

LIBRARY Michigan State University

This is to certify that the thesis entitled

CONTROL OF THE MAIN BEAM OF A HALF-WIDTH MICROSTRIP LEAKY-WAVE ANTENNA BY EDGE LOADING USING THE TRANSVERSE RESONANCE METHOD

presented by

MICHAEL LANRE ARCHBOLD

has been accepted towards fulfillment of the requirements for the

M.S. degree in ELECTRICAL ENGINEERING

Major Professor's Signature

2 November 2008

Date

MSU is an Affirmative Action/Equal Opportunity Employer

PLACE IN RETURN BOX to remove this checkout from your record. **TO AVOID FINES** return on or before date due. **MAY BE RECALLED** with earlier due date if requested.

DATE DUE	DATE DUE	DATE DUE

5/08 K./Proj/Acc&Pres/CIRC/DateDue indd

CONTROL OF THE MAIN BEAM OF A HALF-WIDTH MICROSTRIP LEAKY-WAVE ANTENNA BY EDGE LOADING USING THE TRANSVERSE RESONANCE METHOD

By

Michael Lanré Archbold

A THESIS

Submitted to
Michigan State University
in partial fulfillment of the requirements
for the degree of

MASTER OF SCIENCE

Electrical Engineering

2008

Copyright by Michael Lanré Archbold 2008

ABSTRACT

CONTROL OF THE MAIN BEAM OF A HALF-WIDTH MICROSTRIP LEAKY-WAVE ANTENNA BY EDGE LOADING USING THE TRANSVERSE RESONANCE METHOD

By

Michael Lanré Archbold

As the need to conserve fuel is ever increasing, developing low-profile, lightweight, broadband antennas is undoubtedly important to the success of the United States Air Force. The Half-Width Microstrip Leaky-Wave Antenna (HMLWA) addresses these important issues along with other beneficial characteristics such as being inexpensive and conformable (say to the fuselage of an aircraft) all while being half the width of its full-width counterpart, the Full-Width Microstrip Leaky-Wave Antenna (FMLWA).

It is well known that the main beam angle of a leaky-wave antenna scans with frequency [1] and that the angle can be controlled by reactively loading the radiating edge [2]-[7]. This work will optimize the reactive loading (lumped capacitors) of a current HMLWA antenna design allowing for fixed-frequency beam steering over the operational frequency range. The Transverse Resonance Method (TRM) is used to analyze the HMLWA antenna for various edge loading configurations. Full-width and half-width antennas are simulated on both finite and infinite ground planes in an attempt to verify the claim that the HMLWA antenna reasonably approximates its full-width counterpart. Furthermore, the radiation pattern of the HMLWA antenna is determined analytically using the Radiating Aperture Method (RAM) and compared to the patterns of simulated antennas. Finally, the proposed antenna is fabricated and measured, and the results are presented.

For Luis and Leslie

ACKNOWLEDGMENTS

First and foremost, I would like to thank God. This work would not have been possible without His grace and mercy.

To my parents, Luis and Leslie Archbold, whom have always placed the highest value on education. Their relentless motivation fueled my desire to continue learning, for that I can never repay them. To my loving fiancé Devin Williams, for her patience throughout this exhausting process. To my sisters, Rose and Josette, you all have set an impeccable example, one that I could only hope to ever achieve.

Sincere gratitude for Drs. Percy Pierre and Barbara O'Kelly. Thank you for providing me with the opportunity to attend graduate school. To my advisor, Dr. Ed Rothwell, thank you for teaching me how to fish, providing infinite meals, rather than giving me a single meal. To my surrogate advisor, Dr. Leo Kempel thank you for providing a priceless opportunity.

To Ms. Jackie Toussaint-Barker of AFRL, thank you for investing in my future. Being an MLP scholar has opened many doors. To my extended AFRL family: Ms. Nivia Colon-Diaz, Dr. Stephen Schneider, Mr. John McCann, Mr. Kyle Zeller, Dr. Dan Janning, and Mr. Matt Longbrake, thank you for welcoming me with open arms and for your assistance. A very special thanks to Dr. Brad Kramer. I appreciate you taking the time to answer my many questions and for providing guidance when I was "spinning my wheels". And last but not least, I would like to thank Mr. Thomas Goodwin for his exceptional editorial skills that were pushed to the limit when revising this work. With you all I feel that I have made life-long friends.

TABLE OF CONTENTS

LIST C	F TABLES	vii
LIST C	OF FIGURES	ix
KEY T	O SYMBOLS AND ABBREVIATIONS	xvi
CHAPT		
	action	1
1.1	Background	2
1.2	Research Overview	4
CHAPT Leaky-V	ΓER 2 Wave Antennas	ϵ
2.1	Dispersion Characteristics of the Hybrid Leaky-Wave EH ₁ Mode	8
2.2		
2.2	Half-Width Approximation of a Full-Width Microstrip Leaky-Wave Antenna	10
	2.2.1 Half-Width Approximation of a Full-Width Microstrip Leaky-	
	Wave Antenna on an Infinite Substrate-Ground Plane	11
	2.2.2 Half-Width Approximation of a Full-Width Microstrip Leaky- Wave Antenna on a Finite Substrate-Ground Plane	12
CHAPT	ΓER 3	
Transve	erse Resonance Method	14
3.1	Transmission-line Theory	14
3.2	Terminated Lossless Transmission Line	20 23
3.3	Transverse Resonance Relation	2 4
3.4	TRM method applied to an unloaded HMLWA antenna	28
3.5	Free-edge Admittance	3 4
3.6	TRM method applied to a reactively loaded HMLWA antenna	38
3.7	TRM method Implementation	46
3.8	Fixed Frequency Beam Steering	48
CHAPT	ΓER. 4	
	cal Solution	53
4.1	Cavity Model of HMLWA antenna	53
4.2	The Radiating Aperture Model	55

63
65 65 67 71
73 77
7 9
80
82
93
93
93
103
109
116
196

LIST OF TABLES

Table 2.1	Radiation Pattern Gain Difference of HMLWA vs. FMLWA Antennas on an Infinite Substrate-Ground Plane Layer	12
Table 2.2	Radiation Pattern Gain Difference of HMLWA vs. FMLWA Antennas on a Finite Substrate-Ground Plane Layer	13
Table 3.1	Lower cutoff frequency, upper cutoff frequency, and bandwidth of various capacitive loads	46
Table 3.2	Capacitive limits used to compute fixed main beam vs. frequency tabulated values	48
Table 3.3	Capacitive Load required to fix Main Beam at 10° over C-band .	49
Table 3.4	Capacitive Load required to fix Main Beam at 20° over C-band .	49
Table 3.5	Capacitive Load required to fix Main Beam at 30° over C-band .	50
Table 3.6	Capacitive Load required to fix Main Beam at 40° over C-band .	50
Table 3.7	Capacitive Load required to fix Main Beam at 50° over C-band .	50
Table 3.8	Capacitive Load required to fix Main Beam at 60° over C-band .	51
Table 3.9	Capacitive Load required to fix Main Beam at 70° over C-band .	51
Table 3.10	Capacitive Load required to fix Main Beam at 80° over C-band .	51
Table 4.1	Main beam direction of unloaded HMLWA antenna determined analytically using RAM method	62
Table 4.2	Main beam direction of 0.10 pF edge-loaded HMLWA antenna determined analytically using RAM method	62

LIST OF FIGURES

Figure 1.1	Electric field lines on an open microstrip line operated in the dominant (a) and first higher-order (b) modes. (After [13])	3
Figure 2.1	Typical dispersion characteristics of the hybrid leaky-wave $\mathrm{EH_{1}}$ mode. Yellow, green, magenta, and cyan correspond to the reactive, leaky, surface, and bound regimes, respectively (After [15]).	8
Figure 2.2	Radiation Patterns of HMLWA antenna vs. FMLWA antenna at 7 GHz mounted atop an infinite substrate-ground plane layer. (10 dB radial spacing)	11
Figure 2.3	Radiation Patterns of HMLWA antenna vs. FMLWA antenna at 7 GHz mounted atop a finite substrate-ground plane layer. (10 dB radial spacing)	13
Figure 3.1	General transmission line shown in (a). Transmission line decomposed into differential sections Δx depicted in (b). And equivalent circuit of each differential section (c) (After [23])	16
Figure 3.2	Transmission Line terminated in an arbitrary load impedance \mathbf{Z}_L .	21
Figure 3.3	Short-circuited transmission line	23
Figure 3.4	TRM method applied to an unloaded HMLWA antenna	28
Figure 3.5	Dispersion curves of the hybrid leaky-wave EH_1 mode. Operational region: 5.889-8.115 GHz. $BW=31.80\%$	34
Figure 3.6	Convergence of $Q(-\delta_{\epsilon})$ vs. m for ϵ_r =2.33	37
Figure 3.7	TRM method applied to an edge-loaded HMLWA antenna	39
Figure 3.8	Dispersion curves of the hybrid leaky-wave EH ₁ mode of a 0.10 pF loaded HMLWA antenna. Operational region: $3.928-4.869$ GHz. $BW=21.39\%$	44
Figure 3.9	Phase coefficients for various capacitive loads ranging from 0.02 to 0.10 pF	45

Figure 3.10	Leakage coefficients for various capacitive loads ranging from 0.02 to 0.10 pF	45
Figure 3.11	340 mm edge-loaded HMLWA antennas. Loads spaced every 1.5 mm. Depicts how large capacitance value shorts the radiating edge.	47
Figure 3.12	Main beam direction vs. Capacitance for various Frequencies	52
Figure 4.1	Cavity Model of a Microstrip Antenna	54
Figure 4.2	Magnitude of the Electric field within the aperture of the HMLWA antenna	56
Figure 4.3	HMLWA antenna geometry with radiating aperture	57
Figure 4.4	Analytical solution to far fields maintained by equivalent magnetic current on the surface of the radiating aperture of the unloaded HMLWA antenna.	61
Figure 4.5	Analytical solution to far fields maintained by equivalent magnetic current on the surface of the radiating aperture with 0.10 pF edge loading configuration.	61
Figure 5.1	Unloaded 340 mm HMLWA antenna with through-substrate feed	64
Figure 5.2	Loaded 340 mm HMLWA antenna with edge-launch feed $ \ldots \ldots $	64
Figure 5.3	Exploded view of loaded HMLWA antenna showing 0.10 pF 0603 multilayer capacitors	65
Figure 5.4	Return loss of an unloaded terminated HMLWA antenna	66
Figure 5.5	Return loss of terminated and non-terminated unloaded HMLWA antennas	68
Figure 5.6	(a) PHASEFLEX test assembly. (b) Pasternack 50 Ω termination	68
Figure 5.7	VSWR of terminated and non-terminated unloaded HMLWA antennas	69

Figure 5.8	Simulated vs. Measured $ S_{11} $ Return Loss of Reactively Loaded HMLWA Antenna	70
Figure 5.9	Simulated vs. Measured $ S_{22} $ Return Loss of Reactively Loaded HMLWA Antenna	71
Figure 5.10	(a) NSI-2000 workstation (b) Agilent E8362B PNA	72
Figure 5.11	Reactively loaded HMLWA antenna in Near Field Anechoic Chamber	73
Figure 5.12	(a) 3-dimensional Spherical Pattern and (b) 2-dimensional Contour Plot at 7.00 GHz	75
Figure 5.13	Simulated vs Measured HMLWA Gain at 7.00 GHz	76
Figure 5.14	Unloaded, Simulated Reactively Loaded, and Measured Reactively Loaded HMLWA Antenna Main Beam Direction Comparison	77
Figure 5.15	Simulated vs Measured Radiation Efficiency	78
Figure B.1	Radiation Patterns of HMLWA antenna vs. FMLWA antenna at $6GHz$ mounted atop an infinite substrate-ground plane layer	93
Figure B.2	Radiation Patterns of HMLWA antenna vs. FMLWA antenna at $6.25GHz$ mounted atop an infinite substrate-ground plane layer	94
Figure B.3	Radiation Patterns of HMLWA antenna vs. FMLWA antenna at $6.5GHz$ mounted atop an infinite substrate-ground plane layer	94
Figure B.4	Radiation Patterns of HMLWA antenna vs. FMLWA antenna at $6.75GHz$ mounted atop an infinite substrate-ground plane layer	95
Figure B.5	Radiation Patterns of HMLWA antenna vs. FMLWA antenna at 7 GHz mounted atop an infinite substrate-ground plane layer	95
Figure B.6	Radiation Patterns of HMLWA antenna vs. FMLWA antenna at $7.25GHz$ mounted atop an infinite substrate-ground plane layer	96
Figure B.7	Radiation Patterns of HMLWA antenna vs. FMLWA antenna at $7.5GHz$ mounted atop an infinite substrate-ground plane layer.	96

Figure B.8	Radiation Patterns of HMLWA antenna vs. FMLWA antenna at $7.75GHz$ mounted atop an infinite substrate-ground plane layer.	97
Figure B.9	Radiation Patterns of HMLWA antenna vs. FMLWA antenna at $8GHz$ mounted atop an infinite substrate-ground plane layer	97
Figure B.10	Radiation Patterns of HMLWA antenna vs. FMLWA antenna at $6GHz$ mounted atop a finite substrate-ground plane layer	98
Figure B.11	Radiation Patterns of HMLWA antenna vs. FMLWA antenna at $6.25GHz$ mounted atop a finite substrate-ground plane layer	98
Figure B.12	Radiation Patterns of HMLWA antenna vs. FMLWA antenna at $6.5GHz$ mounted atop a finite substrate-ground plane layer	99
Figure B.13	Radiation Patterns of HMLWA antenna vs. FMLWA antenna at $6.75GHz$ mounted atop a finite substrate-ground plane layer	99
Figure B.14	Radiation Patterns of HMLWA antenna vs. FMLWA antenna at $7GHz$ mounted atop a finite substrate-ground plane layer	100
Figure B.15	Radiation Patterns of HMLWA antenna vs. FMLWA antenna at $7.25GHz$ mounted atop a finite substrate-ground plane layer	100
Figure B.16	Radiation Patterns of HMLWA antenna vs. FMLWA antenna at $7.5GHz$ mounted atop a finite substrate-ground plane layer	101
Figure B.17	Radiation Patterns of HMLWA antenna vs. FMLWA antenna at $7.75GHz$ mounted atop a finite substrate-ground plane layer	101
Figure B.18	Radiation Patterns of HMLWA antenna vs. FMLWA antenna at $8GHz$ mounted atop a finite substrate-ground plane layer	102
Figure C.1	Free-edge resistance of the unloaded HMLWA antenna	103
Figure C.2	Free-edge reactance of the unloaded HMLWA antenna	104
Figure C.3	$Re(\chi)$ of the unloaded HMLWA antenna	105
Figure C.4	$Im(\chi)$ of the unloaded HMLWA antenna	105

Figure	C.5	$ \chi $ of the unloaded HMLWA antenna	106
Figure	C.6	$Ang(\chi)$ of the unloaded HMLWA antenna	106
Figure	C.7	$Re(k_T)$ of the unloaded HMLWA antenna	107
Figure	C.8	$Im(k_T)$ of the unloaded HMLWA antenna	107
Figure	C.9	$Re(k_z)$ of the unloaded HMLWA antenna	108
Figure	C.10	$Im(k_z)$ of the unloaded HMLWA antenna	108
Figure	D.1	Free-edge resistance of the 0.10 pF loaded HMLWA antenna	110
Figure	D.2	Free-edge reactance of the 0.10 pF loaded HMLWA antenna	110
Figure	D.3	Radiating-edge resistance of the 0.10 pF loaded HMLWA antenna.	111
Figure	D.4	Radiating-edge reactance of the 0.10 pF loaded HMLWA antenna.	111
Figure	D.5	$Re(\chi)$ of the 0.10 pF loaded HMLWA antenna	112
Figure	D.6	$Im(\chi)$ of the 0.10pF loaded HMLWA antenna	112
Figure	D.7	$ \chi $ of the 0.10 pF loaded HMLWA antenna	113
Figure	D.8	$Ang(\chi)$ of the 0.10 pF loaded HMLWA antenna	113
Figure	D.9	$Re(k_T)$ of the 0.10 pF loaded HMLWA antenna	114
Figure	D.10	$Im(k_T)$ of the 0.10 pF loaded HMLWA antenna	114
Figure	D.11	$Re(k_z)$ of the 0.10 pF loaded HMLWA antenna	115
Figure	D.12	$Im(k_z)$ of the 0.10 pF loaded HMLWA antenna	115
Figure	E.1	Measured Radiation Pattern of HMLWA antenna at $4.00~\mathrm{GHz}$	116
Figure	E.2	Measured Radiation Pattern of HMLWA antenna at 4.25 GHz	117

Figure	E.3	Measured	Radiation	Pattern	of HMLWA	antenna a	t 4.50	GHz	 117
Figure	E.4	Measured	Radiation	Pattern	of HMLWA	antenna a	t 4.75	GHz	 118
Figure	E.5	Measured	Radiation	Pattern	of HMLWA	antenna a	t 5.00	GHz	 118
Figure	E.6	Measured	Radiation	Pattern	of HMLWA	antenna a	t 5.25	GHz	 119
Figure	E.7	Measured	Radiation	Pattern	of HMLWA	antenna a	t 5.50	GHz	 119
Figure	E.8	Measured	Radiation	Pattern	of HMLWA	antenna a	t 5.75	GHz	 120
Figure	E.9	Measured	Radiation	Pattern	of HMLWA	antenna a	t 6.00	GHz	 120
Figure	E.10	Measured	Radiation	Pattern	of HMLWA	antenna a	t 6.25	GHz	 121
Figure	E.11	Measured	Radiation	Pattern	of HMLWA	antenna a	t 6.50	GHz	 121
Figure	E.12	Measured	Radiation	Pattern	of HMLWA	antenna a	t 6.75	GHz	 122
Figure	E.13	Measured	Radiation	Pattern	of HMLWA	antenna a	t 7.00	GHz	 122
Figure	E.14	Measured	Radiation	Pattern	of HMLWA	antenna a	t 7 .25	GHz	 123
Figure	E.15	Measured	Radiation	Pattern	of HMLWA	antenna a	t 7.50	GHz	 123
Figure	E.16	Measured	Radiation	Pattern	of HMLWA	antenna a	t 7 .75	GHz	 124
Figure	E.17	Measured	Radiation	Pattern	of HMLWA	antenna a	t 8.00	GHz	 124

Images in this thesis are presented in color.

KEY TO SYMBOLS AND ABBREVIATIONS

AFRL: Air Force Research Laboratory

AUT: Antenna Under Test

EIA: Electronic Industries Alliance

EM: Electromagnetic

FBR: Front-to-Back Ratio

FMLWA: Full-Width Microstrip Leaky-Wave Antenna

HMLWA: Half-Width Microstrip Leaky-Wave Antenna

KCL: Kirchoff's Current Law

KVL: Kirchoff's Voltage Law

MLWA: Microstrip Leaky-Wave Antenna

NSI: Nearfield Systems Incorporated

OEWG: Open-ended Waveguide

PEC: Perfect Electric Conductor

PMC: Perfect Magnetic Conductor

PUL: Per Unit Length

RAM: Radiating Aperture Method

RASCAL: Radiation and Scattering Compact Antenna Laboratory

ROI: Region of Interest

RY: Sensors Directorate

SGH: Standard Gain Horn

SMA: SubMiniature Version A

TEM: Transverse Electromagnetic

TE: Transverse Electric

TM: Transverse Magnetic

TRM: Transverse Resonance Method

TWA: Traveling Wave Antenna

VNA: Vector Network Analyzer

VSWR: Voltage Standing Wave Ratio

WRT: With Respect To

CHAPTER 1

INTRODUCTION

Microstrip Leaky-Wave Antennas (MLWA) are traveling-wave printed antennas wherein the microstrip is responsible for radiation. Due to their inherently small size, low-profile, and conformability, they are well suited for aerospace applications where all of the abovementioned constraints are addressed. As the name suggests, a Half-Width Microstrip Leaky-Wave Antenna (HMLWA) is one half the width of a full-width antenna whereby a perfect electric conducting (PEC) septum connects the microstrip to the ground plane, ridding the need of half of the antenna.

As one side of the HMLWA antenna is open to free space, it is well known that the edge reflection coefficient affects the propagation characteristics of the antenna. With knowledge of the admittance looking into the free edge available in the literature [8], modifying this edge reflection coefficient by reactively loading the free edge alters the propagation characteristics of the antenna. In this thesis, the main beam direction of a HMLWA antenna is steered at fixed frequencies by placing lumped multilayer capacitors (MLC) in shunt with the free edge of the microstrip and the ground plane.

As waves of the hybrid leaky-wave EH₁ mode propagate along the conducting strip, radiation occurs because the hybrid leaky-wave mode is loosely bound to the microstrip. In order to control the direction of the energy one must study the relationship between the guided wave phase coefficient, β , and frequency, ω . (Note that the term "coefficient" is used rather than the more frequently encountered term "constant" to emphasize the frequency dependence of the phase.) The guided wave phase coefficient is dependent on the reactive loading at the free edge (see Figure 3.9); and since the main beam direction depends on the phase coefficient, it follows that the main beam direction can be controlled at fixed frequencies.

The Transverse Resonance Method (TRM) is used to determine the complex propagation coefficient of the wave. It simplifies the analysis by employing transmission line theory rather than complex field theory. Since the TRM method is an approximation, a full-wave solution using commercially available software (CST MICROWAVE STUDIO® and FEKO Suite 5.3) is determined prior to antenna fabrication.

1.1 Background

In 1976, Helmut Ermert presented a paper on the dominant and higher-order modes on microstrip lines in which he investigated mode propagation on covered microstrip lines [9]. In a subsequent publication, [10] Ermert investigated the dominant and the first two higher-order modes on both covered and open microstrip lines. He concluded that radiation was not feasible because in the "radiation region" the wave number was purely real, resulting in only a phase coefficient, and no leakage coefficient.

A few years later in 1979, Wolfgang Menzel, a German scientist, presented a traveling-wave microstrip antenna that took advantage of the first higher-order EH₁ mode [11]. Menzel's antenna was a full-width microstrip antenna that consisted of several transverse slots (with respect to the longitudinal guiding axis) nearest to the feed. The transverse slots served the purpose of suppressing the non-radiating, dominant EH₀ microstrip mode. Although Menzel's transverse slot technique was inefficient at suppressing all of the dominant-mode radiation, hence mode purity was not entirely assured, his antenna was indeed successful, and 65% of the power leaked away in the form of space waves [12].

More than two decades later, engineers at the Air Force Research Laboratory (AFRL) developed a more efficient way to suppress the non-radiating EH₀ mode while simultaneously exciting the radiating first higher-order EH₁ mode. When a microstrip is operated in the first higher-order mode, a phase-reversal appears along the centerline of the structure resulting in a null in the Electric field. Figure 1.1

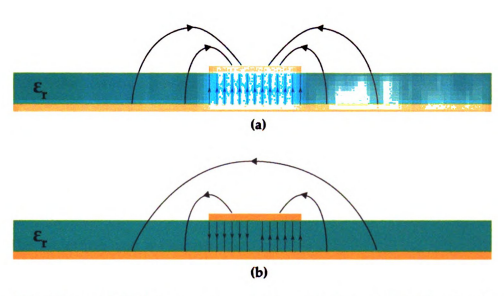


Figure 1.1. Electric field lines on an open microstrip line operated in the dominant (a) and first higher-order (b) modes. (After [13]).

shows the cross section of a Full-Width Microstrip Leaky-Wave Antenna (FMLWA) depicting the Electric field lines of the dominant (EH $_0$) and first higher-order (EH $_1$) modes. The voltage is equal to the product of the Electric field and the height of the substrate. Since the height of the substrate is nonzero, the field is identically zero at the origin. AFRL engineers realized that the introduction of a perfectly electric conducting (PEC) septum, or shorting wall, bifurcating the conducting strip does not perturb the fields because it is subject to the boundary condition that tangential electric fields vanish along its surface. Both simulations and measurements support the supposition. Initially, this PEC septum was fabricated using shorting pins, then as a slit covered with copper tape, and finally in its current form, copper plated through holes, or vias. The PEC septum also simplifies the feeding network because it inherently excites the radiating EH $_1$ mode.

AFRL engineers later realized that if the conducting strip is truncated to half its size, resulting in the HMLWA antenna [14], the radiation pattern is nearly the same as that of the full-width version. (See simulated results in Appendix B.) In this thesis, the main beam direction of a HMLWA antenna is steered at fixed frequencies by reactively loading the radiating edge.

Although the literature contains several papers on fixed-frequency beam steering of leaky-wave antennas, this author has not seen this accomplished (or attempted) with a reactively loaded HMLWA antenna. In [2], Noujeim uses the transverse resonance and finite-difference time-domain methods for beam steering of a full-width leaky-wave antenna loaded with a reactive sheet. Here, the conducting strip is bisected about the centerline, and a reactive sheet connects the two halves. Augustin et al. describes a reactively loaded slot line leaky-wave antenna in [3], and in a subsequent publication scans the main beam using varactors [4]. And finally, in [5] a full-width leaky-wave antenna is reactively loaded on both sides of the conducting strip, resulting in a tilt in the main beam direction with respect to the unloaded counterpart. More reactively loaded antenna designs are considered in [6] and [7].

1.2 Research Overview

In order to understand leaky-wave antennas, it is necessary to understand modes, particularly the first higher-order radiating mode, on microstrip lines. Chapter 2 presents typical dispersion curves of the first higher-order hybrid leaky-wave EH₁ mode. This chapter also contains the details explaining how the HMLWA antenna reasonably approximates its full-width counterpart, the FMLWA antenna. In Chapter 3, the TRM method, the mathematical model used in this work, is presented. Here, the TRM is initially applied to an unloaded HMLWA antenna, then to the reactively loaded HMLWA antenna. The transverse resonance relation is derived, and the mathematics of the method is thoroughly explained. Chapter 3 concludes with tabulated values of capacitive loads required to fix the main-beam direction of the HMLWA antenna at various angles over the C-band (4-8 GHz) of the electromagnetic (EM) spectrum. In Chapter 4 the Radiating Aperture Method (RAM) is used to compute the radi-

ation fields of the HMLWA antenna. The HMLWA antenna design and measured data is presented in Chapter 5, along with a detailed description of the apparatus and associated settings during data collection. Finally, Appendices A–E provide the details for construction of solutions from potentials, simulated radiation patterns of HMLWA and FMLWA antennas, characteristics of both unloaded and 0.10 pF loaded HMLWA antennas, and measured data of the 0.10 pF loaded HMLWA antenna over the C-band of the EM spectrum.

CHAPTER 2

LEAKY-WAVE ANTENNAS

According to [1], a leaky-wave antenna is an antenna that leaks power all along its length via some mechanism. A characteristic of this antenna is the frequency dependence of the main beam direction. This frequency dependence results in the main beam direction scanning over the entire operational range (beginning near broadside and terminating near end fire) of the particular leaky-wave antenna. Although this frequency scanning characteristic makes leaky-wave antennas attractive for certain applications, fixing the main beam at particular frequencies would allow more applications for the antenna whereby its other attractive attributes could be exploited (e.g., ease of fabrication, conformability and reasonable cost).

Since the phase coefficient, β , depends on frequency, and the main beam direction depends on β , it follows that the main beam direction is frequency dependent. The problem lies in keeping the main beam direction fixed at a given angle, resulting in a frequency invariant main beam direction over the operational leaky region. The operational leaky-wave region is defined in Section 2.1.

The complex propagation coefficient is defined as

$$k_{\zeta} = \beta_{\zeta} - j\alpha_{\zeta},\tag{2.1}$$

where the real and imaginary parts, β and α , are known as the phase and leakage coefficients, respectively, with $\zeta = x, y, z$. The phase coefficient for a wave propagating through a medium is related to the phase velocity of the wave, ν_p , by the following expression

$$\beta = \frac{\omega}{\nu_p}.\tag{2.2}$$

Further, for a transmission line, which a microstrip is classified as, the phase velocity of the wave is inversely proportional to the per unit length (PUL) capacitance, inductance, conductance, and resistance of the line, dictated by

$$\nu_p = \frac{\omega}{Im(\sqrt{(R'+jwL')(G'+jwC')})}.$$
(2.3)

In the case of a lossless line, equation 2.3 reduces to

$$\nu_p = \frac{1}{\sqrt{L'C'}}.\tag{2.4}$$

The primes on the parameters in equations (2.3) and (2.4) denote the PUL dependence. Substituting either expression ((2.3) or (2.4)) for the phase velocity into (2.2) reveals a directly proportional relationship between the phase coefficient and the PUL transmission line parameters. This relationship describes the premise of this thesis: reactively loading the HMLWA antenna, by placing capacitors along the radiating edge, decreases the phase velocity of the propagating wave, ultimately changing the phase coefficient of the propagating wave.

The dominant microstrip mode is a quasi-transverse electromagnetic (TEM) mode in which both the electric and magnetic fields have a component in the direction of propagation, and is designated EH₀. When the EH₀ mode propagates, the electric field exhibits even symmetry about the center of the structure and the electromagnetic fields are bound to the structure; hence, the dominant mode does not radiate (for electrically thin substrates with $h \ll \lambda$). Since the HMLWA antenna is a microstrip leaky-wave antenna, the first higher-order mode must be excited for EM fields to decouple and radiate away from the structure [15]. The first higher-order mode, the hybrid leaky-wave EH₁ mode, exhibits peculiar phenomena above cutoff. It is the topic of many papers, viz. [16]-[20], and is explained in Section 2.1.

2.1 Dispersion Characteristics of the Hybrid Leaky-Wave EH₁ Mode

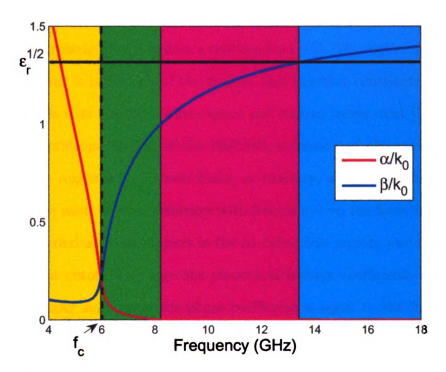


Figure 2.1. Typical dispersion characteristics of the hybrid leaky-wave EH₁ mode. Yellow, green, magenta, and cyan correspond to the reactive, leaky, surface, and bound regimes, respectively (After [15]).

The operational region of the HMLWA antenna considered in this thesis lies in the C-band of the EM spectrum. The operational or leaky region is one of four frequency regions associated with propagation of higher-order modes on microstrip lines [15]. It is preceded by the reactive regime and succeeded by the surface and bound regimes.

Figure 2.1 depicts typical dispersion characteristics of the first higher-order mode, along with the four regions explicitly labeled. The figure depicts the phase and leakage coefficients, both normalized with respect to the free-space wave number, k_0 , in blue and red, respectively. The first of the four regions is the only region below cutoff and is one of the two regions in the so called fast region. The fast region is the region where the wave velocity is faster than the speed of light, i.e. $\nu_p > c$, and the axial phase coefficient, β_y , is less than the free-space wave number, k_0 . Known as the reactive region, the region shaded in yellow is named accordingly because here attenuation is high and the microstrip line resembles a reactive load [15]. The region shaded in green is the leaky region. It is the first of two regions that together constitute the radiation region: the region that identifies where space and surface waves exist [16]. The leaky region is the operational region of the HMLWA antenna and the region of interest because it is the region where power leaks, or radiates, away from the structure at some angle θ (the value of which changes with frequency), in the form of a space wave [16]. It is the second and final region in the so called fast region, and it is bound on the lower side (at cutoff, f_c) where the phase and leakage coefficients are equal and bound on the upper side where the phase coefficient is equal to the free-space wave number. The main beam direction is near broadside at lower frequencies and scans toward near end fire at higher frequencies.

The two regions in the slow region, where $\nu_p < c$, are the surface and bound regions. In the surface region, one of the two transverse leakage coefficients, say α_z , dominates and attenuates the leaky wave. It is the region shown in magenta from $\beta = k_0$ to $\beta = k_s$, where k_s is the wave number of the surface wave and is given by

$$k_s = \sqrt{k_x^2 + k_z^2}. (2.5)$$

Just as in the leaky region, in the surface region power radiates away from the structure at some angle ψ , except here the leakage is in the plane of the structure (the XY plane) rather than in the plane normal to the structure (the YZ plane). Therefore the waves are bound to the structure as opposed to radiating away from it. The surface region is the second region for which radiation can occur. The fourth and final

region is the bound region. It is the region shaded in cyan in Figure 2.1. Here, the remaining transverse leakage coefficient, α_x , dominates and attenuates the surface wave. The bound region begins when $\beta = k_s$, and ends when the next higher-order mode propagates.

2.2 Half-Width Approximation of a Full-Width Microstrip Leaky-Wave Antenna

Although the HMLWA antenna approximates the behavior of the FMLWA antenna, the behavior is not identical. One of its principal advantages, as mentioned in [21], is that the feeding network is simplified. Since the half-width configuration inherently excites the hybrid leaky-wave EH₁ mode with the added benefit of suppressing the dominant EH₀ mode, there is no need for an external 180° Hybrid as required for the FMLWA antenna. Sections 2.2.1 and 2.2.2 present simulated radiation patterns of HMLWA and FMLWA antennas on both infinite and finite ground planes.

For the simulations, the antenna geometries consist of conducting strip widths of 15 and 7.5 mm for the full and half-width antennas, respectively. The length of the conducting strip is 340 mm for both geometries. Optimal feed placement is determined from numerous simulations and is provided by antenna engineers at AFRL to be 4.8025 mm in either direction from the centerline of the full-width antenna (i.e., if the antenna is centered at the origin, to excite the EH₁ mode – requiring a 180° phase shift – feeds are placed at \pm 4.8025 mm from the origin) and 4.8025 mm away from the PEC conducting septum of the half-width antenna. Both the FMLWA and HMLWA antennas are terminated in 50 Ω loads placed at the end of the conducting strip, 340 mm from the feed. The load is placed at the centerline of the FMLWA antenna, and 4.8025 mm away from the PEC conducting septum of the HMLWA antenna. The dielectric substrate is modeled as Rogers RT/duroid 5870, characterized by a relative permittivity of ϵ_r =2.33 and a dissipation factor of

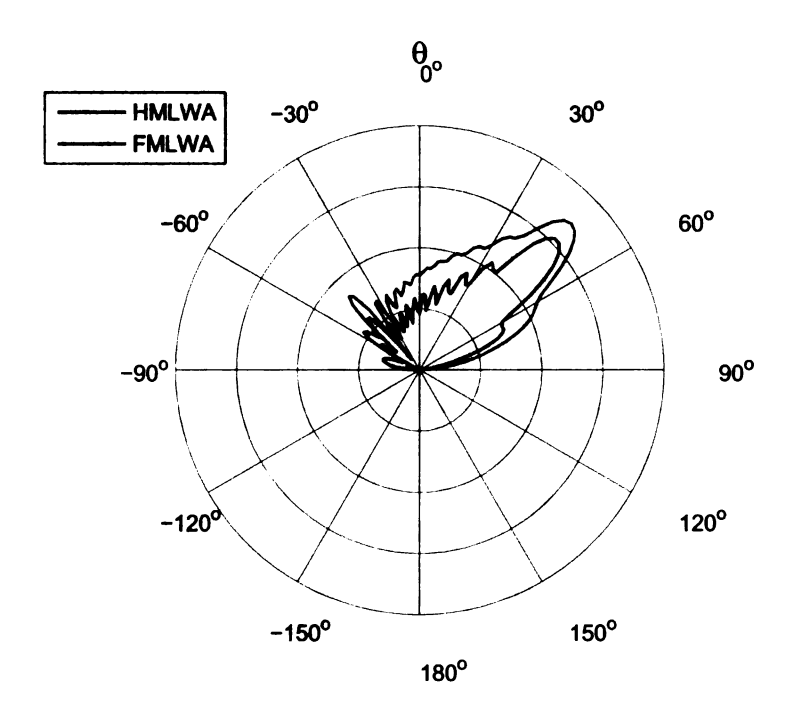


Figure 2.2. Radiation Patterns of HMLWA antenna vs. FMLWA antenna at 7 GHz mounted atop an infinite substrate-ground plane layer. (10 dB radial spacing)

 $\tan \delta = 0.0012$.

2.2.1 Half-Width Approximation of a Full-Width Microstrip Leaky-Wave Antenna on an Infinite Substrate-Ground Plane

The radiation pattern shown in Figure 2.2, was computed using a FEKO Suite 5.3 simulation of the antennas. Radiation patterns covering the operational range of the antennas (6-8 GHz), computed every 250 MHz, are given in Appendix B. In both full-width and half-width geometries, the conducting strip is married to an infinite substrate-ground plane layer via FEKO's multilayer planar Green's function option. The geometries are meshed using triangles with an edge length of $\frac{\lambda_{min}}{15}$, where $\lambda_{min} = \frac{c}{8GHz}$, the smallest wavelength of the C-band.

Figure B.1-Figure B.9 show that when the antennas are mounted atop an infinite

substrate-ground plane layer, the elevation plane (YZ) patterns are quite similar. Although there is noticeable attenuation (in some cases exceeding 4.5 dB, see Table 2.1), in the patterns of the HMLWA antenna over the entire leaky region, the main beam direction does not vary more than 2° from the FMLWA antenna for all frequencies.

Table 2.1. Radiation Pattern Gain Difference of HMLWA vs. FMLWA Antennas on an Infinite Substrate-Ground Plane Layer

	round I faire Day	
F	requency (GHz)	Gain Difference (dB)
	6.00	4.30
	6.25	2.54
	6.50	2.89
	6.75	3.12
	7.00	3.62
	7.25	3.67
	7.50	4.39
	7.75	4.27
	8.00	4.76
1		

2.2.2 Half-Width Approximation of a Full-Width Microstrip Leaky-Wave Antenna on a Finite Substrate-Ground Plane

More accurate results are obtained when the HMLWA antenna approximates the FMLWA antenna on the practical case of a finite substrate-ground plane layer. CST MICROWAVE STUDIO is used to compute the radiation patterns of this case, and the radiation pattern of the antennas at 7.00 GHz is shown in Figure 2.3. Here, as opposed to Figure 2.2, the HMLWA antenna pattern more reasonably approximates the FMLWA antenna pattern with less than a 0.8 dB difference (see Table 2.2) in the gain and a 2° angular variation in the main beam direction. Appendix B gives the radiation patters over the operational range of the antennas (6-8 GHz) at every 250 MHz.

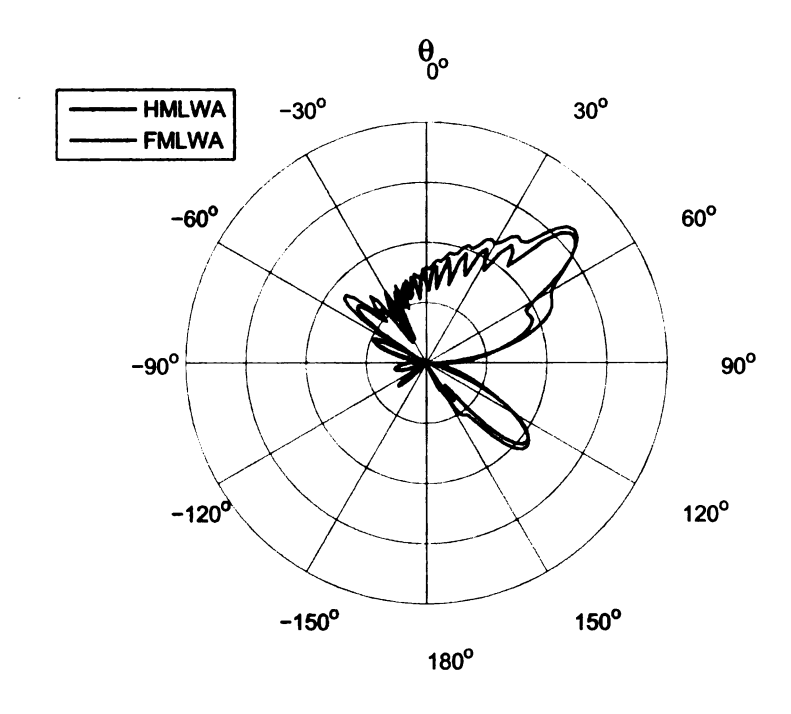


Figure 2.3. Radiation Patterns of HMLWA antenna vs. FMLWA antenna at 7 GHz mounted atop a finite substrate-ground plane layer. (10 dB radial spacing)

Table 2.2. Radiation Pattern Gain Difference of HMLWA vs. FMLWA Antennas on a Finite Substrate-Ground Plane Layer

Frequency (GHz)	Gain Difference (dB)
6.00	1.24
6.25	0.96
6.50	1.07
6.75	0.96
7.00	0.78
7.25	0.73
7.50	1.00
7.75	0.26
8.00	0.70

CHAPTER 3

TRANSVERSE RESONANCE METHOD

The transverse resonance method is a technique used to determine the complex propagation coefficient of many practical composite waveguide structures as well as traveling-wave antenna systems [22]. The method uses the behavior of the wave transverse to the guiding direction to determine the characteristics of the wave along the guiding axis. With the TRM method, the cross section of the structure is represented as a transmission line operating at resonance. The resonances of the transverse transmission line model provide a transcendental equation that, when coupled with the constraint equation, yields the propagation coefficient γ . The method is accurate provided that the transverse resonance relation, a result of the continuity of tangential fields, is maintained (see Section 3.3).

It is important to note that the TRM method is an approximation and only provides the complex propagation coefficient of the structure to which it is applied. More exhaustive techniques, which invoke a full-wave solution, are required to determine other design parameters including field distributions and wave impedances. However, a reasonable approximation of the radiation fields are determined using the radiating aperture method (see Section 4.2) based on the propagation coefficient found using the TRM method. Before considering the details of the TRM method, a brief review of relevant transmission-line theory will be explained.

3.1 Transmission-line Theory

The analysis in this section is restricted to the distributed parameter approach, foregoing the usual circuit theory (lumped-element) technique, because the physical dimensions of the HMLWA antenna are not small when compared to a wavelength. This criterion is based on the rule of thumb that transmission-line effects, such as the phase shift associated with time delay and the reflection due to load mismatch, must be considered when the broadest dimension of the structure, l, is, at least approximately, one one-hundredth of a wavelength, represented mathematically as [23]

$$l \gtrsim \frac{\lambda}{100}.\tag{3.1}$$

To facilitate the understanding of the distributed parameter model, the concepts used in its derivation will be reviewed. Composed of per unit length inductance, resistance, conductance, and capacitance, the model represents the physics of the transmission line using distributed electrical components. To account for the combined resistance, inductance, and capacitance of the conductors, the model includes PUL parameters R' (Ω/m), L' (H/m), and C' (F/m), respectively. If the medium separating the conductors is not free space, its effects must be accounted for with the inclusion of an additional parameter, conductance. Denoted by G' (S/m), the PUL conductance describes the resistance of the dielectric medium separating the two conductors. The parameters are denoted with primes to show the explicit PUL dependence. If the length of the transmission line is l, then the net resistance of the line is R'l (Ω). Total inductance, capacitance, and conductance are determined in the same fashion.

A transmission line can be decomposed into several cascaded differential sections, each of width Δx , provided that each section is electrically small. Each section is modeled by an equivalent circuit using the PUL parameters previously addressed. An arbitrary length of transmission line and its equivalent circuit are shown in Figure 3.1.

Propagating waves on a transmission line obey the wave equation. The wave equation is derived by applying Kirchoff's voltage and current laws to the electrically small section of the transmission line depicted in Figure 3.1. Kirchoff's voltage law

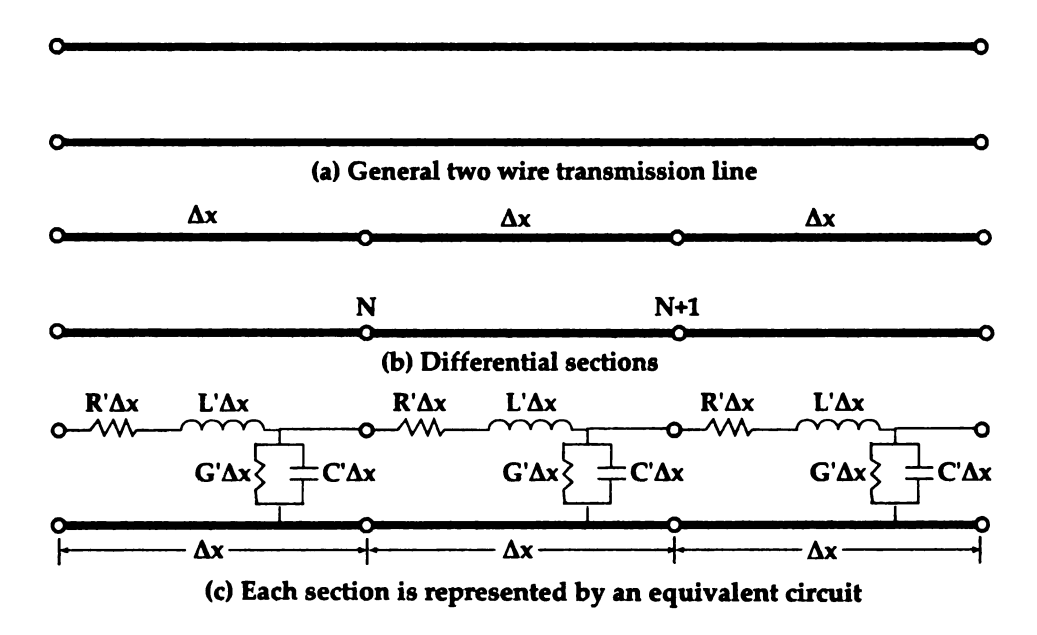


Figure 3.1. General transmission line shown in (a). Transmission line decomposed into differential sections Δx depicted in (b). And equivalent circuit of each differential section (c) (After [23]).

(KVL) states that the sum of the voltages in any loop must vanish. Kirchoff's current law (KCL) states that the sum of current into any node must vanish. Application of KVL to the outer loop in Figure 3.1 yields

$$-v(x,t) + R'\Delta x i(x,t) + L'\Delta x \frac{\partial i(x,t)}{\partial t} + v(x+\Delta x,t) = 0.$$
 (3.2)

Rearranging terms leads to

$$v(x + \Delta x, t) - v(x, t) = -R' \Delta x i(x, t) - L' \Delta x \frac{\partial i(x, t)}{\partial t}.$$
 (3.3)

Dividing equation (3.3) by Δx yields

$$\frac{v(x + \Delta x, t) - v(x, t)}{\Delta x} = \frac{-R' \Delta x i(x, t)}{\Delta x} - \frac{L' \Delta x}{\Delta x} \frac{\partial i(x, t)}{\partial t}$$

$$= -R' i(x, t) - L' \frac{\partial i(x, t)}{\partial t}, \qquad (3.4)$$

and in the limit as $\Delta x \rightarrow 0$ equation (3.4) becomes

$$\frac{\partial v(x,t)}{\partial x} = -R'i(x,t) - L'\frac{\partial i(x,t)}{\partial t}.$$
 (3.5)

Equation (3.5) is a first-order partial differential equation relating the voltage and current. It is one of two time-domain transmission-line, or telegrapher, equations. The second equation is derived by applying KCL to node N+1 in Figure 3.1 and following the steps used to derive equations (3.3) through (3.5) above. The second telegrapher's equation is given as

$$\frac{\partial i(x,t)}{\partial x} = -G'v(x,t) - C'\frac{\partial v(x,t)}{\partial t}.$$
 (3.6)

To simplify the analysis and remain consistent with the notation expressed in this thesis, the telegrapher's equations will be analyzed in the frequency domain using phasor notation. The phasors are defined with a cosine reference, and conversion from a quantity in phasor form to its time-varying counterpart is accomplished by

$$\mathcal{A}(x, y, z, t) = Re\{A(x, y, z)e^{j\omega t}\},\tag{3.7}$$

where A(x, y, z, t) represents a time-varying quantity, and A(x, y, z) represents the phasor. Equations (3.5) and (3.6) can now be recast in their equivalent steady-state

phasor form as

$$\frac{dV(x)}{dx} = -R'I(x) - j\omega L'I(x)$$

$$= -(R' + j\omega L')I(x),$$
(3.8)

and

$$\frac{dI(x)}{dx} = -G'V(x) - j\omega C'V(x)$$

$$= -(G' + j\omega C')V(x), \qquad (3.9)$$

respectively.

Equations (3.8) and (3.9) are coupled first-order ordinary differential equations. It is necessary to decouple these equations in order to solve for the voltage and current along the transmission line. Differentiating equation (3.8) with respect to x leads to

$$\frac{d^2V(x)}{dx^2} = -(R' + j\omega L')\frac{dI(x)}{dx},$$
(3.10)

and substituting equation (3.9) yields

$$\frac{d^2V(x)}{dx^2} = -(R' + j\omega L')\frac{dI(x)}{dx}$$

$$= (R' + j\omega L')(G' + j\omega C')V(x)$$

$$= \gamma^2(\omega)V(x), \tag{3.11}$$

where $\gamma(\omega)$, the complex propagation coefficient, is defined as

$$\gamma(\omega) \equiv \sqrt{(R' + j\omega L')(G' + j\omega C')}.$$
 (3.12)

The real part of the complex propagation coefficient, the leakage or attenuation coef-

ficient, is denoted by α , and the imaginary part, the phase coefficient, is denoted by β .

The current wave equation is derived by differentiating equation (3.9) and substituting equation (3.8) into that result giving

$$\frac{d^2I(x)}{dx^2} = \gamma^2(\omega)I(x). \tag{3.13}$$

Equations (3.11) and (3.13), are linear, second-order, homogeneous, ordinary differential equations. Candidate solutions include exponentials, sines, cosines, or a linear combination of them. The solutions chosen should complement the physics of the problem. It is for this reason that exponentials are chosen as the solution of the wave equations, for they represent traveling waves, while sines and cosines represent standing waves. The traveling-wave voltage and current solutions of the wave equations are

$$V(x) = V_o^+ e^{-\gamma x} + V_o^- e^{\gamma x}$$
 (3.14)

and

$$I(x) = I_o^+ e^{-\gamma x} + I_o^- e^{\gamma x}$$
 (3.15)

respectively. The characteristic impedance of the line can be determined by differentiating equation (3.14)

$$\frac{dV(x)}{dx} = \frac{dV_o^+ e^{-\gamma x}}{dx} + \frac{dV_o^- e^{\gamma x}}{dx}
= -\gamma V_o^+ e^{-\gamma x} + \gamma V_o^- e^{\gamma x}
= -\gamma (V_o^+ e^{-\gamma x} - V_o^- e^{\gamma x}),$$
(3.16)

and upon substitution into equation (3.8) leads to

$$-\gamma (V_o^+ e^{-\gamma x} - V_o^- e^{\gamma x}) = -(R' + j\omega L')I(x)$$

$$(V_o^+ e^{-\gamma x} - V_o^- e^{\gamma x}) = \frac{(R' + j\omega L')}{\gamma}I(x),$$
(3.17)

where the quantity $\frac{(R'+j\omega L')}{\gamma}$ is known as the characteristic impedance, denoted by Z_0 . The characteristic impedance may also be derived by differentiating equation (3.15), and substituting the result into equation (3.9) leading to $\frac{\gamma}{(G'+j\omega C')}$. Hence the characteristic impedance is defined as:

$$Z_{o} \equiv \frac{(R' + j\omega L')}{\gamma}$$

$$Z_{o} \equiv \frac{\gamma}{(G' + j\omega C')}.$$
(3.18)

The complex propagation coefficient and characteristic impedance, defined in (3.12) and (3.18), respectively, fully characterize any transmission line. Using Equation (3.17) the current on the line can be recast in terms of characteristic impedance as

$$I(x) = \frac{\gamma}{(R' + j\omega L')} (V_o^+ e^{-\gamma x} - V_o^- e^{\gamma x})$$

$$= \frac{1}{Z_o} (V_o^+ e^{-\gamma x} - V_o^- e^{\gamma x})$$

$$= \frac{V_o^+}{Z_o} e^{-\gamma x} - \frac{V_o^-}{Z_o} e^{\gamma x}.$$
(3.19)

3.2 Terminated Lossless Transmission Line

The voltage and current traveling-wave solutions given in (3.14) and (3.19) contain two unknowns, the amplitudes of the incident and reflected waves, V_o^+ and V_o^- , respectively. These unknowns are determined by exciting the transmission line with a source or generator located at x=-1 and terminating the line in an arbitrary load

characterized by impedance Z_L located at x=0. A transmission line terminated in an arbitrary load impedance is shown in Figure 3.2. The load impedance can be

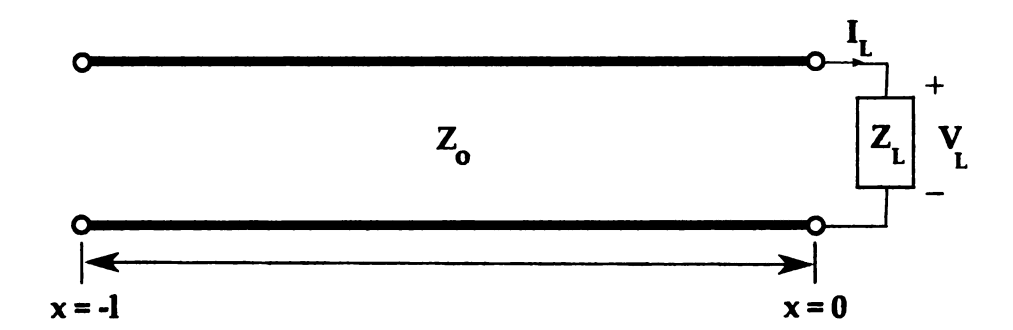


Figure 3.2. Transmission Line terminated in an arbitrary load impedance \mathbf{Z}_L .

described using Ohm's law, V=IZ, as

$$Z_{L} = \frac{V(x=0)}{I(x=0)} = \frac{V_{L}}{I_{L}}$$

$$= \frac{V_{o}^{+}e^{-\gamma 0} + V_{o}^{-}e^{\gamma 0}}{\frac{1}{Z_{o}}(V_{o}^{+}e^{-\gamma 0} - V_{o}^{-}e^{\gamma 0})}$$

$$= \frac{V_{o}^{+} + V_{o}^{-}}{\frac{1}{Z_{o}}(V_{o}^{+} - V_{o}^{-})}$$

$$= Z_{o}\frac{V_{o}^{+} + V_{o}^{-}}{V_{o}^{+} - V_{o}^{-}}.$$
(3.20)

Solving Equation (3.20) for V_o^- gives

$$V_o^- = V_o^+ \frac{Z_L - Z_o}{Z_L + Z_o} \tag{3.21}$$

and so

$$\frac{V_o^-}{V_o^+} = \frac{Z_L - Z_o}{Z_L + Z_o} = \Gamma_L. \tag{3.22}$$

The ratio of the reflected to incident voltage amplitudes, Γ_L , is known as the voltage reflection coefficient. The voltage and current traveling-wave solutions given in (3.14) and (3.19) can now be expressed in terms of the voltage reflection coefficient and are given by:

$$V(x) = V_o^+(e^{-\gamma x} + \Gamma_L e^{\gamma x}) \tag{3.23a}$$

$$I(x) = \frac{V_o^+}{Z_o} (e^{-\gamma x} - \Gamma_L e^{\gamma x}). \tag{3.23b}$$

The impedance at any point on the transmission line is given by the ratio of the voltage to current. The input impedance is the impedance seen looking into the transmission line, toward the load, at a distance x=-1 from the load. The input impedance in its most general form is given by

$$Z_{in} = \frac{V(x=-l)}{I(x=-l)}$$

$$= \frac{V_o^+(e^{-\gamma(-l)} + \Gamma_L e^{\gamma(-l)})}{\frac{V_o^+}{Z_o}(e^{-\gamma(-l)} - \Gamma_L e^{\gamma(-l)})}$$

$$= Z_o \frac{(e^{\gamma l} + \Gamma_L e^{-\gamma l})}{(e^{\gamma l} - \Gamma_L e^{-\gamma l})}.$$
(3.24)

Using the reflection coefficient from (3.22) in (3.24) yields:

$$Z_{in} = Z_{o} \frac{\left(e^{\gamma l} + \left(\frac{Z_{L} - Z_{o}}{Z_{L} + Z_{o}}\right)e^{-\gamma l}\right)}{\left(e^{\gamma l} - \left(\frac{Z_{L} - Z_{o}}{Z_{L} + Z_{o}}\right)e^{-\gamma l}\right)}$$

$$= Z_{o} \frac{\left(\left(Z_{L} + Z_{o}\right)e^{\gamma l} + \left(Z_{L} - Z_{o}\right)e^{-\gamma l}\right)}{\left(\left(Z_{L} + Z_{o}\right)e^{\gamma l} - \left(Z_{L} - Z_{o}\right)e^{-\gamma l}\right)}$$

$$= Z_{o} \frac{Z_{L}\left(e^{\gamma l} + e^{-\gamma l}\right) + Z_{o}\left(e^{\gamma l} - e^{-\gamma l}\right)}{Z_{o}\left(e^{\gamma l} + e^{-\gamma l}\right) + Z_{L}\left(e^{\gamma l} - e^{-\gamma l}\right)}$$

$$= Z_{o} \frac{2Z_{L}\cosh\gamma l + 2Z_{o}\sinh\gamma l}{2Z_{o}\cosh\gamma l + 2Z_{L}\sinh\gamma l}$$

$$= Z_{o} \frac{Z_{L} + Z_{o}\tanh\gamma l}{Z_{o} + Z_{L}\tanh\gamma l}.$$
(3.25)

The conducting septum of the HMLWA antenna is analogous to a special case of loaded transmission lines: the short-circuited loaded line. This special case will be discussed in the following section.

3.2.1 Short-Circuited Line

A short-circuited transmission line is characterized by a load impedance of $Z_L=0$, and is depicted in Figure 3.3. Therefore, the voltage reflection coefficient is $\Gamma_L=-1$, governed by Equation (3.22). The voltage and current on a short-circuited transmission line are given by substituting $\Gamma_L=-1$ into equations (3.23a) and (3.23b) resulting in

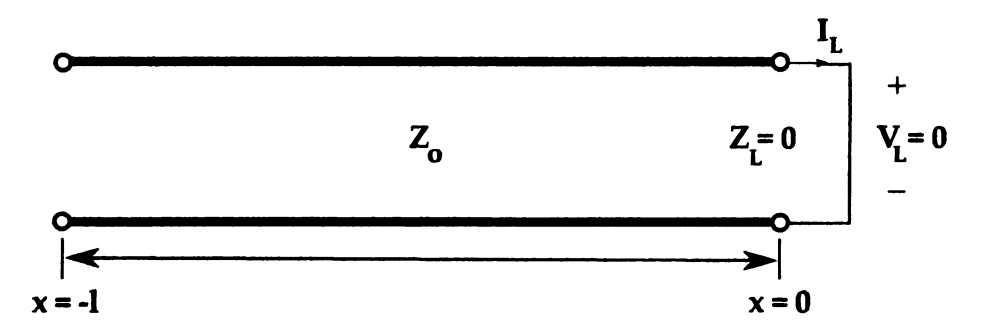


Figure 3.3. Short-circuited transmission line.

$$V(x) = V_o^+(e^{-\gamma x} - e^{\gamma x})$$
 (3.26)

and

$$I(x) = \frac{V_o^+}{Z_o} (e^{-\gamma x} + e^{\gamma x})$$
 (3.27)

which become

$$V(x) = -V_o^+(e^{\gamma x} - e^{-\gamma x})$$
$$= -2V_o^+ \sinh \gamma x \tag{3.28}$$

and

$$I(x) = \frac{V_o^+}{Z_o} (e^{-\gamma x} + e^{\gamma x})$$

$$= 2 \frac{V_o^+}{Z_o} \cosh \gamma x. \tag{3.29}$$

The input impedance of a short-circuited transmission line is determined by substituting $\mathbf{Z}_L = 0$ into Equation (3.25)

$$Z_{in} = \frac{V(x=-l)}{I(x=-l)}$$

$$= Z_o \frac{(0) + Z_o \tanh \gamma l}{Z_o + (0) \tanh \gamma l}$$

$$= Z_o \tanh \gamma l. \tag{3.30}$$

where symmetry of the sinusoidal functions was invoked.

3.3 Transverse Resonance Relation

The TRM method is valid as long as the transverse resonance relation is maintained. This relation can be viewed as a boundary condition invoking continuity of impedances across a mathematical boundary. It states that the input impedance

to the left of the boundary is equal and opposite the impedance to the right of the boundary. This is mathematically represented as

$$Z_{in}^{x^{-}} + Z_{in}^{x^{+}} = 0. (3.31)$$

Equation (3.31) is derived by invoking boundary conditions on the tangential electric and magnetic fields at the boundary $x=-\frac{w}{2}$ (see Figure 3.4). The tangential boundary conditions that must be obeyed are:

$$\widehat{n} \times (\overrightarrow{E}^{+} - \overrightarrow{E}^{-}) = -\overrightarrow{M} \tag{3.32a}$$

$$\widehat{n} \times (\overrightarrow{H}^+ - \overrightarrow{H}^-) = \overrightarrow{J}, \tag{3.32b}$$

where $\hat{n} = \hat{x}$ is oriented from left to right, i.e., originating in the negative region and pointing toward the positive region. Since the region within the HMLWA antenna is source free, the tangential boundary conditions reduce to

$$\widehat{x} \times (\overrightarrow{E}^+ - \overrightarrow{E}^-) = 0 \tag{3.33a}$$

$$\widehat{x} \times (\overrightarrow{H}^+ - \overrightarrow{H}^-) = 0, \tag{3.33b}$$

resulting in the following continuous components:

$$E_{y}^{+} = E_{y}^{-} \tag{3.34a}$$

$$E_z^+ = E_z^- (3.34b)$$

$$H_y^+ = H_y^-$$
 (3.34c)

$$H_z^+ = H_z^-.$$
 (3.34d)

The directional wave impedance is obtained by dividing the electric field component by the corresponding orthogonal magnetic field component [22]. It is governed by the following expression

$$Z^k = \frac{E^i}{H^j} = -\frac{E^j}{H^i},\tag{3.35}$$

where $\hat{k} = \hat{i} \times \hat{j}$ abides by the cyclic nature of the cross product. The wave impedance in the positive x-direction is

$$Z^{x^{+}} = \frac{E^{y^{+}}}{H^{z^{+}}} = -\frac{E^{z^{+}}}{H^{y^{+}}},\tag{3.36}$$

while that in the negative x-direction is given by

$$Z^{x^{-}} = \frac{E^{z^{-}}}{H^{y^{-}}} = -\frac{E^{y^{-}}}{H^{z^{-}}}. (3.37)$$

Substituting (3.34a) and (3.34d) into (3.36) gives

$$Z^{x^+} = \frac{E^{y^-}}{H^{z^-}}. (3.38)$$

The right hand side of (3.38) is equal to $-Z^{x^{-}}$ given by (3.37), and leads to

$$Z^{x^+} = -Z^{x^-}, (3.39)$$

the transverse resonance relation.

An alternative form of the transverse resonance relation may be derived by determining the voltage reflection coefficient at the boundary $\mathbf{x} = -\frac{w}{2}$. Substituting $Z_{in}^{x^-}$ and $Z_{in}^{x^+}$ into equation (3.22) gives

$$\Gamma_{in}^{x^{-}} = \frac{Z_{in}^{x^{-}} - Z_{o}}{Z_{in}^{x^{-}} + Z_{o}} \tag{3.40}$$

and

$$\Gamma_{in}^{x^+} = \frac{Z_{in}^{x^+} - Z_o}{Z_{in}^{x^+} + Z_o},\tag{3.41}$$

the reflection coefficients to the left and right of the boundary $x=-\frac{w}{2}$, respectively. Solving equations (3.40) and (3.41) for $Z_{in}^{x^-}$ and $Z_{in}^{x^+}$ gives

$$Z_{in}^{x^{-}} = Z_{o} \frac{1 + \Gamma_{in}^{x^{-}}}{1 - \Gamma_{in}^{x^{-}}}$$
 (3.42a)

$$Z_{in}^{x^{+}} = Z_{o} \frac{1 + \Gamma_{in}^{x^{+}}}{1 - \Gamma_{in}^{x^{+}}}.$$
 (3.42b)

The sum of (3.42a) and (3.42b)

$$Z_{in}^{x^{-}} + Z_{in}^{x^{+}} = Z_{o} \frac{1 + \Gamma_{in}^{x^{-}}}{1 - \Gamma_{in}^{x^{-}}} + Z_{o} \frac{1 + \Gamma_{in}^{x^{+}}}{1 - \Gamma_{in}^{x^{+}}} = 0,$$
(3.43)

invokes the transverse resonance relation, equation (3.31). Further algebraic manipulation leads to:

$$Z_{o} \frac{1 + \Gamma_{in}^{x^{-}}}{1 - \Gamma_{in}^{x^{-}}} + Z_{o} \frac{1 + \Gamma_{in}^{x^{+}}}{1 - \Gamma_{in}^{x^{+}}} = 0$$

$$\frac{1 + \Gamma_{in}^{x^{-}}}{1 - \Gamma_{in}^{x^{-}}} + \frac{1 + \Gamma_{in}^{x^{+}}}{1 - \Gamma_{in}^{x^{+}}} = 0$$

$$\frac{(1 + \Gamma_{in}^{x^{-}})(1 - \Gamma_{in}^{x^{+}}) + (1 + \Gamma_{in}^{x^{+}})(1 - \Gamma_{in}^{x^{-}})}{(1 - \Gamma_{in}^{x^{-}})(1 - \Gamma_{in}^{x^{+}})} = 0$$

$$(1 + \Gamma_{in}^{x^{-}})(1 - \Gamma_{in}^{x^{+}}) + (1 + \Gamma_{in}^{x^{+}})(1 - \Gamma_{in}^{x^{-}}) = 0$$

$$2 - 2\Gamma_{in}^{x^{-}}\Gamma_{in}^{x^{+}} = 0$$

$$\Gamma_{in}^{x^{-}}\Gamma_{in}^{x^{+}} = 1, \qquad (3.44)$$

a more usable form of the transverse resonance relation.

3.4 TRM method applied to an unloaded HMLWA antenna

Before the TRM method is applied to the edge-loaded HMLWA antenna, the simpler unloaded case will be presented. Once the unloaded case is explained in detail, the

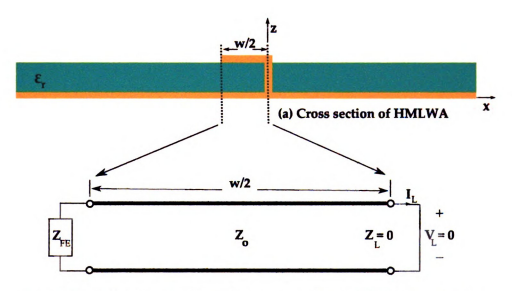


Figure 3.4. TRM method applied to an unloaded HMLWA antenna.

edge-loaded case is determined by expounding upon this simpler, but non-trivial model.

It is evident from the transverse resonance relation (equation (3.44)) that an a priori knowledge of the reflection coefficients on both sides of the mathematical boundary is required. The reflection coefficient looking to the right is that of a short-circuited transmission line transformed to the mathematical boundary (placed at the radiating edge of the HMLWA antenna) $\mathbf{x} = -\frac{w}{2}$. The reflection coefficient due to a

shorted transmission line is negative one, given by:

$$\Gamma_L^{short} = \frac{Z_L - Z_o}{Z_L + Z_o}$$

$$= \frac{0 - Z_o}{0 + Z_o}$$

$$= \frac{-Z_o}{Z_o}$$

$$= -1, \qquad (3.45)$$

where the impedance of a short-circuited load is zero. But the input reflection coefficient at the mathematical boundary $\mathbf{x} = -\frac{w}{2}$, a distance $\frac{w}{2}$ from the short, must account for this displacement. The input reflection coefficient at the boundary $\mathbf{x} = -\frac{w}{2}$ can be computed by determining the ratio of the magnitude of the reflected voltage wave to that of the incident wave, i.e.

$$\Gamma(x) = \frac{V_o^- e^{\gamma_T x}}{V_o^+ e^{-\gamma_T x}},\tag{3.46}$$

which reduces to

$$\Gamma(x) = \frac{V_o^- e^{jk_T x}}{V_o^+ e^{-jk_T x}},\tag{3.47}$$

for waves propagating and attenuating in the x-direction. Transverse wave number k_T is the wave number transverse to the direction of propagation, and is defined as

$$k_T = \beta_{\zeta} - j\alpha_{\zeta},\tag{3.48}$$

where $\zeta=x$, z. Moving the exponential term in the denominator to the numerator yields

$$\Gamma(x) = \frac{V_o^- e^{j2k_T x}}{V_o^+}. (3.49)$$

The voltage reflection coefficient at the load follows upon substituting x=0 into equa-

tion (3.49),

$$\Gamma(0) = \frac{V_o^- e^{j2k_T(0)}}{V_o^+}$$

$$\Gamma_L = \frac{V_o^-}{V_o^+}.$$
(3.50)

Substituting $x=-\frac{w}{2}$ into equation (3.49) yields the input reflection coefficient at the reference plane given by

$$\Gamma_{in}^{x^{+}}(-\frac{w}{2}) = \frac{V_{o}^{-}e^{j2k_{T}(-\frac{w}{2})}}{V_{o}^{+}} \\
= \frac{V_{o}^{-}e^{-jk_{T}w}}{V_{o}^{+}}.$$
(3.51)

Recall equation (3.50) which states that the reflection coefficient at the load is the ratio of the reflected to incident waves. Substituting this into equation (3.51) gives

$$\Gamma_{in}^{x^{+}}(x) = \frac{V_{o}^{-}e^{-jk_{T}w}}{V_{o}^{+}}$$

$$= \Gamma_{L}e^{-jk_{T}w}.$$
(3.52)

Substituting the reflection coefficient of a short-circuited transmission line from equation (3.45) yields

$$\Gamma_{in}^{x^+}(x) = -e^{-jk_T w},\tag{3.53}$$

the input reflection coefficient looking to the right of the mathematical boundary, $x=-\frac{w}{2}$. Here, k_T is the transverse wave number given by $k_T=\sqrt{k_x^2+k_z^2}$.

The reflection coefficient looking to the left is not as trivial. The discontinuity presented by the abrupt end of the conducting strip, while the substrate and ground plane continue, introduces a significant amount of reflection for waves propagating in the substrate. This phenomenon is thoroughly explained in [8] where the authors

give the reflection coefficient at this interface. Using their notation, the reflection coefficient looking to the left is written as

$$\Gamma_{in}^{x^-}(x) = e^{j\chi(k_T)},\tag{3.54}$$

where $\chi(k_T)$ is a complex function of k_T defined in equation (3.70) of Section 3.5.

Substituting (3.53) and (3.54) into (3.44) enforces the transverse resonance relation and leads to the following transcendental equation

$$-e^{-jk_Tw} \times e^{j\chi(k_T)} = 1. \tag{3.55}$$

Figure 3.4 depicts application of the TRM method to the unloaded HMLWA antenna. Multiplying both sides of (3.55) by negative one leads to

$$e^{-jk_T w} \times e^{j\chi(k_T)} = -1, \tag{3.56}$$

and realizing that $-1 = e^{\pm jn\pi}$ for odd n gives

$$e^{-jk_T w} \times e^{j\chi(k_T)} = e^{\pm jn\pi}. (3.57)$$

Dividing both sides by $e^{\pm jn\pi}$ gives

$$\frac{e^{-jk_T w} \times e^{j\chi(k_T)}}{e^{\pm jn\pi}} = 1$$

$$e^{-jk_T w} \times e^{j\chi(k_T)} \times e^{\mp jn\pi} = 1$$

$$e^{j(\chi(k_T) - k_T w \mp n\pi)} = 1.$$
(3.58)

Taking the natural logarithm leads to

$$\ln(e^{j(\chi(k_T) - k_T w \mp n\pi)}) = 0. \tag{3.59}$$

The term within the parenthesis of equation (3.59) is a complex quantity. It can be recast in the general exponential form of $z = re^{j\rho}$, where $r = |e^{j(\chi(k_T) - k_T w \mp n\pi)}| = 1$ and $\rho = \arg(e^{j(\chi(k_T) - k_T w \mp n\pi)}) = \chi(k_T) - k_T w \mp n\pi$. This complex quantity is muti-valued, and its value depends on which Riemann sheet, or branch, it lies on. There are an infinite number of sheets which are traversed by increasing multiples of $2\pi m$ where m, an integer, isolates one sheet where the multi-valued quantity is single-valued. Therefore, the natural logarithm of a complex quantity is given by

$$\ln(z) = \ln r + \ln e^{j\rho}$$

$$= \ln r + j\rho + j2\pi m$$

$$= \ln r + j(\rho + 2\pi m). \tag{3.60}$$

Applying this definition to (3.59) leads to

$$\ln(1) + j(\chi(k_T) - k_T w \mp n\pi) + j2\pi m = 0$$

$$j(\chi(k_T) - k_T w \mp n\pi + 2\pi m) = 0$$

$$\chi(k_T) - k_T w + \pi(2m \mp n) = 0,$$
(3.61)

but since $(2m \mp n)$ results in an integer, conveniently allowing this integer to be n yields

$$\chi(k_T) - k_T w + n\pi = 0. (3.62)$$

For the hybrid leaky-wave EH₁ mode, n = 1 [21] and (3.62) becomes

$$\chi(k_T) - k_T w + \pi = 0. (3.63)$$

Equation (3.63) contains one unknown, the transverse wave number k_T , which is determined by finding the root of the function. Once k_T is known, the axial wave number k_y can be determined by solving the constraint equation,

$$k_T^2 + k_y^2 = k^2. (3.64)$$

Solving for k_y yields

$$k_y^2 = k^2 - k_T^2 k_y = \sqrt{k^2 - k_T^2} k_y = \sqrt{\epsilon_r k_0^2 - k_T^2},$$
 (3.65)

where k_0 is the free-space wavenumber given by $k_0 = \omega \sqrt{\mu_0 \epsilon_0}$. The normalized leakage and phase coefficients are easily extracted from k_y as

$$\alpha(\omega) = Im\left\{\frac{k_y}{k_0}\right\} \tag{3.66}$$

and

$$\beta(\omega) = Re\left\{\frac{k_y}{k_0}\right\},\tag{3.67}$$

respectively. Dispersion curves of the leaky EH₁ mode on an unloaded HMLWA antenna are depicted in Figure 3.5.

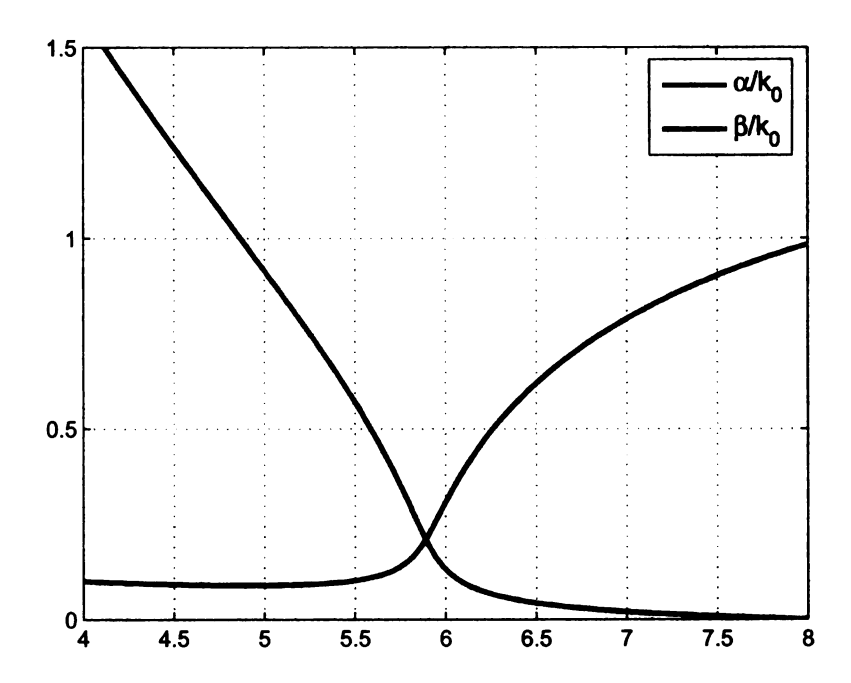


Figure 3.5. Dispersion curves of the hybrid leaky-wave EH_1 mode. Operational region: 5.889-8.115 GHz. BW=31.80%.

3.5 Free-edge Admittance

Chang and Kuester investigated oblique incidence of a TEM wave incident upon the open end of a parallel-plate waveguide with a truncated upper plate [8]. This can be used as a simple model for the open edge of the HMLWA antenna. They employed a Wiener-Hopf technique to determine the reflection coefficient at the open edge of the structure. They used this reflection coefficient to define the free-edge admittance as

$$Y_{FE}(k_T) = \frac{\sqrt{\frac{\epsilon_r}{\mu_r}}}{j\eta_o} \tan \frac{\chi(k_T)}{2}.$$
 (3.68)

The reciprocal of the admittance results in the free-edge impedance,

$$Z_{FE}(k_T) = \frac{j\eta_o}{\sqrt{\epsilon_r}} \cot \frac{\chi(k_T)}{2}, \qquad (3.69)$$

where $\mu_r=1$ for a non-magnetic substrate. Figure C.1 depicts the resistance of the free-edge impedance while Figure C.2 depicts the reactance. An alternative to using the rigorous Wiener-Hopf technique to determine the free-edge impedance is given in [2]. Here, a y-polarized Gaussian pulse is excited at one end of the microstrip (between the conducting strip and the ground plane), and the impedance at the opposite end, the free-edge, is determined by taking the ratio of the Fourier transforms of the y-polarized electric to z-polarized magnetic fields.

The $\chi(k_T)$ term within the argument of the cotangent function is given by

$$\chi(k_T) = 2 \tan^{-1} \left(\frac{\sqrt{k^2 - k_T^2}}{k_T} \tanh \Delta(k_T) \right) - f_e(k_T),$$
(3.70)

where $\Delta(k_T)$ and $f_e(k_T)$ are given in [33], based on results reported by Chang and Kuester, and are repeated here:

$$\Delta(k_T) = \frac{h\sqrt{k^2 - k_T^2}}{\pi} \left[\frac{1 - \epsilon_r}{\epsilon_r} \left(\ln\left(jh\sqrt{k_0^2 - k^2 + k_T^2}\right) + \gamma - 1 \right) + 2Q(-\delta_\epsilon) - \frac{1}{(3.71)} - 2Q(\delta_\mu) \right],$$

and

$$f_e(k_T) = \frac{-2k_T h}{\pi} \left[\frac{\ln \left(jh\sqrt{k_0^2 - k^2 + k_T^2} \right) + \gamma - 1}{\epsilon_r} + 2Q(-\delta_\epsilon) - \ln(2\pi) \right]. \quad (3.72)$$

Here γ , Euler's constant, is defined as $\gamma=0.577215665$, and the other constants are

defined as:

$$\delta_{\epsilon} = \frac{\epsilon_r - 1}{\epsilon_r + 1} \tag{3.73}$$

$$\delta_{\mu} = \frac{\mu_r - 1}{\mu_r + 1}$$

$$= 0 \tag{3.74}$$

$$Q(-\delta_{\epsilon}) = \sum_{m=1}^{\infty} \left[-\frac{\epsilon_r - 1}{\epsilon_r + 1} \right]^m \ln(m)$$
 (3.75a)

$$Q(-\delta_{\mu}) = 0|_{\mu_r = 1} \tag{3.75b}$$

Figure 3.6 depicts that for ϵ_r =2.33, Q($-\delta_\epsilon$) converges with at least m=15 terms in the series. $\Delta(k_T)$ and $f_e(k_T)$ are reexpressed as

$$\Delta(k_T) = \frac{h\sqrt{k^2 - k_T^2}}{\pi} \left[\frac{1 - \epsilon_r}{\epsilon_r} (\ln(jh\sqrt{k_0^2 - k^2 + k_T^2}) + \gamma - 1) + 2\sum_{m=1}^{\infty} \left[-\frac{\epsilon_r - 1}{\epsilon_r + 1} \right]^m \ln(m) \right],$$
(3.76)

and

$$f_e(k_T) = \frac{-2k_T h}{\pi} \left[\frac{\ln\left(jh\sqrt{k_o^2 - k^2 + k_T^2}\right) + \gamma - 1}{\epsilon_r} + 2\sum_{m=1}^{\infty} \left[-\frac{\epsilon_r - 1}{\epsilon_r + 1} \right]^m \ln(m) - \ln(2\pi) \right]$$

$$(3.77)$$

upon substituting equation (3.75) into equations (3.71) and (3.72), respectively.

Finally, an expression for $\chi(k_T)$ is derived showing its explicit dependence on the

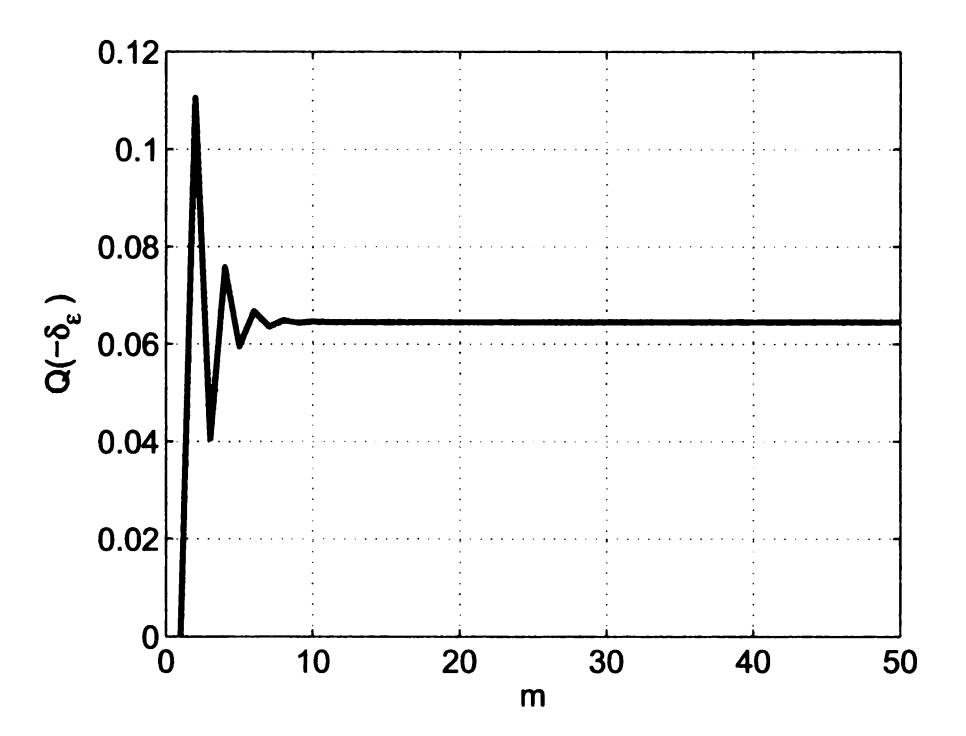


Figure 3.6. Convergence of $Q(-\delta_{\epsilon})$ vs. m for ϵ_r =2.33.

transverse wave number, k_T . Substituting equations (3.76) and (3.77) into (3.70) yields

$$\chi(k_T) = 2 \tan^{-1} \left(\frac{\sqrt{k_0^2 - k_T^2}}{k_T} \tanh \left[\frac{h(1 - \epsilon_r) \sqrt{k_0^2 - k_T^2}}{\pi \epsilon_r} (\ln(jhk_T) + \gamma') + \frac{h\sqrt{k_0^2 - k_T^2}}{\pi} \sum_{m=1}^{\infty} \left[-\frac{\epsilon_r - 1}{\epsilon_r + 1} \right]^m \ln(m) \right] \right) + \frac{2k_T h}{\pi} \left[\frac{\ln(jhk_T) + \gamma'}{\epsilon_r} + 2 \sum_{m=1}^{\infty} \left[-\frac{\epsilon_r - 1}{\epsilon_r + 1} \right]^m \ln(m) - \ln(2\pi) \right],$$
(3.78)

the final expression for $\chi(k_T)$, as derived by Chang and Kuester, where $\gamma' = \gamma - 1$.

Equations (3.68) through (3.78) are valid for electrically thin substrates, where $k_0 \epsilon_r h \ll 1$.

3.6 TRM method applied to a reactively loaded HMLWA antenna

The impedance to the left of the boundary, given by

$$Z_{in}^{x^{-}}(x') = Z_{o} \left[\frac{Z_{RE} + jZ_{o}tan(k_{x}x')}{Z_{o} + jZ_{RE}tan(k_{x}x')} \right], \tag{3.79}$$

is derived in Section 3.2. The impedance to the right of the boundary

$$Z_{in}^{x^+}(x') = jZ_o tan(k_x x'),$$
 (3.80)

derived in Section 3.2.1, is the input impedance of a short-circuited transmission line. The radiating-edge impedance denoted by Z_{RE} in equation (3.79), is the parallel combination of the free-edge impedance and the impedance of the lumped element placed in shunt with the radiating edge, given by

$$Z_{RE} = \frac{Z_{Load} \times Z_{FE}(k_T)}{Z_{Load} + Z_{FE}(k_T)}.$$
(3.81)

Substituting Z_{FE} from equation (3.69) yields

$$Z_{RE} = \frac{Z_{Load} \times \frac{j\eta_o}{\sqrt{\epsilon_r}} \cot \frac{\chi(k_T)}{2}}{Z_{Load} + \frac{j\eta_o}{\sqrt{\epsilon_r}} \cot \frac{\chi(k_T)}{2}}.$$
 (3.82)

The following analysis employs equation (3.44) because it is less laborious to manipulate reflection coefficients than input impedances. The reflection coefficient looking to the right, that of a short circuited load transformed to the boundary $\mathbf{x} = -\frac{w}{2}$, is derived in Section 3.4 and is repeated here:

$$\Gamma_{in}^{x^+}(x) = -e^{-jk_T w}. (3.83)$$

The characteristic impedance is required to determine the reflection coefficient looking to the left, evident from equation (3.22). The wave impedance of a TEM plane wave propagating through a dielectric, characterized by a relative permittivity of ϵ_r , is used for the characteristic impedance [2] and is given by

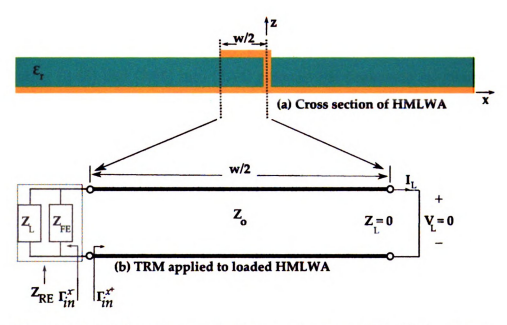


Figure 3.7. TRM method applied to an edge-loaded HMLWA antenna.

$$Z_o = \frac{\eta_o}{\sqrt{\epsilon_r}},\tag{3.84}$$

where η_0 , the intrinsic impedance of free space, has a value of $\sqrt{\frac{\mu_0}{\epsilon_0}} \approx 120\pi~\Omega$.

Post application of equation (3.22), the reflection coefficient looking to the left of the boundary $\mathbf{x} = -\frac{w}{2}$ is given as

$$\Gamma_{in}^{x^-}(x) = \frac{Z_{RE}(k_T) - Z_o}{Z_{DE}(k_T) + Z_o},$$
(3.85)

and substituting equations (3.82) and (3.84) yields

$$\Gamma_{in}^{x^{-}}(x) = \frac{\left(\frac{Z_{Load} \times \frac{j\eta_{o}}{\sqrt{\epsilon_{r}}} \cot \frac{\chi(k_{T})}{2}}{Z_{Load} + \frac{j\eta_{o}}{\sqrt{\epsilon_{r}}} \cot \frac{\chi(k_{T})}{2}}\right) - \frac{\eta_{o}}{\sqrt{\epsilon_{r}}}}{\left(\frac{Z_{Load} \times \frac{j\eta_{o}}{\sqrt{\epsilon_{r}}} \cot \frac{\chi(k_{T})}{2}}{Z_{Load} + \frac{j\eta_{o}}{\sqrt{\epsilon_{r}}} \cot \frac{\chi(k_{T})}{2}}\right) + \frac{\eta_{o}}{\sqrt{\epsilon_{r}}}} \tag{3.86}$$

Substituting (3.83) and (3.86) into (3.44) enforces the transverse resonance relation leading to the following transcendental equation

$$\left[\frac{\left(\frac{Z_{Load} \times \frac{j\eta_o}{\sqrt{\epsilon_r}} \cot \frac{\chi(k_T)}{2}}{Z_{Load} + \frac{j\eta_o}{\sqrt{\epsilon_r}} \cot \frac{\chi(k_T)}{2}} \right) - \frac{\eta_o}{\sqrt{\epsilon_r}}}{\left(\frac{Z_{Load} \times \frac{j\eta_o}{\sqrt{\epsilon_r}} \cot \frac{\chi(k_T)}{2}}{Z_{Load} + \frac{j\eta_o}{\sqrt{\epsilon_r}} \cot \frac{\chi(k_T)}{2}} \right) + \frac{\eta_o}{\sqrt{\epsilon_r}}} \right] \times (-e^{-jk_T w}) = 1.$$
(3.87)

Figure 3.7 depicts application of the TRM method to the edge-loaded HMLWA antenna. Multiplying both sides of (3.87) by negative one yields

$$\left[\frac{\left(\frac{Z_{Load} \times \frac{j\eta_o}{\sqrt{\epsilon_r}} \cot \frac{\chi(k_T)}{2}}{Z_{Load} + \frac{j\eta_o}{\sqrt{\epsilon_r}} \cot \frac{\chi(k_T)}{2}} \right) - \frac{\eta_o}{\sqrt{\epsilon_r}}}{\left(\frac{Z_{Load} \times \frac{j\eta_o}{\sqrt{\epsilon_r}} \cot \frac{\chi(k_T)}{2}}{Z_{Load} + \frac{j\eta_o}{\sqrt{\epsilon_r}} \cot \frac{\chi(k_T)}{2}} \right) + \frac{\eta_o}{\sqrt{\epsilon_r}}} \right] \times e^{-jk_T w} = -1,$$
(3.88)

and realizing that $-1 = e^{\pm jn\pi}$ for odd n gives

$$\left[\frac{\left(\frac{Z_{Load} \times \frac{j\eta_o}{\sqrt{\epsilon_r}} \cot \frac{\chi(k_T)}{2}}{Z_{Load} + \frac{j\eta_o}{\sqrt{\epsilon_r}} \cot \frac{\chi(k_T)}{2}} \right) - \frac{\eta_o}{\sqrt{\epsilon_r}}}{\left(\frac{Z_{Load} \times \frac{j\eta_o}{\sqrt{\epsilon_r}} \cot \frac{\chi(k_T)}{2}}{Z_{Load} + \frac{j\eta_o}{\sqrt{\epsilon_r}} \cot \frac{\chi(k_T)}{2}} \right) + \frac{\eta_o}{\sqrt{\epsilon_r}}} \right] \times e^{-jk_T w} = e^{\pm jn\pi}.$$
(3.89)

Multiplying both sides by e^{+jk_Tw} gives

$$\left[\frac{\left(\frac{Z_{Load} \times \frac{j\eta_o}{\sqrt{\epsilon_r}} \cot \frac{\chi(k_T)}{2}}{Z_{Load} + \frac{j\eta_o}{\sqrt{\epsilon_r}} \cot \frac{\chi(k_T)}{2}} \right) - \frac{\eta_o}{\sqrt{\epsilon_r}}}{\left(\frac{Z_{Load} \times \frac{j\eta_o}{\sqrt{\epsilon_r}} \cot \frac{\chi(k_T)}{2}}{Z_{Load} + \frac{j\eta_o}{\sqrt{\epsilon_r}} \cot \frac{\chi(k_T)}{2}} \right) + \frac{\eta_o}{\sqrt{\epsilon_r}}} \right] = e^{j(\pm n\pi + k_T w)},$$
(3.90)

and taking the natural logarithm of both sides leads to

$$\ln \left| \frac{\left(\frac{Z_{Load} \times \frac{j\eta_o}{\sqrt{\epsilon_r}} \cot \frac{\chi(k_T)}{2}}{Z_{Load} + \frac{j\eta_o}{\sqrt{\epsilon_r}} \cot \frac{\chi(k_T)}{2}} \right) - \frac{\eta_o}{\sqrt{\epsilon_r}}}{\left(\frac{Z_{Load} \times \frac{j\eta_o}{\sqrt{\epsilon_r}} \cot \frac{\chi(k_T)}{2}}{Z_{Load} + \frac{j\eta_o}{\sqrt{\epsilon_r}} \cot \frac{\chi(k_T)}{2}} \right) + \frac{\eta_o}{\sqrt{\epsilon_r}}} \right| + j2\pi m = j(\pm n\pi + k_T w), \quad (3.91)$$

post application of (3.60). Rearranging terms gives

$$\ln \left| \frac{\left(\frac{Z_{Load} \times \frac{j\eta_o}{\sqrt{\epsilon_r}} \cot \frac{\chi(k_T)}{2}}{Z_{Load} + \frac{j\eta_o}{\sqrt{\epsilon_r}} \cot \frac{\chi(k_T)}{2}} \right) - \frac{\eta_o}{\sqrt{\epsilon_r}}}{\left(\frac{Z_{Load} \times \frac{j\eta_o}{\sqrt{\epsilon_r}} \cot \frac{\chi(k_T)}{2}}{Z_{Load} + \frac{j\eta_o}{\sqrt{\epsilon_r}} \cot \frac{\chi(k_T)}{2}} \right) + \frac{\eta_o}{\sqrt{\epsilon_r}}} \right| + j2\pi m - j(\pm n\pi + k_T w) = 0, \quad (3.92)$$

and grouping common terms leads to

$$\ln \left| \frac{\left(\frac{Z_{Load} \times \frac{j\eta_o}{\sqrt{\epsilon_r}} \cot \frac{\chi(k_T)}{2}}{Z_{Load} + \frac{j\eta_o}{\sqrt{\epsilon_r}} \cot \frac{\chi(k_T)}{2}} - \frac{\eta_o}{\sqrt{\epsilon_r}} \right|}{\left(\frac{Z_{Load} \times \frac{j\eta_o}{\sqrt{\epsilon_r}} \cot \frac{\chi(k_T)}{2}}{Z_{Load} + \frac{j\eta_o}{\sqrt{\epsilon_r}} \cot \frac{\chi(k_T)}{2}} \right) + \frac{\eta_o}{\sqrt{\epsilon_r}} \right|} + j(2\pi m \mp n\pi - k_T w) = 0.$$
 (3.93)

Further simplification leads to

$$\ln \left| \frac{\left(\frac{Z_{Load} \times \frac{j\eta_o}{\sqrt{\epsilon_r}} \cot \frac{\chi(k_T)}{2}}{Z_{Load} + \frac{j\eta_o}{\sqrt{\epsilon_r}} \cot \frac{\chi(k_T)}{2}} \right) - \frac{\eta_o}{\sqrt{\epsilon_r}}}{\left(\frac{Z_{Load} \times \frac{j\eta_o}{\sqrt{\epsilon_r}} \cot \frac{\chi(k_T)}{2}}{Z_{Load} + \frac{j\eta_o}{\sqrt{\epsilon_r}} \cot \frac{\chi(k_T)}{2}} \right) + \frac{\eta_o}{\sqrt{\epsilon_r}}} \right| + j \left(\pi(2m \mp n) - k_T w \right) = 0$$
 (3.94)

and since $(2m \mp n)$ results in an integer, conveniently allowing this integer to be n

yields

$$\ln \left| \frac{\left(\frac{Z_{Load} \times \frac{j\eta_o}{\sqrt{\epsilon_r}} \cot \frac{\chi(k_T)}{2}}{Z_{Load} + \frac{j\eta_o}{\sqrt{\epsilon_r}} \cot \frac{\chi(k_T)}{2}} \right) - \frac{\eta_o}{\sqrt{\epsilon_r}}}{\left(\frac{Z_{Load} \times \frac{j\eta_o}{\sqrt{\epsilon_r}} \cot \frac{\chi(k_T)}{2}}{Z_{Load} + \frac{j\eta_o}{\sqrt{\epsilon_r}} \cot \frac{\chi(k_T)}{2}} \right) + \frac{\eta_o}{\sqrt{\epsilon_r}}} \right| + j(\pi n - k_T w) = 0.$$
 (3.95)

This reduces to

$$\ln \left| \frac{\left(\frac{Z_{Load} \times \frac{j\eta_o}{\sqrt{\epsilon_r}} \cot \frac{\chi(k_T)}{2}}{Z_{Load} + \frac{j\eta_o}{\sqrt{\epsilon_r}} \cot \frac{\chi(k_T)}{2}} \right) - \frac{\eta_o}{\sqrt{\epsilon_r}}}{\left(\frac{Z_{Load} \times \frac{j\eta_o}{\sqrt{\epsilon_r}} \cot \frac{\chi(k_T)}{2}}{Z_{Load} + \frac{j\eta_o}{\sqrt{\epsilon_r}} \cot \frac{\chi(k_T)}{2}} \right) + \frac{\eta_o}{\sqrt{\epsilon_r}}} \right| + j(\pi - k_T w) = 0$$
(3.96)

since n=1 for the hybrid leaky-wave EH₁ mode [21].

Equation (3.96) contains one unknown, the transverse wave number k_T , which is determined by finding the root of the function. Once k_T is known, the axial wave number k_y can be determined by solving the constraint equation (3.64). Dispersion curves of the hybrid leaky-wave EH₁ mode of a 0.10 pF loaded HMLWA antenna are depicted in Figure 3.8.

Comparing the dispersion curves of Figure 3.5 and Figure 3.8, there are several notable differences, particularly with the operational leaky region and the bandwidth. When loaded, the operational leaky region of the HMLWA antenna decreases. This behavior is expected because loading the antenna with the lumped capacitors essentially slows the propagating wave down. These results are also consistent with those reported in [2] and [5], where the authors state that capacitive loading shifts the operational region down in frequency, while inductive loading shifts the operational region

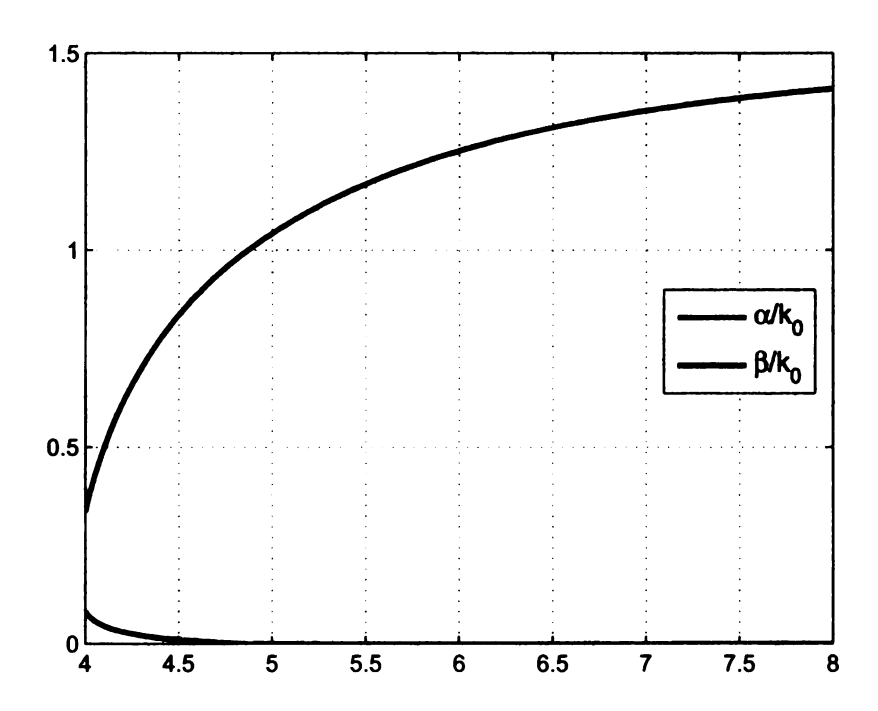
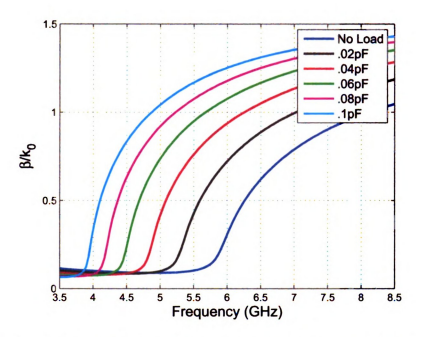


Figure 3.8. Dispersion curves of the hybrid leaky-wave EH₁ mode of a 0.10 pF loaded HMLWA antenna. Operational region: 3.928-4.869 GHz. BW = 21.39%.

to a higher frequency band. The bandwidth, defined as the difference between the exit and entrance of the operational region, i.e., $f(\beta = k_0) - f(\alpha = \beta)$, experiences a significant decrease from 2.26 to 0.95 GHz, 58%.

Figure 3.9 and Figure 3.10 depict the phase and leakage coefficients for various capacitive loads ranging from 0.02 to 0.10 pF. Figure 3.9 shows that when the value of capacitance placed in shunt with the radiating edge of the HMLWA antenna is increased, the microstrip appears to be wider causing the cutoff frequency to shift downward. Table 3.1 lists the lower and upper cutoff frequencies of the EH₁ mode, i.e., $f_{cL} = f(\alpha = \beta)$ and $f_{cU} = f(\beta = k_0)$, respectively, and the bandwidth for each loading configuration depicted in Figure 3.9 and Figure 3.10.



 ${\bf Figure~3.9.}$ Phase coefficients for various capacitive loads ranging from 0.02 to 0.10 ${\bf pF}.$

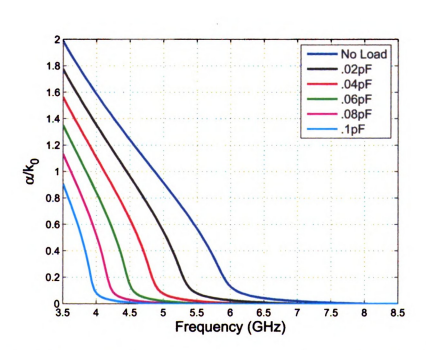


Figure 3.10. Leakage coefficients for various capacitive loads ranging from 0.02 to 0.10 pF.

Table 3.1. Lower cutoff frequency, upper cutoff frequency, and bandwidth of various capacitive loads.

$f_{cL}(GHz)$	$f_{cU}(GHz)$	BW
5.29	7.03	28.16%
4.83	6.25	25.59%
4.47	5.67	23.76%
4.17	5.23	22.39%
3.93	4.87	21.39%
	5.29 4.83 4.47 4.17	5.29 7.03 4.83 6.25 4.47 5.67 4.17 5.23

3.7 TRM method Implementation

The transverse resonance method is implemented in FORTRAN. The FORTRAN code uses the secant method to determine the root (transverse wave number k_T) of equation (3.96). The axial wave number, k_y , follows upon substituting the transverse wave number into (3.64), the constraint equation. The TRM method models a 3-dimensional structure as a 2-dimensional transverse transmission line infinite in extent [21]. Therefore, when a loading configuration is simulated, the method inherently assumes that it is placed all along the radiating edge of the HMLWA antenna, a physically unrealizable configuration when using lumped elements. Hence, the loading configurations are actually per unit length.

To ensure that the radiating edge of the HMLWA antenna is not short- or opencircuited, the impedance regime is determined prior to running the code. The impedance of a capacitor

$$Z_C = \frac{X_C}{j},\tag{3.97}$$

is inversely proportional to the value of capacitance. The numerator in (3.97), the capacitive reactance, is defined below:

$$X_C = \frac{-1}{\omega C}. (3.98)$$

The inversely proportional nature of (3.98) allows for a reduction in the test pool of

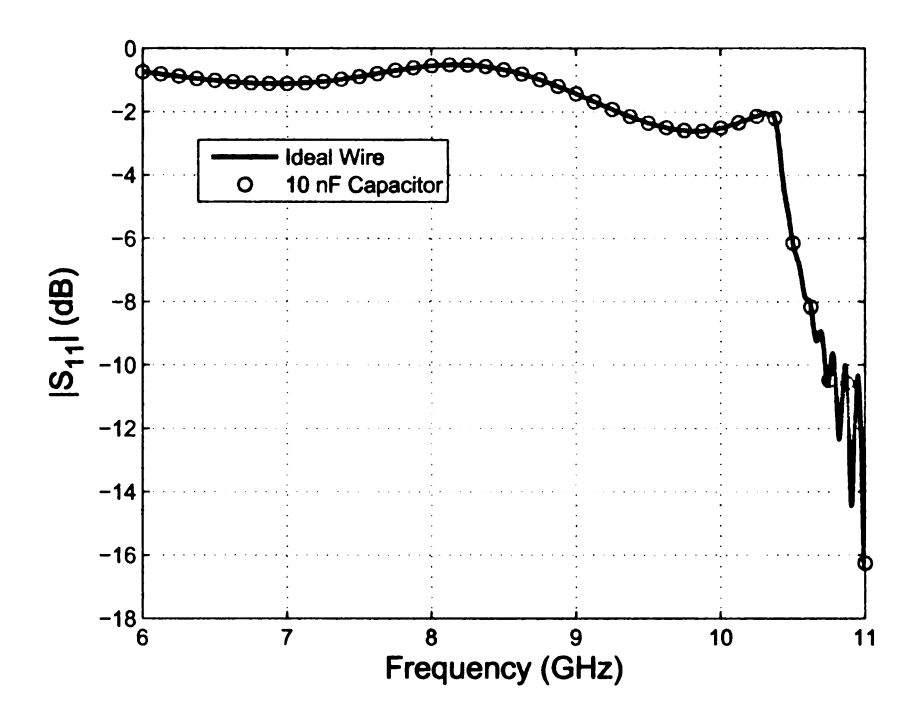


Figure 3.11. 340 mm edge-loaded HMLWA antennas. Loads spaced every 1.5 mm. Depicts how large capacitance value shorts the radiating edge.

candidate capacitors. Capacitors in the nano-Farad range and larger are ignored since the operational frequency, in the gigahertz range, essentially neutralizes their effect. For example, computing the capacitive reactance of a 10 nF capacitor using (3.98) yields a capacitive reactance of X_C =0.002 Ω at 8.00 GHz. This miniscule impedance effectively shorts the radiating edge transforming the antenna into a waveguide or cavity. Figure 3.11 illustrates the agreement between the input reflection coefficients of the 10 nF edge-loaded HMLWA and the ideal wire-loaded HMLWA antennas. It shows that edge loading with 10 nF capacitors is equivalent to shorting the radiating edge of the antenna.

3.8 Fixed Frequency Beam Steering

The purpose of this thesis is to show fixed frequency beam steering of a HMLWA antenna. Although edge loading in the TRM method implies a PUL configuration, a physically unrealizable result, the simulations provide a reasonable amount of insight into the solution, without requiring a full-wave solution. Table 3.3 through Table 3.10 provide the PUL capacitive loading required to fix the main-beam direction of the HMLWA antenna at the specified angle throughout the C-band. The negative entries in the tables represent non-Foster capacitances. This is implemented in the TRM code by changing the sign of the reactive portion of the complex load, Z_{Load} .

Table 3.2 gives the numerical values used to determine the fixed main-beam direction tabulated results reported in Table 3.3 through Table 3.10.

Table 3.2. Capacitive limits used to compute fixed main beam vs. frequency tabulated

Frequency (GHz)	Lower Capacitive Limit (pF)	Upper Capacitive Limit (pF)
4.00	0.00001	1.00
4.50	0.000001	1.00
5.00	0.00001	1.00
5.50	0.000001	1.00
6.00	0.00001	0.10
6.50	0.00001	0.10
7.00	0.00001	0.10
7.50	0.00001	0.10
8.00	0.000001	0.01

All loads consist of lumped capacitors placed in shunt with the radiating edge of the HMLWA antenna. It is assumed that the lumped elements are placed infinitely along the radiating edge with an infinitesimal spacing between consecutive elements. This assumption is reasonable because the TRM method is a 2-dimensional continuous model of the 3-dimensional HMLWA antenna. The angle is measured off broadside, normal to the plane of the antenna. Figure 3.12 is a pictorial representation of the tabulated data reported in Table 3.3 through Table 3.10.

Table 3.3. Capacitive Load required to fix Main Beam at 10° over C-band

Frequency (GHz)	Angle	Lumped Capacitor (pF)	Percent Error WRT 10°
4.00	10.55395	$9.404792946473237 \times 10^{-2}$	5.54%
4.50	10.10443	$5.752970685342671 \times 10^{-2}$	1.04%
5.00	10.58057	$3.151672636318159 \times 10^{-2}$	5.81%
5.50	10.04023	$1.100649174587294 \times 10^{-2}$	0.40%
6.00	10.01043	$-4.851474737368685 \times 10^{-3}$	0.10%
6.50	10.04327	$-1.775805702851426 \times 10^{-2}$	0.43%
7.00	10.00862	$-2.876366983491746 \times 10^{-2}$	0.09%
7.50	10.00392	$-3.846861930965483 \times 10^{-2}$	0.04%
8.00	10.05291	$-4.742318609304652 \times 10^{-2}$	0.53%

Table 3.4. Capacitive Load required to fix Main Beam at 20° over C-band

Frequency (GHz)	Angle	Lumped Capacitor (pF)	Percent Error WRT 20°
4.00	20.49186	0.100551174587294	2.46%
4.50	20.59925	$6.403295197598799 \times 10^{-2}$	2.99%
5.00	20.75909	$3.751972186093047 \times 10^{-2}$	3.79%
5.50	20.16161	$1.700948724362181 \times 10^{-2}$	0.81%
6.00	20.00144	$1.051514757378689 \times 10^{-3}$	0.01%
6.50	20.02314	$-1.190507203601801 \times 10^{-2}$	0.12%
7.00	20.02268	$-2.291068484242121 \times 10^{-2}$	0.11%
7.50	20.05478	$-3.261563431715857 \times 10^{-2}$	0.27%
8.00	20.08793	$-4.157020110055027 \times 10^{-2}$	0.44%

Table 3.5. Capacitive Load required to fix Main Beam at 30° over C-band

Frequency (GHz)	Angle	Lumped Capacitor (pF)	Percent Error WRT 30°
4.00	30.39386	0.109055418209105	1.31%
4.50	30.49723	$7.153669634817408 \times 10^{-2}$	1.66%
5.00	30.21305	$4.402296698349175 \times 10^{-2}$	0.71%
5.50	30.33996	$2.351273236618309 \times 10^{-2}$	1.13%
6.00	30.04200	$7.154505252626313 \times 10^{-3}$	0.14%
6.50	30.04345	$-5.952036018009005 \times 10^{-3}$	0.14%
7.00	30.07277	$-1.695764882441220 \times 10^{-2}$	0.24%
7.50	30.02271	$-2.661257278639320 \times 10^{-2}$	0.08%
8.00	30.07005	$-3.531701200600300 \times 10^{-2}$	0.23%

Table 3.6. Capacitive Load required to fix Main Beam at 40° over C-band

Frequency (GHz)	Angle	Lumped Capacitor (pF)	Percent Error WRT 40°
4.00	40.26788	0.120060909954977	0.67%
4.50	40.29020	$8.104143921960981 \times 10^{-2}$	0.73%
5.00	40.02176	$5.252721060530265 \times 10^{-2}$	0.05%
5.50	40.30084	$3.151672636318159 \times 10^{-2}$	0.75%
6.00	40.03358	$1.470820660330165 \times 10^{-2}$	0.09%
6.50	40.03638	$1.351661830915458 \times 10^{-3}$	0.09%
7.00	40.05529	$-9.753974987493747 \times 10^{-3}$	0.14%
7.50	40.00808	$-1.935887343671836 \times 10^{-2}$	0.02%
8.00	40.03607	$-2.786321060530265\times10^{-2}$	0.09%

Table 3.7. Capacitive Load required to fix Main Beam at 50° over C-band

Frequency (GHz)	Angle	Lumped Capacitor (pF)	Percent Error WRT 50°
4.00	50.19959	0.133067400200100	0.39%
4.50	50.03055	$9.204693096548273 \times 10^{-2}$	0.06%
5.00	50.45237	$6.303245272636318 \times 10^{-2}$	0.90%
5.50	50.06800	$4.052121960980491 \times 10^{-2}$	0.14%
6.00	50.00917	$2.331242271135568 \times 10^{-2}$	0.02%
6.50	50.03428	$9.605706353176589 \times 10^{-3}$	0.07%
7.00	50.04904	$-1.699867433716859 \times 10^{-3}$	0.09%
7.50	50.05514	$-1.130476588294147 \times 10^{-2}$	0.11%
8.00	50.00431	$-1.975907753876939 \times 10^{-2}$	0.01%

Table 3.8. Capacitive Load required to fix Main Beam at 60° over C-band

Frequency (GHz)	Angle	Lumped Capacitor (pF)	Percent Error WRT 60°
4.00	60.31728	0.147074389694847	0.53%
4.50	60.13477	0.104052921960980	0.22%
5.00	60.44472	$7.353769484742370 \times 10^{-2}$	0.74%
5.50	60.00945	$5.002596248124062 \times 10^{-2}$	0.02%
6.00	60.03025	$3.221678589294648 \times 10^{-2}$	0.05%
6.50	60.00767	$1.800982441220611 \times 10^{-2}$	0.01%
7.00	60.00542	$6.404137568784393 \times 10^{-3}$	0.01%
7.50	60.06108	$-3.300683841920961 \times 10^{-3}$	0.10%
8.00	60.00631	$-1.175499549774888 \times 10^{-2}$	0.01%

Table 3.9. Capacitive Load required to fix Main Beam at 70° over C-band

Frequency (GHz)	Angle	Lumped Capacitor (pF)	Percent Error WRT 70°
4.00	70.16352	0.159580630315158	0.23%
4.50	70.27648	0.115058413706853	0.39%
5.00	70.43237	$8.304243771885943 \times 10^{-2}$	0.62%
5.50	70.44967	$5.903045572786392 \times 10^{-2}$	0.64%
6.00	70.03647	$4.022070785392697 \times 10^{-2}$	0.05%
6.50	70.03898	$2.556352576288145 \times 10^{-2}$	0.06%
7.00	70.06608	$1.365769184592296 \times 10^{-2}$	0.09%
7.50	70.04286	$3.702813906953477 \times 10^{-3}$	0.06%
8.00	70.02250	$-4.801449224612306 \times 10^{-3}$	0.03%

Table 3.10. Capacitive Load required to fix Main Beam at 80° over C-band

Frequency (GHz)	Angle	Lumped Capacitor (pF)	Percent Error WRT 80°
4.00	80.68323	0.169085373186593	0.85%
4.50	80.70762	0.123062407703852	0.88%
5.00	80.93887	$9.004593246623310 \times 10^{-2}$	1.17%
5.50	80.26050	$6.503345122561280 \times 10^{-2}$	0.33%
6.00	80.11734	$4.597352676338170 \times 10^{-2}$	0.15%
6.50	80.02818	$3.091614857428715 \times 10^{-2}$	0.04%
7.00	80.08994	$1.876019209604803 \times 10^{-2}$	0.11%
7.50	80.10358	$8.655240620310155 \times 10^{-3}$	0.13%
8.00	80.00903	$3.601400700350175 \times 10^{-5}$	0.01%

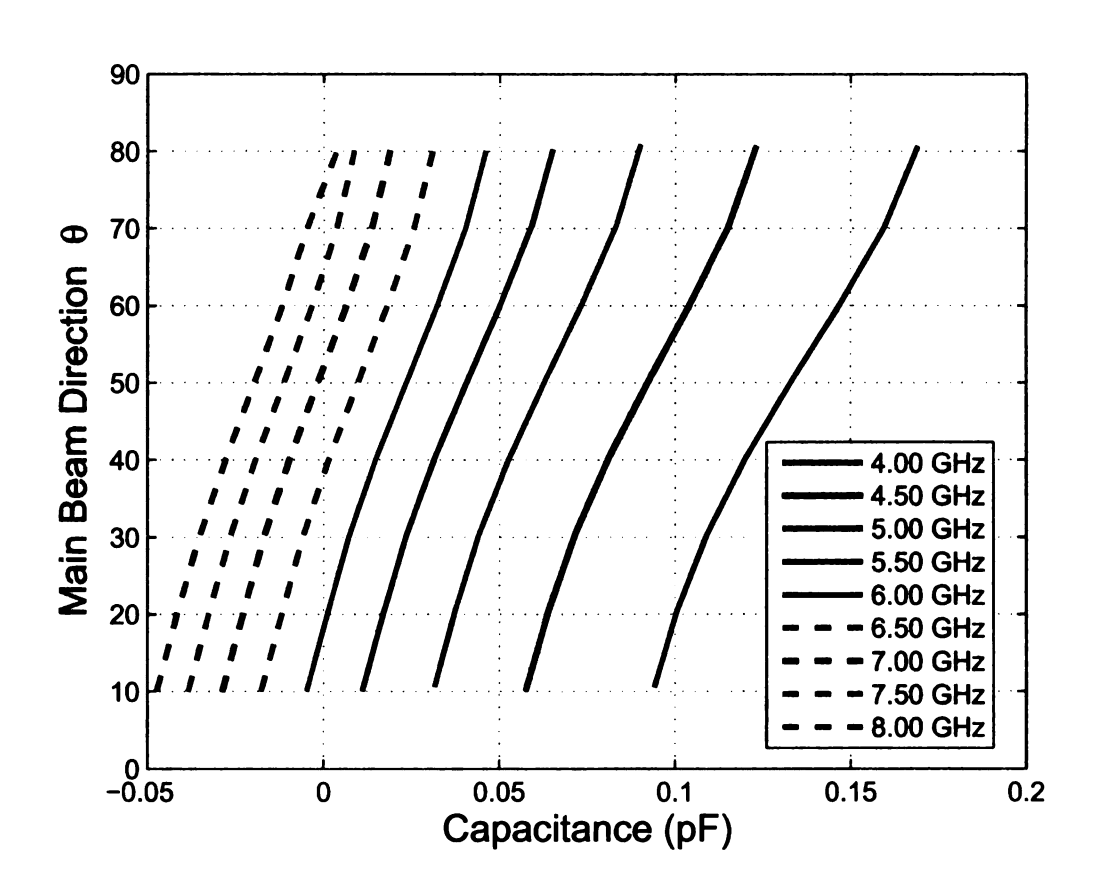


Figure 3.12. Main beam direction vs. Capacitance for various Frequencies.

CHAPTER 4

ANALYTICAL SOLUTION

There are numerous analytical techniques used to determine the field structure within a microstrip antenna including the transmission-line model, the cavity model, and the integral equation method [24]. Of these, the cavity model is appealing because it uses the aperture fields within the dielectric substrate in a fairly straightforward fashion [24]. If the radiation pattern is desired, a particularly simple, mathematically precise, analysis can be used to approximate the pattern of an open-circuited microstrip line [32]. The radiating aperture model is precise if the aperture field distributions are known exactly, but the model yields a fairly accurate pattern even if the aperture fields are approximated. In Section 4.1, the cavity model is used to derive the appropriate boundary conditions that the EM fields must obey at the radiating edge (aperture) of the HMLWA antenna. In Section 4.2 the EM field in the half space z > 0 of the HMLWA antenna is determined which must obey the boundary conditions discussed in Section 4.1.

4.1 Cavity Model of HMLWA antenna

Although patch antennas are resonant standing-wave strucutures, we borrow the analysis method used to derive the EM fields at the conducting-strip edge air interface of a patch to study the HMLWA antenna. This approach has been dubbed the leaky-cavity model and is presented here. Elliott [26] mentions that the electromagnetic properties of a patch (microstrip) antenna can be deduced by viewing it as a leaky cavity, provided that the substrate is electrically thin, i.e. $h \ll \lambda$. This leaky-cavity analysis provides good conceptual knowledge of how fields radiate away from microstrip antennas. The radiation zone fields are computed using the aperture fields within the slots along the patch edges.

If the dielectric substrate and the PEC ground plane of the microstrip antenna are truncated to the dimensions of the patch, the antenna can be viewed as a dielectric loaded cavity (Figure 4.1). The cavity is bound by perfect electric conducting walls

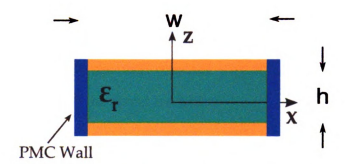


Figure 4.1. Cavity Model of a Microstrip Antenna

on the top and bottom, representative of the conducting strip and the ground plane, and bound by pefect magnetic conducting (PMC) walls on the sides. The PMC walls are included because when the patch is energized, charge distribution is established on the upper and lower surfaces of the conducting strip and on the surface of the ground plane [28]. Grouped like charge under the conducting strip moves to the top of the strip because like charges repel each other. This movement creates two electric current densities, \vec{J}_t , and \vec{J}_b , for current densities on the top and bottom of the conducting strip, respectively. For most microstrips the substrate height-to-width ratio is small, and the opposing charges on the bottom of the strip and top of the ground plane attract; and little, if any, charge moves to the top of the conducting strip. Ideally, as the height-to-width ratio approaches zero, no charge would move to the top of the conducting strip, hence \vec{J}_t =0, and therefore no tangential magnetic fieled exists in the planes forming the edges of the patch. The absence of tangential magnetic fieled salong the edges of the patch are represented in the cavity model by

the inclusion of PMC walls along each edge. The PMC walls ensure that tangential magnetic fields vanish along the side walls by the tangential PMC boundary condition $\hat{n} \times \overrightarrow{H} = 0$.

4.2 The Radiating Aperture Model

In order to use the radiating aperture model, several *a priori* assumptions are made.

The fields in the aperture are assumed constant with a propagating and attenuating behavior along the length of the structure where

$$\vec{E} = \hat{z}E_o e^{-\gamma y}. (4.1)$$

Although Equation (4.1) is reasonable for electrically thin substrates, simulation from CST Microwave Studio verified that the assumption is appropriate for the thicker substrate used for the HMLWA antenna. Figure 4.2 depicts \overrightarrow{E} at two different heights (z=0.40 mm and z=0.55 mm) within the aperture. The fields are approximately equal at both cuts throughout the length of the aperture. As expected, the field attenuates as the wave propagates down the length of the antenna. If reflections are considered from load mismatch, Equation (4.1) becomes

$$\vec{E} = \hat{z}E_o(1+\Gamma)e^{-\gamma y}.$$
(4.2)

For this analysis, Equation (4.1) will be used for the aperture fields because the antenna is sufficiently long (L=340 mm) that 90% of the energy radiates away before reaching the load. Any remaining energy is absorbed by the 50 Ω load. The HMLWA antenna has a half-length $\frac{L}{2}$ =170 mm, conducting strip half-width of $\frac{w}{2}$ =3.80 mm, and dielectric substrate half-height of $\frac{h}{2}$ =0.3935 mm. The antenna is centered at the origin such that the feed is located at y= $\frac{L}{2}$, the load is located at y= $\frac{L}{2}$, the

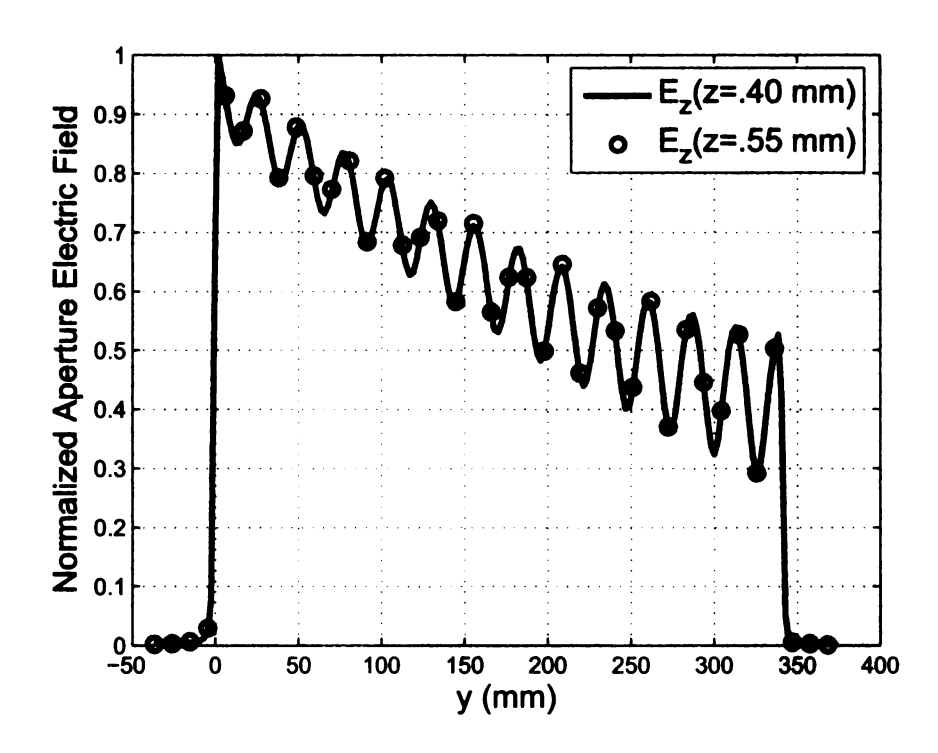


Figure 4.2. Magnitude of the Electric field within the aperture of the HMLWA antenna.

PEC conducting ground plane (of negligible thickness) is located at $z=-\frac{h}{2}$, the PEC conducting strip is located at $z=\frac{h}{2}$, the PEC conducting septum is located at $x=\frac{w}{4}$, and the aperture is located at $x=-\frac{w}{4}$. The antenna geometry is depicted in Figure 4.3.

As discussed in Section 1.1, inclusion of the PEC bifurcating wall slightly perturbs the fields of the EH₁ mode with a noticeable, but negligible, effect on the far-field patterns. The far zone electric field maintained by equivalent magnetic surface current is derived in equation (A.52) of Appendix A. The magnetic surface current on the



Figure 4.3. HMLWA antenna geometry with radiating aperture.

surface bounding the aperture of the HMLWA antenna is given as

$$\overrightarrow{M}(\overrightarrow{r}) = -2\widehat{x} \times (\widehat{z}E_o e^{-\gamma y})$$

$$= 2E_o e^{-\gamma y} \widehat{y}$$

$$= 2E_o e^{-jk_y y} \widehat{y}, \qquad (4.3)$$

a result of the equivalent magentic surface current, $\overrightarrow{M} = \hat{n} \times \overrightarrow{E}$, and $\gamma = jk_y$. For a wave propagating and attenuating in the y-direction, $k_y = (\beta - j\alpha)$ and (4.3) becomes

$$\overrightarrow{M}(\overrightarrow{r}) = 2E_o e^{(-j\beta - \alpha)y} \widehat{y}. \tag{4.4}$$

The far-zone electric field follows upon substituing (4.4) into (A.52) and is given by

$$\overrightarrow{E} \approx \frac{2jk}{\epsilon} \hat{r} \times \frac{\epsilon}{4\pi} \frac{e^{-jkr}}{r} \iiint_{V} (2E_{o}e^{(-j\beta-\alpha)y'} \hat{y}) e^{jk\hat{r}\cdot\vec{r}'} \delta(x' - (-\frac{w}{4})) dv'$$

$$\approx \frac{E_{ojk}}{\pi} \frac{e^{-jkr}}{r} \hat{r} \times \iiint_{V} e^{(-j\beta-\alpha)y'} e^{jk\hat{r}\cdot\vec{r}'} \delta(x' - (-\frac{w}{4})) \hat{y} dv'. \tag{4.5}$$

The factor of 2 is included because the magnetic surface current images into the PEC ground plane. Equation (4.5) becomes

$$\vec{E} \approx \frac{E_o j k}{\pi} \frac{e^{-jkr}}{r} \hat{r} \times \iiint_{V} e^{(-j\beta - \alpha)y'} e^{jk\hat{r} \cdot \vec{r}'} \delta(x' - (-\frac{w}{4})) \hat{y} \, dv'$$
(4.6)

after employing a singular model since the magnetic current lies in the y-z plane within the radiating aperture located at $x=-\frac{w}{4}$. Once a spherical-to-rectangular transformation is performed on the \hat{r} unit vector, (4.6) becomes

$$\overrightarrow{E} \approx \frac{E_{o}jk}{\pi} \frac{e^{-jkr}}{r} \hat{r} \times \iiint_{V} \left(e^{(-j\beta - \alpha)y'} e^{jk(\hat{x}\sin\theta\cos\phi + \hat{y}\sin\theta\sin\phi + \hat{z}\cos\theta) \cdot \overrightarrow{r}'} \right) \\
\cdot \delta(x' + \frac{w}{4}) \hat{y} dv', \tag{4.7}$$

which reduces to

$$\overrightarrow{E} \approx \frac{E_{o}jk}{\pi} \frac{e^{-jkr}}{r} \hat{r} \times \iiint_{V} \left(e^{jy'(k\sin\theta\sin\phi - \beta + j\alpha)} e^{jk(x'\sin\theta\cos\phi + z'\cos\theta)} \right)$$

$$\cdot \delta(x' + \frac{w}{4})\hat{y}) dv'$$
(4.8)

since $\vec{r}' = x'\hat{x} + y'\hat{y} + z'\hat{z}$. Since the solution is independent of the order of integration, it is appropriate to evaluate the integral over x' first leading to

$$\overrightarrow{E} \approx \frac{E_{o}jk}{\pi} \frac{e^{-jkr}}{r} \hat{r} \times \hat{y}e^{-jk} \frac{w}{4} \sin\theta \cos\phi \int_{z'} \int_{y'} e^{jy'(k\sin\theta \sin\phi - \beta + j\alpha)} e^{jkz'\cos\theta} dy' dz'.$$
(4.9)

Since the substrate is electrically thin $(kh \ll 1)$, the integral over z' is

$$\int_{-\frac{h}{2}}^{\frac{h}{2}} e^{jkz'\cos\theta} dz' \approx h, \tag{4.10}$$

and (4.9) becomes

$$\overrightarrow{E} \approx \frac{E_{o}jk}{\pi} \frac{e^{-jkr}}{r} \hat{r} \times \hat{y}he^{-jk} \frac{w}{4} \sin\theta \cos\phi \int_{y'} e^{jy'(k\sin\theta \sin\phi - \beta + j\alpha)} dy'. \tag{4.11}$$

Rearranging terms leads to

$$\overrightarrow{E} \approx \frac{E_{o}jkh}{\pi} \frac{e^{-jk(r + \frac{w}{4}\sin\theta\cos\phi)}}{r} \hat{r} \times \hat{y} \int_{y'} e^{jy'(k\sin\theta\sin\phi - \beta + j\alpha)} dy'$$

$$\approx \frac{E_{o}jkh}{\pi} \frac{e^{-jk(r + \frac{w}{4}\sin\theta\cos\phi)}}{r} \hat{r} \times \hat{y} \int_{-L/2}^{L/2} e^{jy'(k\sin\theta\sin\phi - \beta + j\alpha)} dy'. (4.12)$$

The integral in (4.12) is of the form

$$\int_{-L/2}^{L/2} e^{j\zeta\rho} d\zeta = 2 \frac{\sin(\rho \frac{L}{2})}{\rho}$$
(4.13)

where $\rho = (k \sin \theta \sin \phi - \beta + j\alpha)$ and $\zeta = y'$. Therefore, (4.12) becomes

$$\vec{E} \approx \frac{E_{o}jkh}{\pi} \frac{e^{-jk(r + \frac{w}{4}\sin\theta\cos\phi)}}{r} \hat{r} \times \hat{y}2 \frac{\sin\left(\frac{L}{2}(k\sin\theta\sin\phi - \beta + j\alpha)\right)}{(k\sin\theta\sin\phi - \beta + j\alpha)}$$
(4.14)

which becomes

$$\overrightarrow{E} \approx \frac{E_{o}jkhL}{\pi} \frac{e^{-jk(r + \frac{w}{4}\sin\theta\cos\phi)}}{r} \operatorname{sinc}\left(\frac{L}{2}(k\sin\theta\sin\phi - \beta + j\alpha)\right) \left(\hat{\phi}\cos\theta\sin\phi - \hat{\theta}\cos\phi\right),\tag{4.15}$$

after completing rectangular-to-spherical transformation on unit vector \hat{y} and taking the cross product. In the elevation (YZ-plane), $\phi = \frac{\pi}{2}$ and $\frac{-\pi}{2} \le \theta \le \frac{\pi}{2}$ reducing (4.15) to

$$\overrightarrow{E} \approx \frac{E_o j k h L}{\pi} \frac{e^{-jkr}}{r} \cos \theta \operatorname{sinc} \left(\frac{L}{2} (k \sin \theta - \beta + j\alpha) \right) \hat{\phi}. \tag{4.16}$$

The normalized radiation intensity is determined to be

$$U(\theta, \phi = \frac{\pi}{2}) = \frac{|\overrightarrow{E}(\theta, \phi = \frac{\pi}{2})|^2}{|\overrightarrow{E}(\theta, \phi = \frac{\pi}{2})|^2_{max}} = \frac{\sqrt{\overrightarrow{E}(\theta, \phi = \frac{\pi}{2}) \cdot \overrightarrow{E}^*(\theta, \phi = \frac{\pi}{2})}^2}{\left[\sqrt{\overrightarrow{E}(\theta, \phi = \frac{\pi}{2}) \cdot \overrightarrow{E}^*(\theta, \phi = \frac{\pi}{2})}^2\right]_{max}}$$
$$= \cos^2 \theta \left|\operatorname{sinc}\left(\frac{L}{2}(k\sin\theta - \beta + j\alpha)\right)\right|^2_{\theta = \theta, MainBeam}, \tag{4.17}$$

from equation (4.16). It is important to note that the far-field analytical solution derived with the RAM method is an approximation. Albeit a reasonably accurate approximation considering it uses the leakage and phase coefficients from yet another approximation technique: the TRM method. The TRM method assumes that the structure is infinite in extent. It is a reasonable assumption since the structure is axially invariant and agrees well with full-wave solutions such as the Finite-Difference Time-Domain method; see [15]. Figure 4.4 and Figure 4.5 depict the normalized far-field gain patterns of the unloaded and 0.10 pF loaded HMLWA antennas, respectively, computed using the RAM method. The figures are limited to the frequencies that lie in the operational leaky region of each antenna, i.e. 6 to 8 GHz for the unloaded antenna (see Figure 3.5) and 4 to 5 GHz for the 0.10 pF loaded antenna (see Figure 3.8). Tabulated main beam angles for the unloaded and 0.10 pF loaded HMLWA antennas are given in Table 4.1 and Table 4.2, respectively.

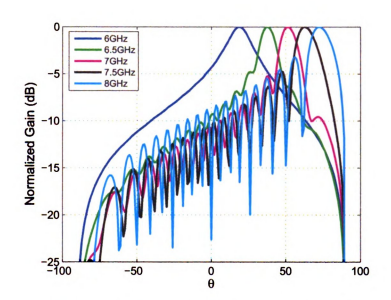


Figure 4.4. Analytical solution to far fields maintained by equivalent magnetic current on the surface of the radiating aperture of the unloaded HMLWA antenna.

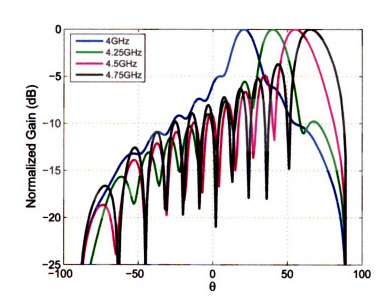


Figure 4.5. Analytical solution to far fields maintained by equivalent magnetic current on the surface of the radiating aperture with $0.10~\rm pF$ edge loading configuration.

Tah usin

> Tal ana

Table 4.1. Main beam direction of unloaded HMLWA antenna determined analytically using RAM method

Frequency (GHz)	Main Beam		
6.00	19°		
6.25	29°		
6.50	38°		
6.75	45°		
7.00	51°		
7.25	57°		
7.50	63°		
7.75	67°		

Table 4.2. Main beam direction of 0.10 pF edge-loaded HMLWA antenna determined analytically using RAM method_____

Frequency (GHz)	z) Main Beam		
4.00	21°		
4.25	40°		
4.50	55°		
4.75	65°		
5.00	74°		
	i .		

CHAPTER 5

ANTENNA DESIGN

The unloaded and reactively loaded HMLWA antennas are depicted in Figure 5.1 and Figure 5.2, respectively. The antennas are printed on Rogers RT/duroid 5870 high frequency laminate characterized by a relative permittivity of ϵ_r =2.33, standard thickness of 31 mils, and a dissipation factor of tan δ =0.0012. The antennas consist of a conducting strip 340 mm long by 7.6 mm wide (7λ and 0.15λ , respectively at 6 GHz) sitting atop the grounded dielectric substrate. The antennas are terminated in Pasternack's SubMiniature version A (SMA) 50 Ω terminations, product identification number PE6081. The bifurcating wall is constructed of 440 vias spaced every $\frac{\lambda}{100}$, or 0.381 mm. The vias have a radius of 0.1905 mm. The unloaded HMLWA antenna is fed via an SMA coaxial connector with the outer conductor connected to the ground plane and the inner conductor terminated on the conducting strip (passing through the substrate). The reactively loaded HMLWA antenna is edge-launch fed via a matched 50 Ω microstrip line. The microstrip line is 2.2860 mm wide, and is designed in Microwave Office $^{\textcircled{R}}$ 2007 to ensure that it is matched at 50 Ω . Twenty American Technical Ceramics 600S series multilayer capacitors (EIA case size 0603) are placed in shunt with the radiating edge by mounting one terminal on the conducting strip and the other terminal, 0.6 mm away, on copper pads (3.7860 mm \times 2.6430 mm) with a center-to-center spacing of 16.1905 mm. The pads are connected to the ground plane by vias. Each pad consists of four vias to ensure contact with the ground plane. Figure 5.3 shows an exploded view of the mounting pad and the associated dimensions.



Figure 5.1. Unloaded 340 mm HMLWA antenna with through-substrate feed



Figure 5.2. Loaded 340 mm HMLWA antenna with edge-launch feed



Figure 5.3. Exploded view of loaded HMLWA antenna showing $0.10~\mathrm{pF}$ $0603~\mathrm{multi-layer}$ capacitors

5.1 Measurements

The Sensors Directorate (RY) of the Air Force Research Laboratory at Wright-Patterson Air Force Base provided materials and facilities for the fabrication and measurement of the reactively loaded HMLWA antenna. Sections 5.1.1 through 5.2.1 provide measured data and detailed descriptions of the laboratory apparatus (and associated settings) used during the data collection.

5.1.1 Return Loss

The return loss measurement of the antennas is motivated by the bandwidth definition given in [3] and [4]. Here, the authors define the bandwidth as a percentage over the -10 dB resonating band.

5.1.2 Unloaded HMLWA

As an example, Figure 5.4 shows the return loss, or $|S_{11}|$, of the unloaded HMLWA antenna. S_{11} is defined as the reflection coefficient seen at port 1 when port 2 is terminated in a matched load [27]. The bandwidth, expressed as a percentage around the center frequency, is governed by

$$BW = \frac{f_U - f_L}{f_L + \left(\frac{f_U - f_L}{2}\right)} \times 100,$$
 (5.1)

where f_U and f_L are the frequencies of the upper and lower -10 dB crossing points. Therefore, the bandwidth of the unloaded HMLWA is 23.19% for an f_U =8.2314 GHz and an f_L =6.5206 GHz.

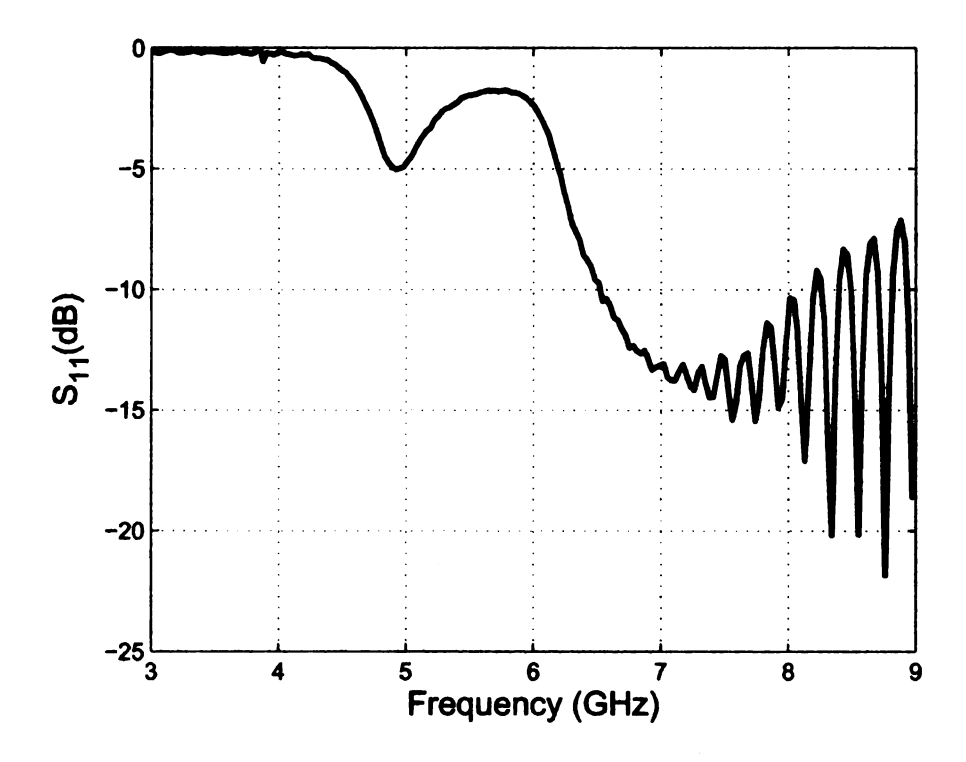


Figure 5.4. Return loss of an unloaded terminated HMLWA antenna

The return loss data is measured using an HP8510C Vector Network Analyzer (VNA) powered on an hour prior to data collection, ensuring accurate measurements. The HP8510C VNA is used in conjunction with the HP83631A 8360 Series Synthe-

GORE PHASEFLEX test assemblies (cables) with an SMA pin connector connects the VNA to the antenna under test (AUT). 192 inches of cable is used to ensure the AUT can be placed in the compact antenna chamber, as to avoid unintentional scattering/reflection from nearby objects in the laboratory. To ensure accurate results, prior to connecting the VNA to the AUT, the HP8510C VNA must be calibrated for S₁₁ one-port measurements. The pre-calibration process commences by setting the VNA to the factory preset state, and setting the start and stop frequencies to 3 and 9 GHz, respectively. Next, the sweep time is changed from the factory preset state of 160 to 100 ms/Sweep. The scale (located on the FUNCTION block of the VNA) is changed to 10 dB/division with a reference value of 0 dB, and a reference line position set at 5 divisions. Calibration begins by placing an open termination at the opposite end of the 96 inch long GORE PHASEFLEX test assembly followed by a short and a broadband load. Figure 5.5 compares the return loss of both the terminated and non-terminated unloaded HMLWA antennas.

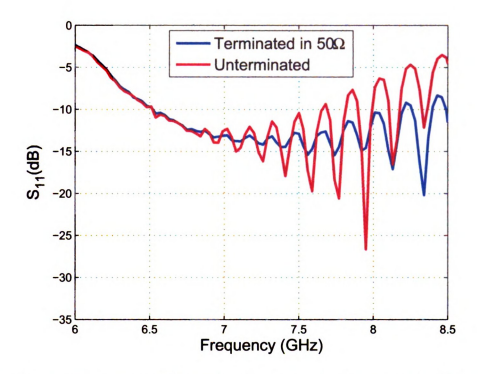
Note that the 50 Ω load at the end of the antenna absorbs a significant amount of the higher frequency reflections. Inclusion of the 50 Ω load also increases the bandwidth from 16.03% to 23.19%. Figure 5.6 shows the PHASEFLEX test assembly and the Pasternack 50 Ω termination. Since the voltage standing wave ratio (VSWR) is defined as

$$VSWR = \frac{1+|\Gamma|}{1-|\Gamma|},\tag{5.2}$$

the VSWR of both the terminated and non-terminated HMLWA antennas is easily computed and shown in Figure 5.7.

5.1.3 Reactively Loaded HMLWA

Since the HMLWA antenna is not symmetric about the XZ plane (i.e. $y = \frac{L}{2}$), both $|S_{11}|$ and $|S_{22}|$ return loss data are measured. All settings on the HP8510C VNA



 ${f Figure}$ 5.5. Return loss of terminated and non-terminated unloaded HMLWA antennas.



Figure 5.6. (a) PHASEFLEX test assembly. (b) Pasternack 50 Ω termination

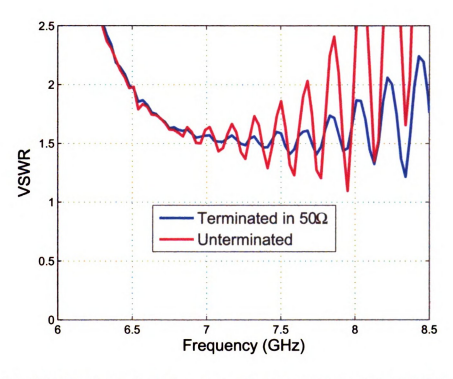


Figure 5.7. VSWR of terminated and non-terminated unloaded HMLWA antennas.

remain unchanged from the $|S_{11}|$ measurement of the unloaded HMLWA antenna, calibration excepted. $|S_{11}|$ is the reflection coefficient seen at port 1, the port on the left hand side of the picture in Figure 5.2. Figure 5.8 shows the magnitude of S_{11} for both the reactively loaded simulated and measured HMLWA antennas. The $|S_{11}|$ results show the bandwidth of the simulated antenna exceeds that of the measured antenna by 25%. The variation could be due to the microstrip feed line or an improper choice of the termination. Another potential culprit could be the modeling of the capacitors. The capacitors are modeled as lossless ideal lumped elements. The capacitor data sheet does not contain equivalent series resistance (ESR) data in the C-band. It does depict an inversely proportional relationship between capacitance and ESR. Therefore, the inferred ESR in the C-band is 0.10Ω . Altering the HMLWA antenna simulations to include lossy capacitors is discussed in Section 6.1.

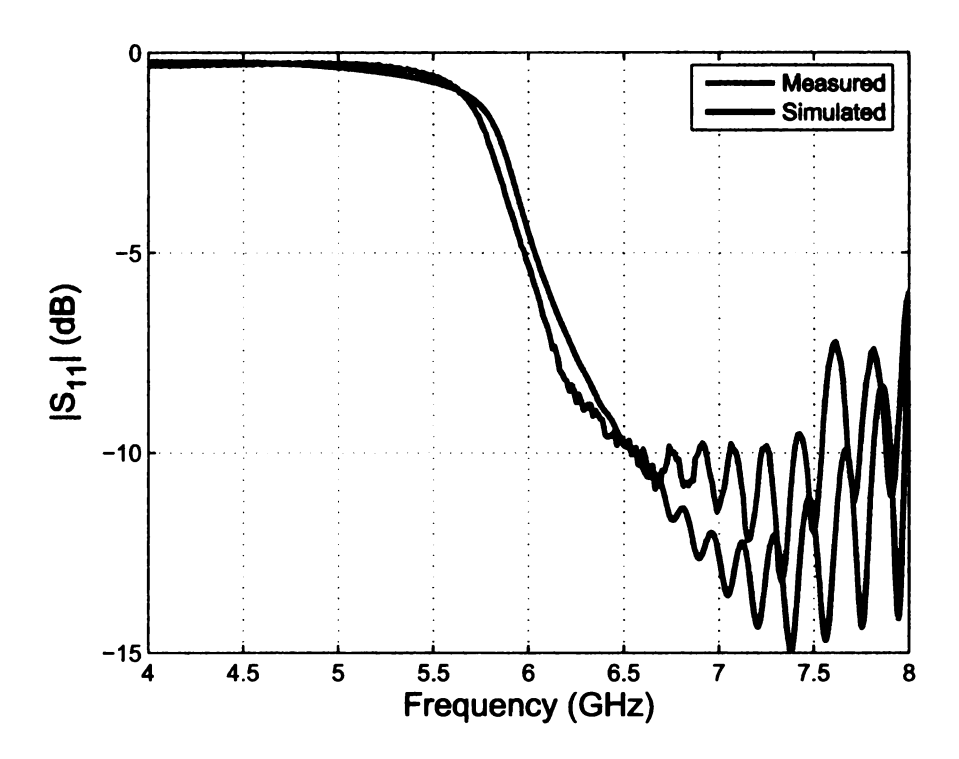


Figure 5.8. Simulated vs. Measured $|S_{11}|$ Return Loss of Reactively Loaded HMLWA Antenna.

Þ

When port 1 is terminated in a 50 Ω load and port 2 is excited, $|S_{22}|$ return loss data is measured. Figure 5.9 reveals simulated results that more accurately predict the measurements. Here, the bandwidth of the simulated HMLWA antenna is 24.75% while that of the measured antenna is 22.18%, an 11.6% difference.

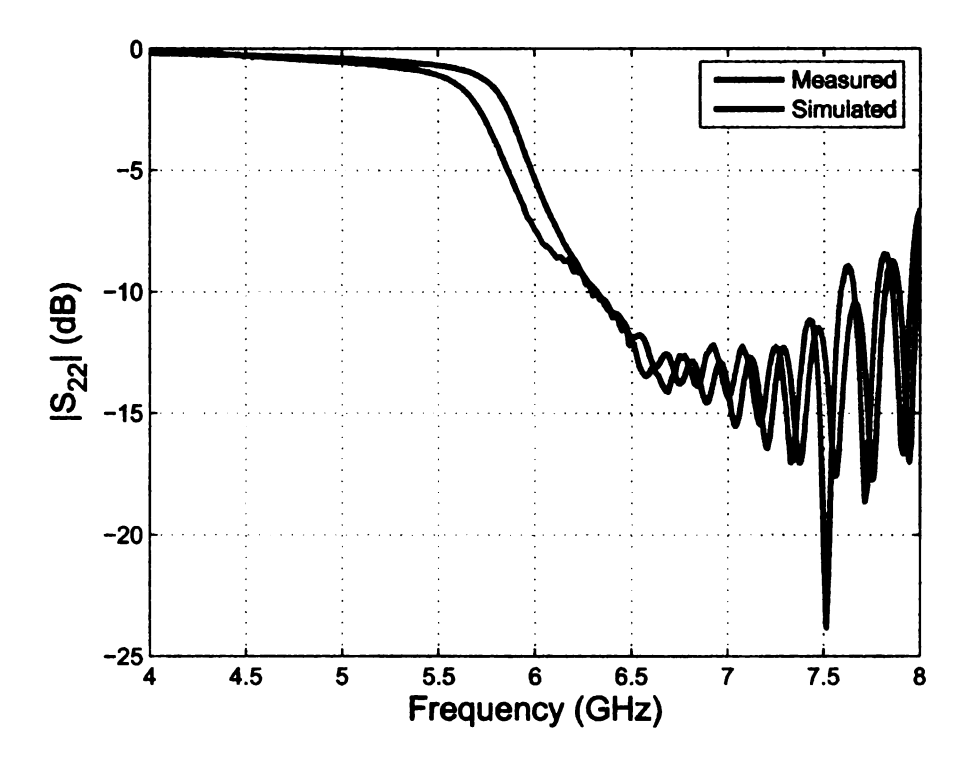


Figure 5.9. Simulated vs. Measured $|S_{22}|$ Return Loss of Reactively Loaded HMLWA Antenna.

5.1.4 Antenna Measurement Calibration

The reactively loaded HMLWA antenna is measured in the Nearfield Systems Incorporated (NSI) spherical near-field measurement system. The near-field measurement system is capable of measuring planar, cylindrical, and spherical near-field antenna patterns. The system consists of a Windows based workstation, Agilent E8362B PNA Network Analyzer, and an anechoic chamber complete with mobile scanner and sled.

The workstation and PNA are shown in Figure 5.10 while Figure 5.11 shows the scanner and sled.

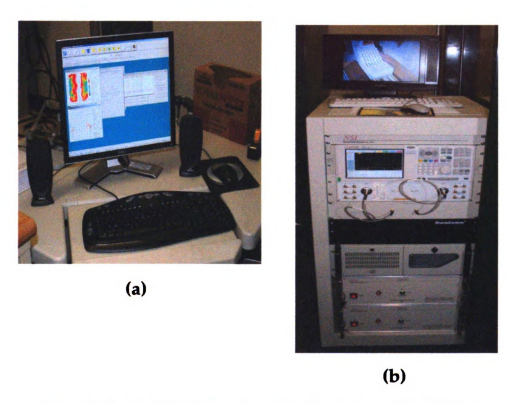


Figure 5.10. (a) NSI-2000 workstation (b) Agilent E8362B PNA

The NSI system is controlled by the NSI2000 Professional edition software, version 4.0527. Before the antenna is characterized, the system must be calibrated to ensure accurate measurements. The reactively loaded HMLWA antenna is measured over the C-band of the EM spectrum. Calibration must be done in two steps since the antenna is measured over the C-band (4-8 GHz), which requires calibration with two standard gain horns (SGH).

The C-band is discretized into two portions: the lower portion, 3.95-5.85 GHz, and the upper portion, 5.85-8.2 GHz. These portions require the use of two sets of SGHs



Figure 5.11. Reactively loaded HMLWA antenna in Near Field Anechoic Chamber

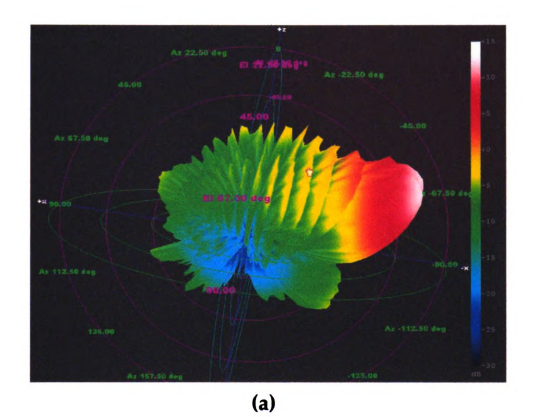
and open-ended waveguides (OEWG). The WR187 SGH-OEWG pair is appropriate for the lower portion, while the WR137 pair is appropriate for the upper portion. Data collection from the lower portion of the band commences with calibration requiring the WR187 SGH and the WR187 open-ended waveguide (OEWG). Once a full spherical scan is taken (a measurement time of approximately 1 hour), the data is stored as a reference for the AUT scan. After removing the WR187 SGH, the AUT is characterized, and the results stored. The process is repeated for the upper portion.

5.2 Reactively Loaded HMLWA Antenna Pattern Measurements

After the data is collected, the far-field is extrapolated from the near-field and the NSI2000 software allows the user to view or export the data. The data is displayed in a variety of ways; the 3-dimensional far-field pattern and 2-dimensional contour figures reveal a significant amount of information. Figure 5.12 shows snapshots of the 3-dimensional far-field pattern and the 2-dimensional far-field contour plot at 7 GHz. Although the 3-dimensional far-field pattern is aesthetically pleasing it does not display all the details (i.e., directivity, beamwidth, etc.) that the 2-dimensional contour plot displays. Figure 5.12b reveals the main beam direction (approximately 70°) and insight into the more intimate details of the pattern. Here, it is clear that the main beam has a concave shape covering nearly ±35° in the horizontal plane. (Note: The coordinate system used by NSI is shifted by 90°. Therefore, the terms elevation and azimuth are opposite that of the standard convention, i.e., elevation corresponds to the horizontal plane, while azimuth refers to the normal elevation plane.)

Since the goal of this thesis is to show fixed frequency beam steering of the main beam direction, a 2-dimensional elevation cut in the YZ plane is used to determine beam direction. Figure 5.13 depicts gain as a function of elevation angle, θ . Here, θ represents the main beam direction measured off broadside. The figure also shows good agreement with simulation. There is a significant amount of disagreement near -60°, but the measurements outperform the simulations with a front-to-back ratio (FBR) of 13.45 dB as opposed to the simulated FBR of 10.09 dB. Measured patterns covering the C-band of the EM spectrum, every 250 MHz, are given in Appendix E. Analysis of Figure E.1 through Figure E.17 show that when the hybrid leaky-wave EH₁ mode begins to propagate, near 5.75 GHz, the main beam begins near broadside and scans toward near end fire as frequency increases.

The main beam direction vs. frequency for the unloaded, simulated reactively loaded, and measured reactively loaded HMLWA antennas is shown in Figure 5.14. Here, the green curve represents the simulated unloaded data, while the blue and red curves represent the simulated and measured reactively loaded HMLWA antennas. There is a 15.3% average shift in the main beam direction of the unloaded and reactively loaded simulated antennas across the operational leaky-wave region. The unloaded and reactively loaded simulations show that the minimum expected shift in



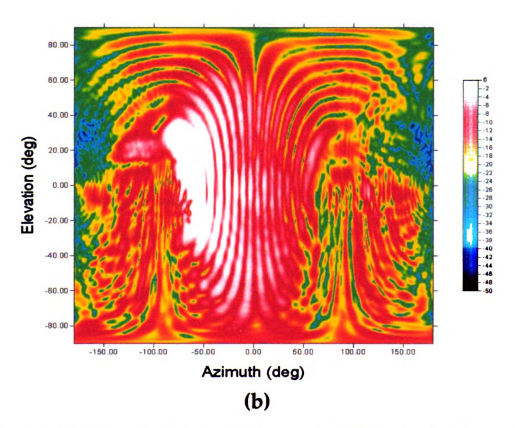


Figure 5.12. (a) 3-dimensional Spherical Pattern and (b) 2-dimensional Contour Plot at $\,$ 7.00 GHz

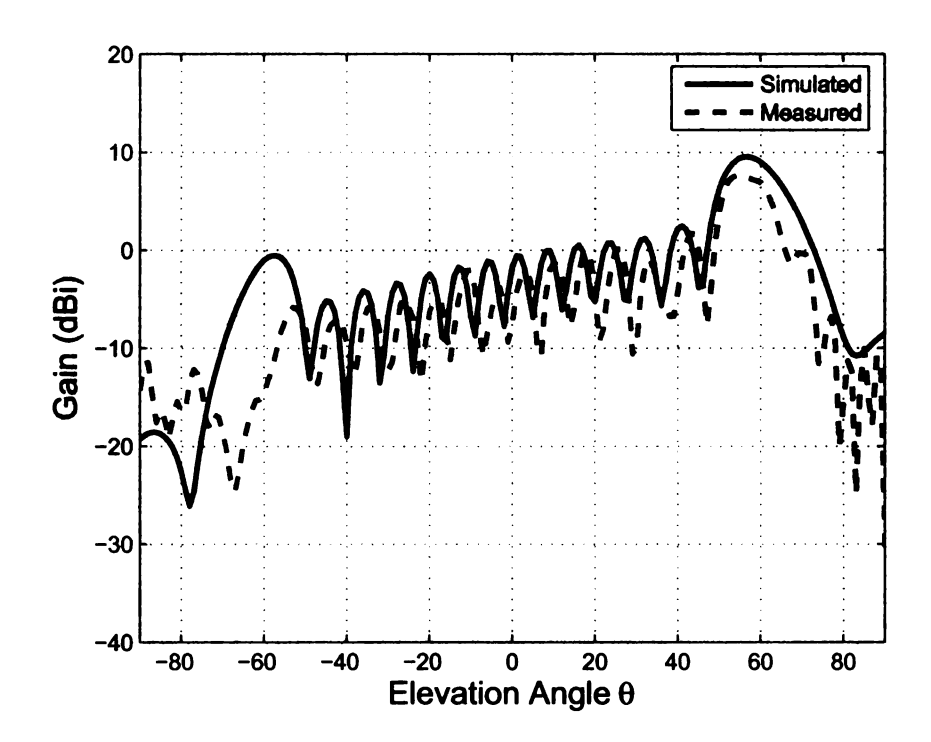


Figure 5.13. Simulated vs Measured HMLWA Gain at 7.00 GHz

the main beam direction is 14° and occurs at 6.50, 7.50, and 7.75 GHz. The maximum expected shift occurs at 6.25 GHz, where the main beam is shifted by 18°.

There is 100% agreement (0% error) between the measured and simulated reactively loaded HMLWA antenna data between 7.25-7.75 GHz. Unfortuantly, the simulations do not accurately predict the measurements over the entire operational region. The percent error between the simulated and measured results is governed by the following expression:

$$PercentError = \frac{|Simulated - Measured|}{Measured} \times 100\%.$$
 (5.3)

The maximum percent error between simulation and measurement is 16.2%, which occurs at 6.25 GHz. Here, the main beam direction (31°) is 6° off from the actual

observed (measured) direction of 37°.

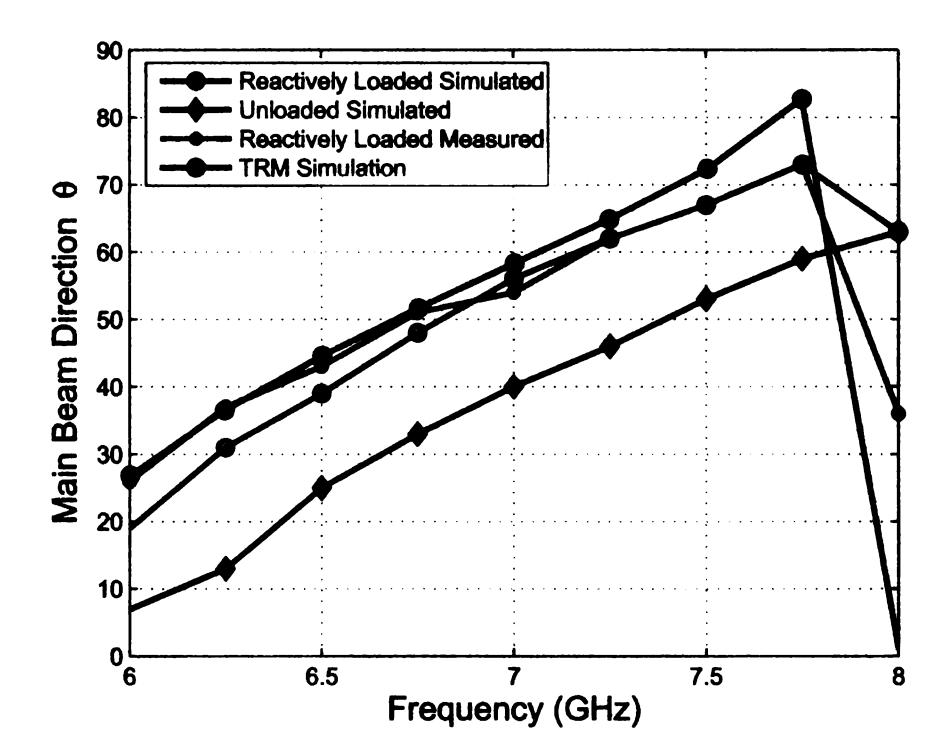


Figure 5.14. Unloaded, Simulated Reactively Loaded, and Measured Reactively Loaded HMLWA Antenna Main Beam Direction Comparison

5.2.1 Radiation Effeciency

Radiation efficiency, according to [28], is the ratio of the total power radiated by the antenna to the total power accepted by the antenna at its input terminals during radiation. It is frequently expressed as

$$Radiation Efficiency = \frac{Gain}{Directivity}.$$
 (5.4)

Figure 5.15 shows broadband simulated and measured radiation efficiencies. The significant variation between the simulated and measured results is mostly attributed to

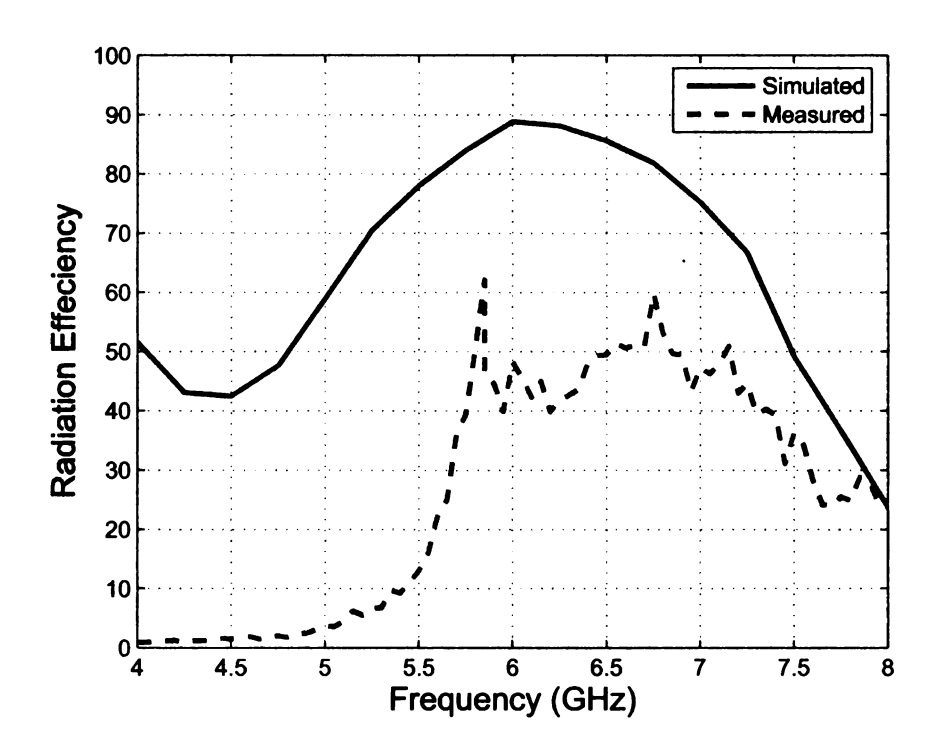


Figure 5.15. Simulated vs Measured Radiation Efficiency

the lossless capacitors used in the model. The simulated results are questionable reporting 50% effeciency before the hybrid leaky-wave EH₁ mode propagates. (Leakage begins near 5.75 GHz, see Figure 5.8 and Figure E.8.) Further, the simulated curve shows a peak effeciency of 90% at 6.00 GHz, while the measured result is slightly less than half (48%) at this frequency.

The measured radiation efficiency data is consistent with the predictions. As the EH₁ mode begins to propagate (near 5.75 GHz), the efficiency reaches its maximum at 62%, and slowly decreases reaching a minimum of 24% at 8.00 GHz. Something peculiar occurs between 5.90-6.50 GHz where the effeciency drops below 50%, in the middle of the operational range. This behavior is unexplained now, but will be investigated in the future.

CHAPTER 6

CONCLUSIONS

In this thesis, several properties of half-width microstrip leaky-wave antennas are investigated. A brief history of leaky-wave antennas is discussed in Chapter 2. In this chapter, the half-width approximation of the full-width microstrip leaky-wave antenna results reported by AFRL researchers are verified. It is found that the half-width microstrip leaky-wave antenna accurately approximates its full-width counterpart when the antennas are simulated on a practical, finite ground plane-substrate layer. However, the approximation does not hold when the antennas are simulated on an infinite ground plane-substrate layer.

In Chapter 3, a preliminary technique is used prior to invoking a full-wave solution to save time and resources. This technique, the transverse resonance method, is used to extract the axial complex propagation coefficient from the transverse complex propagation coefficient. The results of the method are given in Section 3.8, which show the main beam direction can be fixed near end fire (at 80°) over the entire C-band, provided that a per unit length edge loading configuration is used.

An analytical solution to the far-zone fields radiated by the HMLWA antenna is described in Chapter 4. The solution makes use of the radiating aperture method, and assumes a well matched load. Therefore, the solution does not account for reflections.

The antenna design, fabrication materials, and measurements are described in Chapter 5. Here, measured data from the operational region of the HMLWA antenna shows the average shift in the main beam direction (with respect to the simulated unloaded HMLWA antenna) is nearly 17%. The largest shift in the main beam direction is 24° at 6.25 GHz, while the smallest shift, 14°, occurs at three frequencies, 7.00, 7.50, and 7.75 GHz. Comparisons between measurement and simulation show

100% agreeement over a 500 MHz band (7.25 - 7.75 GHz).

The measured results show that the main beam direction of the reactively loaded HMLWA antenna is indeed controlled at various fixed frequencies. This is mentioned as the goal of the work in Chapter 1, and the results show that it was accomplished (see Chapter 5).

6.1 Future Work

There is an interest in having the main beam direction fixed over the entire operational leaky band. Since the main beam direction is dependent on frequency, fixing the main beam direction over a broad frequency band would require varying the impedance (by changing the edge loading capacitance) at the radiating edge of the HMLWA antenna. Based on the results of the TRM method, which requires a per unit length edge loading, this could be accomplished by placing a reactive sheet at the radiating edge of the HMLWA antenna.

Another alternative to loading the radiating edge with a reactive sheet is to maintain the lumped capacitor edge loading technique used in this thesis. In the proposed design, the capacitance value of each lumped element would vary, and would no longer be constant. After having a discussion with my friend and colleague, Mr. Raoul Ouedraogo, he pointed out that the optimal capacitance values could be determined through the use of a genetic algorithm. This would require a well written fitness function. Once the optimal capacitance values are determined, a full-wave solution will be computed using CST Microwave Studio. The antenna could be fabricated and characterized contingent upon the results of that simulation. Mr. Ouedraogo and I will investigate this optimization technique and we will report our findings in a subsequent publication.

APPENDICES

APPENDIX A

CONSTRUCTION OF SOLUTIONS FROM POTENTIALS

In this appendix, construction of solutions from potentials is presented. This discussion will parallel that presented in [22] and [29]. Assuming an $e^{j\omega t}$ time dependence, Maxwell's equations maintained by electric and magnetic sources in an isotropic, homogeneous region of space characterized by permittivity ϵ and permeability μ are given by:

$$\nabla \times \overrightarrow{E} = -j\omega \mu \overrightarrow{H} - \overrightarrow{M} \tag{A.1a}$$

$$\nabla \times \overrightarrow{H} = j\omega \epsilon \overrightarrow{E} + \overrightarrow{J} \tag{A.1b}$$

$$\nabla \cdot \overrightarrow{D} = \rho \tag{A.1c}$$

$$\nabla \cdot \overrightarrow{B} = \rho_m. \tag{A.1d}$$

In source-free regions, Maxwell's curl equations reduce to:

$$\nabla \times \overrightarrow{E} = -j\omega \mu \overrightarrow{H} \tag{A.2a}$$

$$\nabla \times \overrightarrow{H} = j\omega \epsilon \overrightarrow{E}. \tag{A.2b}$$

Equations (A.2a) and (A.2b) are Faraday's and Ampere's laws, respectively. In order to fully express a vector field, both its curl and divergence must be specified; therefore, it is necessary to define the divergence of \overrightarrow{H} and \overrightarrow{E} . Using the constitutive parameter relating the magnetic flux density, \overrightarrow{B} , to the magnetic field intensity, \overrightarrow{H} , i.e., $\overrightarrow{B} = \mu \overrightarrow{H}$, Faraday's law becomes

$$\nabla \times \overrightarrow{E} = -j\omega \overrightarrow{B}. \tag{A.3}$$

Taking the divergence of equation (A.3) and utilizing the following vector derivative identity

$$\nabla \cdot (a\overrightarrow{B}) = a\nabla \cdot \overrightarrow{B} + \overrightarrow{B} \cdot \nabla a \tag{A.4}$$

yields,

$$\nabla \cdot (\nabla \times \overrightarrow{E}) = \nabla \cdot (-j\omega \overrightarrow{B})$$

$$= -j\omega \nabla \cdot \overrightarrow{B} + \overrightarrow{B} \cdot \nabla (-j\omega)$$

$$= -j\omega \nabla \cdot \overrightarrow{B}$$
(A.5)

where $\nabla(-j\omega) = 0$ because the product of $-j\omega$ is a spatially independent constant whose gradient vanishes. Equation (A.5) is further simplified by realizing that the divergence of the curl of any vector field vanishes, i.e.,

$$\nabla \cdot (\nabla \times \overrightarrow{B}) = 0; \tag{A.6}$$

therefore, equation (A.5) becomes

$$\nabla \cdot \overrightarrow{B} = 0, \tag{A.7}$$

which is Gauss' law for the nonexistence of magnetic monopoles. Gauss' electric law is derived in a similar fashion. Using the constitutive parameter relating the electric flux density, \overrightarrow{D} , to the electric field intensity, \overrightarrow{E} , i.e., $\overrightarrow{D} = \epsilon \overrightarrow{E}$, and substituting the latter into Ampere's law, equation (A.2b), and post application of vector derivative identities (A.4) and (A.6), yields Gauss' electric law,

$$\nabla \cdot \overrightarrow{D} = 0. \tag{A.8}$$

By virtue of vector derivative identity (A.6), any vector whose divergence vanishes must be the curl of some other vector. Hence \overrightarrow{B} of equation (A.7) is the curl of some other vector, say \overrightarrow{A} ,

$$\nabla \times \overrightarrow{A} = \overrightarrow{B}$$

$$= \mu \overrightarrow{H}. \tag{A.9}$$

Since this equation shows that \overrightarrow{H} is the field due to vector field \overrightarrow{A} , it is re-expressed as

$$\mu \overrightarrow{H}_A = \nabla \times \overrightarrow{A}; \tag{A.10}$$

where the the subscript A on \overrightarrow{H} reflects the explicit dependence of \overrightarrow{H} on \overrightarrow{A} . Vector field \overrightarrow{A} is known as the magnetic vector potential. It is a mathematical tool which simplifies the construction of EM solutions [22]. Substituting this result into Faraday's law, equation (A.3), leads to

$$\nabla \times \overrightarrow{E}_A = -j\omega(\nabla \times \overrightarrow{A}). \tag{A.11}$$

Rearranging terms leads to

$$\nabla \times (\overrightarrow{E}_A + j\omega \overrightarrow{A}) = 0, \tag{A.12}$$

where the following vector identity was used since both \overrightarrow{E} and \overrightarrow{A} have continuous first and second partial derivatives

$$\nabla \times (\overrightarrow{A} + \overrightarrow{B}) = \nabla \times \overrightarrow{A} + \nabla \times \overrightarrow{B}. \tag{A.13}$$

Just as a divergenceless vector is the curl of some other vector, similarly, a curl-free vector is the gradient of some scalar, defined through the following vector derivative

identity

$$\nabla \times (\nabla a) = 0. \tag{A.14}$$

Thus, the quantity within the parenthesis in equation (A.12) can be represented as the gradient of some scalar; i.e.,

$$\overrightarrow{E}_A + j\omega \overrightarrow{A} = -\nabla \Phi_e, \tag{A.15}$$

where Φ_e is known as the electric scalar potential. Rearranging terms leads to an expression for \overrightarrow{E}_A as a function of the magnetic vector and electric scalar potentials,

$$\overrightarrow{E}_A = -(j\omega \overrightarrow{A} + \nabla \Phi_e). \tag{A.16}$$

Taking the curl of equation (A.10) and utilizing the vector derivative identity

$$\nabla \times (a\overrightarrow{B}) = a\nabla \times \overrightarrow{B} - \overrightarrow{B} \times \nabla a \tag{A.17}$$

yields

$$\nabla \times (\nabla \times \overrightarrow{A}) = \nabla \times (\mu \overrightarrow{H}_A)$$

$$= \mu \nabla \times \overrightarrow{H}_A - \overrightarrow{H}_A \times \nabla(\mu)$$

$$= \mu \nabla \times \overrightarrow{H}_A, \qquad (A.18)$$

because the gradient of a scalar vanishes. Rearranging terms leads to an expression for $\nabla \times \overrightarrow{H}_A$ as a function of the magnetic vector potential,

$$\nabla \times \overrightarrow{H}_A = \frac{1}{\mu} \nabla \times \nabla \times \overrightarrow{A}. \tag{A.19}$$

Substituting equations (A.16) and (A.19) into Ampere's law maintained by electric

current density \overrightarrow{J} , equation (A.1b), results in

$$\frac{1}{\mu}\nabla \times \nabla \times \overrightarrow{A} = j\omega\epsilon(-j\omega\overrightarrow{A} - \nabla\Phi_e) + \overrightarrow{J}$$

$$= -j^2\omega^2\epsilon\overrightarrow{A} - j\omega\epsilon\nabla\Phi_e + \overrightarrow{J}, \tag{A.20}$$

and distributing the μ throughout yields

$$\nabla \times \nabla \times \overrightarrow{A} = -j^2 \omega^2 \mu \epsilon \overrightarrow{A} - j \omega \mu \epsilon \nabla \Phi_e + \mu \overrightarrow{J}$$

$$= \omega^2 \mu \epsilon \overrightarrow{A} - j \omega \mu \epsilon \nabla \Phi_e + \mu \overrightarrow{J}$$

$$= k^2 \overrightarrow{A} - j \omega \mu \epsilon \nabla \Phi_e + \mu \overrightarrow{J}, \qquad (A.21)$$

where k is the wavenumber given by $k = \omega \sqrt{\mu \epsilon}$. Equation (A.21) becomes

$$\nabla(\nabla \cdot \overrightarrow{A}) - \nabla^2 \overrightarrow{A} = k^2 \overrightarrow{A} - j\omega\mu\epsilon\nabla\Phi_e + \mu \overrightarrow{J} \tag{A.22}$$

post application of the vector identity

$$\nabla \times \nabla \times \overrightarrow{A} = \nabla(\nabla \cdot \overrightarrow{A}) - \nabla^2 \overrightarrow{A}, \tag{A.23}$$

where ∇^2 represents the vector Laplacian. The curl of the magnetic vector potential is given in equation (A.9), but the divergence of this quantity, necessary to uniquely specify \overrightarrow{A} , has yet to be defined. The divergence of \overrightarrow{A} is judiciously chosen to simplify equation (A.22) as

$$\nabla \cdot \overrightarrow{A} = -j\omega\mu\epsilon\Phi_e,\tag{A.24}$$

which is also known as the Lorentz condition. Substituting the Lorentz condition into

equation (A.22), and applying the vector derivative identity

$$\nabla(ab) = a\nabla b + b\nabla a \tag{A.25}$$

yields,

$$-j\omega\mu\epsilon\nabla(\Phi_e) + \Phi_e\nabla(-j\omega\mu\epsilon) - \nabla^2\overrightarrow{A} = k^2\overrightarrow{A} - j\omega\mu\epsilon\nabla\Phi_e + \mu\overrightarrow{J},$$
or
$$\Phi_e\nabla(-j\omega\mu\epsilon) - \nabla^2\overrightarrow{A} = k^2\overrightarrow{A} + \mu\overrightarrow{J},$$
(A.26)

which reduces to

$$\nabla^2 \overrightarrow{A} + k^2 \overrightarrow{A} = -\mu \overrightarrow{J}, \tag{A.27}$$

the inhomogeneous complex magnetic vector potential wave equation.. The electric field due to the magnetic vector potential, \overrightarrow{E}_A , is given by

$$\overrightarrow{E}_{A} = -j\omega \overrightarrow{A} - \frac{1}{j\omega\mu\epsilon} \nabla(\nabla \cdot \overrightarrow{A}) \tag{A.28}$$

upon taking the gradient of the Lorentz gauge (equation (A.24)), and substituting the result into equation (A.16).

In a similar fashion, the magnetic field intensity, \overrightarrow{H} , can be written in terms of an electric vector potential, \overrightarrow{F} . From Gauss' electric law, equation (A.8), and vector derivative identity (A.6), \overrightarrow{D} must be the curl of some other vector, say a vector field \overrightarrow{F} , where

$$-\nabla \times \overrightarrow{F} = \overrightarrow{D}. \tag{A.29}$$

Therefore,

$$\epsilon \overrightarrow{E}_F = -\nabla \times \overrightarrow{F} \tag{A.30}$$

upon invoking the constitutive relationship $\overrightarrow{D} = \epsilon \overrightarrow{E}$. The magnetic field due to the electric vector potential, \overrightarrow{H}_F , results upon substituting equation (A.30) into Ampere's law, equation (A.2b), and invoking vector derivative identity (A.14), and is given by

$$\overrightarrow{H}_F = -(j\omega \overrightarrow{F} + \nabla \Phi_m), \tag{A.31}$$

where Φ_m is known as the magnetic scalar potential. Taking the curl of equation (A.30) and equating it to Faraday's law maintained by magnetic current density \overrightarrow{M} , equation (A.1a), leads to

$$\frac{-1}{\epsilon} \nabla \times \nabla \times \overrightarrow{F} = -j\omega \mu \overrightarrow{H}_F - \overrightarrow{M}, \tag{A.32}$$

which becomes

$$\frac{-1}{\epsilon} \nabla \times \nabla \times \overrightarrow{F} = -j\omega \mu (-j\omega \overrightarrow{F} - \nabla \Phi_m) - \overrightarrow{M}, \tag{A.33}$$

upon substituting \overrightarrow{H}_F from equation (A.31). Applying vector derivative identity (A.23) and defining the divergence of \overrightarrow{F} as

$$\nabla \cdot \overrightarrow{F} = -j\omega\mu\epsilon\Phi_m,\tag{A.34}$$

leads to

$$\nabla^2 \vec{F} + k^2 \vec{F} = -\epsilon \vec{M},\tag{A.35}$$

the inhomogeneous complex electric vector potential wave equation. The magnetic field due to the electric vector potential, \overrightarrow{H}_F , is given by

$$\overrightarrow{H}_F = -j\omega \overrightarrow{F} + \frac{1}{j\omega\mu\epsilon} \nabla(\nabla \cdot \overrightarrow{F})$$
 (A.36)

upon taking the gradient of equation (A.34), and substituting the result into equation (A.31).

The total EM fields are obtained by the superposition of the individual fields due to \overrightarrow{A} and \overrightarrow{F} [22], i.e.,

$$\overrightarrow{E} = \overrightarrow{E}_A + \overrightarrow{E}_F$$

$$= -j\omega \overrightarrow{A} + \frac{1}{j\omega\mu\epsilon} \nabla(\nabla \cdot \overrightarrow{A}) - \frac{1}{\epsilon} \nabla \times \overrightarrow{F}$$

$$= \frac{-j\omega}{k^2} (k^2 \overrightarrow{A} + \nabla(\nabla \cdot \overrightarrow{A})) - \frac{1}{\epsilon} \nabla \times \overrightarrow{F}$$
(A.37)

and

$$\overrightarrow{H} = \overrightarrow{H}_A + \overrightarrow{H}_F$$

$$= \frac{1}{\mu} \nabla \times \overrightarrow{A} - j\omega \overrightarrow{F} + \frac{1}{j\omega\mu\epsilon} \nabla(\nabla \cdot \overrightarrow{F})$$

$$= \frac{1}{\mu} \nabla \times \overrightarrow{A} - \frac{j\omega}{k^2} (k^2 \overrightarrow{F} + \nabla(\nabla \cdot \overrightarrow{F})). \tag{A.38}$$

These become

$$\vec{E} = \frac{-j\omega}{k^2} (\nabla \times \nabla \times \vec{A}) - \frac{1}{\epsilon} \nabla \times \vec{F}$$
 (A.39)

and

$$\overrightarrow{H} = \frac{1}{\mu} \nabla \times \overrightarrow{A} - \frac{j\omega}{k^2} (\nabla \times \nabla \times \overrightarrow{F})$$
 (A.40)

for all field points external to the source system. Solutions of equations (A.27) and (A.35) can be found using the method of separation of variables. For problems involving radiation, appropriate solutions of equations (A.27) and (A.35) are

$$\overrightarrow{A}(\overrightarrow{r}) = \mu \iiint_{V} \overrightarrow{J}(\overrightarrow{r}')G(\overrightarrow{r}|\overrightarrow{r}') dv'$$
(A.41)

and

$$\overrightarrow{F}(\overrightarrow{r}) = \epsilon \iiint_{V} \overrightarrow{M}(\overrightarrow{r}')G(\overrightarrow{r}|\overrightarrow{r}') dv', \qquad (A.42)$$

respectively. Here $G(\overrightarrow{r}|\overrightarrow{r}')$, the 3-dimensional free-space Green's function, is

$$G(\overrightarrow{r}|\overrightarrow{r}') = \frac{\psi(\overrightarrow{r}|\overrightarrow{r}')}{4\pi}$$

$$= \frac{e^{-jk|\overrightarrow{r}-\overrightarrow{r}'|}}{4\pi|\overrightarrow{r}-\overrightarrow{r}'|}.$$
(A.43)

Substituting equation (A.43) into equations (A.41) and (A.42) yields

$$\overrightarrow{A}(\overrightarrow{r}) = \frac{\mu}{4\pi} \iiint_{V} \overrightarrow{J}(\overrightarrow{r}') \frac{e^{-jk|\overrightarrow{r} - \overrightarrow{r}'|}}{|\overrightarrow{r} - \overrightarrow{r}'|} dv'$$
(A.44)

and

$$\vec{F}(\vec{r}) = \frac{\epsilon}{4\pi} \iiint_{V} \vec{M}(\vec{r}') \frac{e^{-jk|\vec{r} - \vec{r}'|}}{|\vec{r} - \vec{r}'|} dv', \tag{A.45}$$

respectively. Equations (A.44) and (A.45) are appropriate solutions to equations (A.27) and (A.35) because $\psi(\overrightarrow{r}|\overrightarrow{r}')$ satisfies the homogeneous scalar wave equation $\forall \overrightarrow{r} \neq \overrightarrow{r}'$.

The total fields are re-expressed as

$$\overrightarrow{E} = \frac{-j\omega}{k^2} \left(\nabla \times \nabla \times \frac{\mu}{4\pi} \iiint_V \overrightarrow{J}(\overrightarrow{r}') \frac{e^{-jk|\overrightarrow{r}-\overrightarrow{r}'|}}{|\overrightarrow{r}-\overrightarrow{r}'|} dv' \right)$$

$$- \frac{1}{\epsilon} \nabla \times \frac{\epsilon}{4\pi} \iiint_V \overrightarrow{M}(\overrightarrow{r}') G(\overrightarrow{r}|\overrightarrow{r}') dv'$$

and

$$\overrightarrow{H} = \frac{1}{\mu} \nabla \times \frac{\mu}{4\pi} \iiint_{V} \overrightarrow{J}(\overrightarrow{r}') \frac{e^{-jk|\overrightarrow{r} - \overrightarrow{r}'|}}{|\overrightarrow{r} - \overrightarrow{r}'|} dv'$$

$$- \frac{j\omega}{k^{2}} \left(\nabla \times \nabla \times \frac{\epsilon}{4\pi} \iiint_{V} \overrightarrow{M}(\overrightarrow{r}') \frac{e^{-jk|\overrightarrow{r} - \overrightarrow{r}'|}}{|\overrightarrow{r} - \overrightarrow{r}'|} dv' \right)$$

upon substituting (A.44) and (A.45) into equations (A.39) and (A.40), respectively. These equations reduce to

$$\vec{E} = \frac{-j\omega\mu}{4\pi k^2} \nabla \times \nabla \times \iiint_V \vec{J}(\vec{r}') \frac{e^{-jk|\vec{r} - \vec{r}'|}}{|\vec{r} - \vec{r}'|} dv'$$
(A.46)

and

$$\vec{H} = \frac{1}{4\pi} \nabla \times \iiint_{V} \vec{J}(\vec{r}') \frac{e^{-jk|\vec{r} - \vec{r}'|}}{|\vec{r} - \vec{r}'|} dv'$$
(A.47)

when the field is maintained only by \overrightarrow{J} , and

$$\overrightarrow{E} = \frac{-1}{4\pi} \nabla \times \iiint_{V} \overrightarrow{M}(\overrightarrow{r}') G(\overrightarrow{r}|\overrightarrow{r}') dv'$$
 (A.48)

and

$$\overrightarrow{H} = \frac{-j\omega\epsilon}{4\pi k^2} \nabla \times \nabla \times \iiint_V \overrightarrow{M}(\overrightarrow{r}') \frac{e^{-jk|\overrightarrow{r} - \overrightarrow{r}'|}}{|\overrightarrow{r} - \overrightarrow{r}'|} dv'$$
(A.49)

when maintained only by \overrightarrow{M} .

The Fraunhofer or far-field region is that region that lies beyond the radiating near-field (Fresnel) where the radiation pattern is unchanging with distance [30]. Equations (A.46) through (A.49) can be simplified by approximating the kernels of the integrals in the far zone provided that $r' \ll r$. The simplifications result in:

$$\overrightarrow{E} \approx \frac{-j\omega\mu}{4\pi} \frac{e^{-jkr}}{r} \left[\iiint_{V} \overrightarrow{J}(\overrightarrow{r}') e^{jk\hat{r}\cdot\overrightarrow{r}'} dv' \right]_{\perp \text{ to } \hat{r}}$$

$$\approx -j\omega \overrightarrow{A}_{T} \tag{A.50}$$

and

$$\overrightarrow{H} \approx \frac{-jk}{\mu} \hat{r} \times \frac{\mu}{4\pi} \frac{e^{-jkr}}{r} \iiint_{V} \overrightarrow{J}(\overrightarrow{r}') e^{jk\hat{r} \cdot \overrightarrow{r}'} dv'$$

$$\approx \frac{-jk}{\mu} \hat{r} \times \overrightarrow{A} \tag{A.51}$$

when the field is maintained only by \overrightarrow{J} , and

$$\vec{E} \approx \frac{jk}{\epsilon} \hat{r} \times \frac{\epsilon}{4\pi} \frac{e^{-jkr}}{r} \iiint_{V} \vec{M}(\vec{r}') e^{jk\hat{r} \cdot \vec{r}'} dv'$$

$$\approx \frac{jk}{\epsilon} \hat{r} \times \vec{F}$$
(A.52)

and

$$\overrightarrow{H} \approx \frac{-j\omega\epsilon}{4\pi} \frac{e^{-jkr}}{r} \left[\iiint_{V} \overrightarrow{M}(\overrightarrow{r}') e^{jk\hat{r}\cdot\overrightarrow{r}'} dv' \right]_{\perp \text{ to } \hat{r}}$$

$$\approx -j\omega \overrightarrow{F}_{T} \tag{A.53}$$

when maintained only by \overrightarrow{M} . \overrightarrow{A}_T and \overrightarrow{F}_T of equations (A.50) and (A.53) are the transverse components of the magnetic and electric vector potentials. They uphold the Sommerfeld radiation condition which states that fields far from sources must behave as waves TEM to the r-direction [31].

APPENDIX B

RADIATION PATTERNS OF FMLWA AND HMLWA ANTENNAS ON INFINITE AND FINITE GROUND PLANES

The following radiation patterns verifies the claim that the HMLWA antenna reasonably approximates the FMLWA antenna. The antennas are simulated on both infinite and finite ground planes using FEKO and CST MICROWAVE STUDIO, respectively. There is a 10 dB radial spacing (i.e., 10 dB per division) for all patterns.

B.1 HMLWA vs. FMLWA simulated on an infinite ground plane

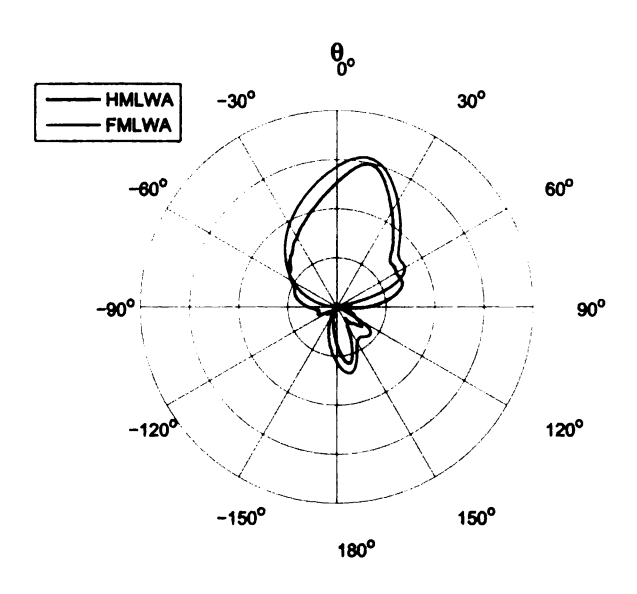


Figure B.1. Radiation Patterns of HMLWA antenna vs. FMLWA antenna at 6GHz mounted atop an infinite substrate-ground plane layer.

B.2 HMLWA vs. FMLWA simulated on a finite ground plane

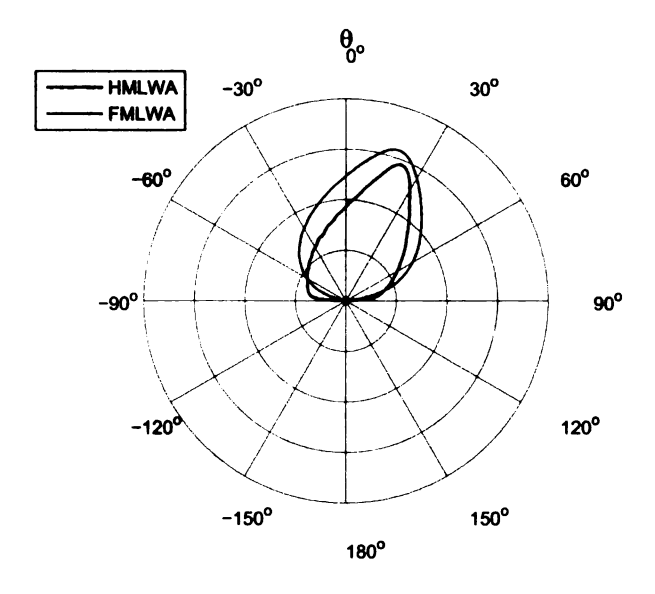


Figure B.2. Radiation Patterns of HMLWA antenna vs. FMLWA antenna at 6.25GHz mounted atop an infinite substrate-ground plane layer.

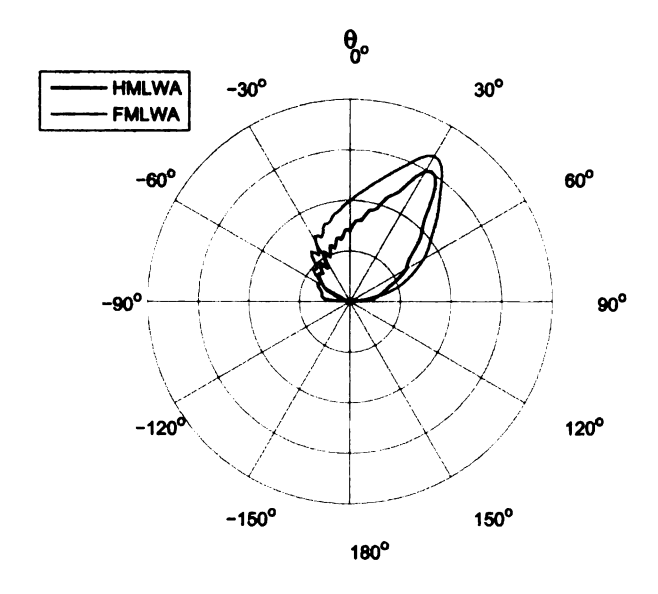


Figure B.3. Radiation Patterns of HMLWA antenna vs. FMLWA antenna at 6.5GHz mounted atop an infinite substrate-ground plane layer.

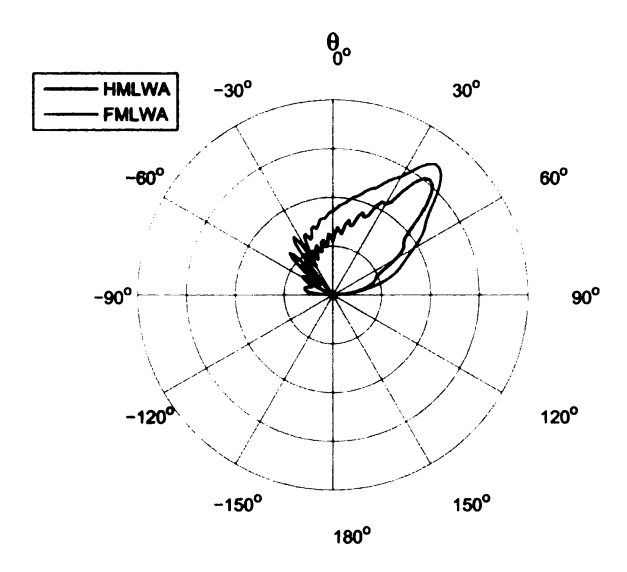


Figure B.4. Radiation Patterns of HMLWA antenna vs. FMLWA antenna at 6.75GHz mounted atop an infinite substrate-ground plane layer.

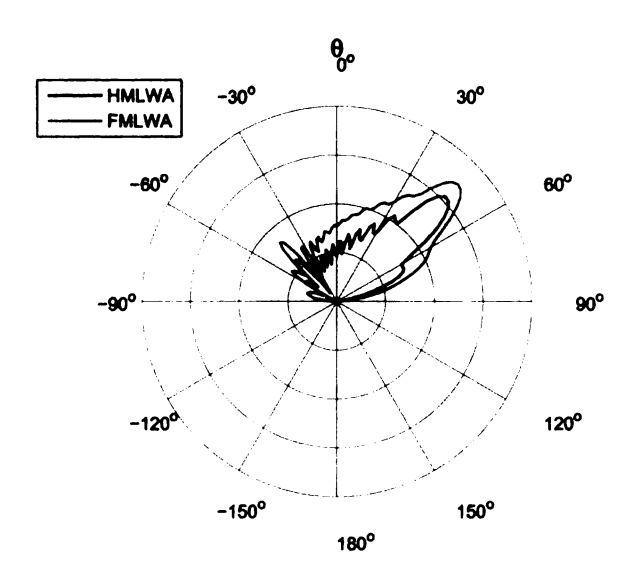


Figure B.5. Radiation Patterns of HMLWA antenna vs. FMLWA antenna at 7 GHz mounted atop an infinite substrate-ground plane layer.

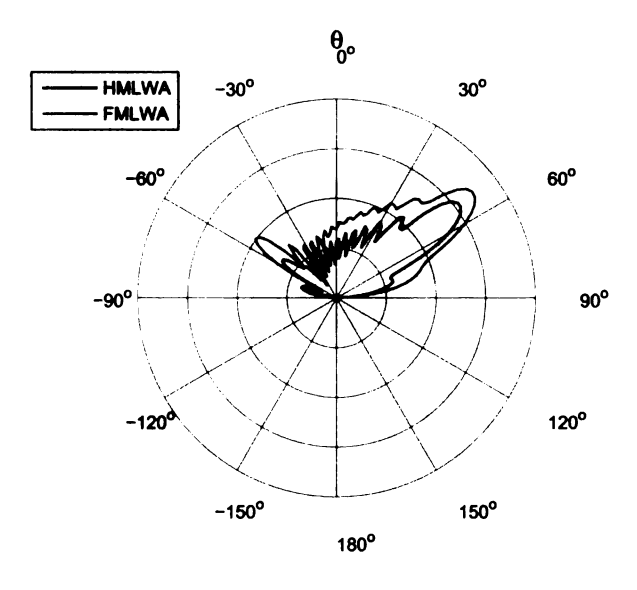


Figure B.6. Radiation Patterns of HMLWA antenna vs. FMLWA antenna at 7.25GHz mounted atop an infinite substrate-ground plane layer.

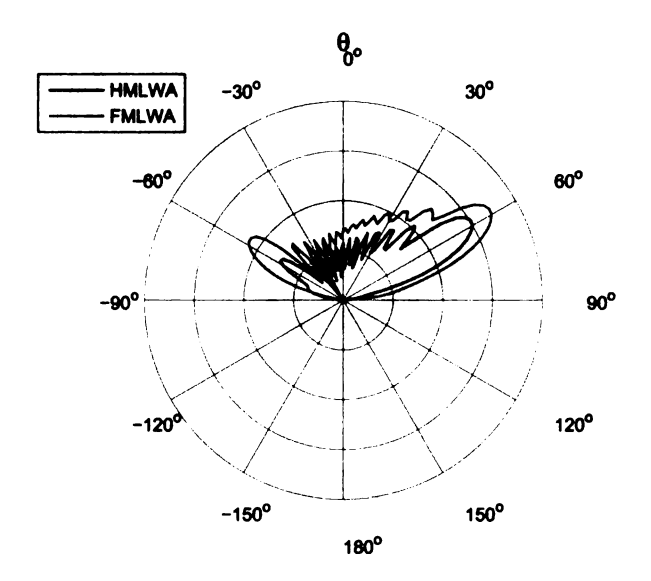


Figure B.7. Radiation Patterns of HMLWA antenna vs. FMLWA antenna at 7.5GHz mounted atop an infinite substrate-ground plane layer.

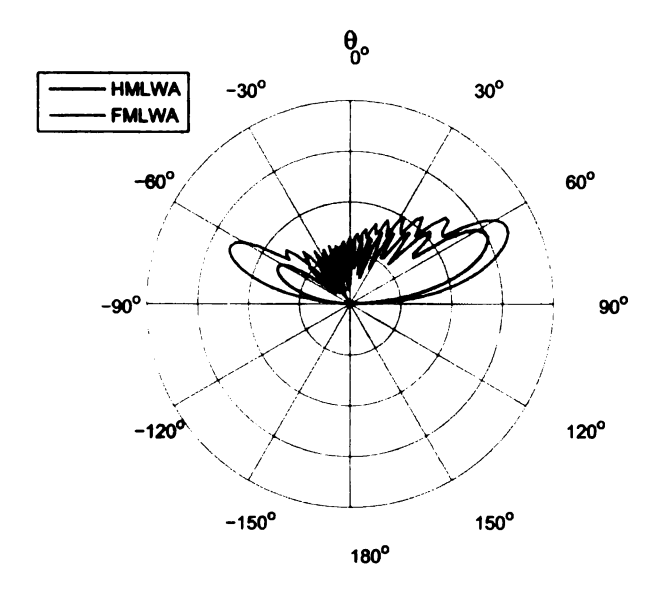


Figure B.8. Radiation Patterns of HMLWA antenna vs. FMLWA antenna at 7.75GHz mounted atop an infinite substrate-ground plane layer.

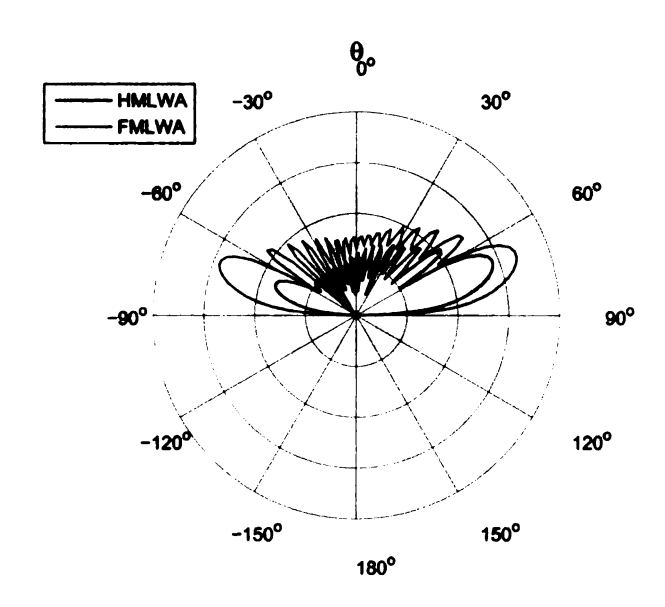


Figure B.9. Radiation Patterns of HMLWA antenna vs. FMLWA antenna at 8GHz mounted atop an infinite substrate-ground plane layer.

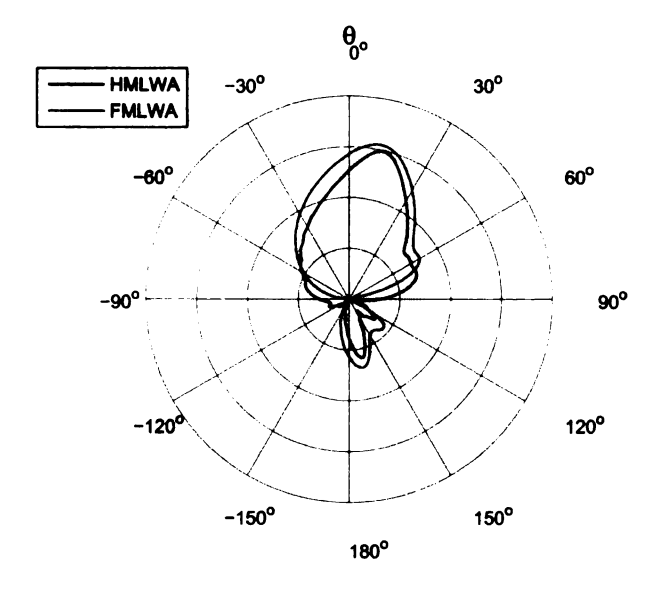


Figure B.10. Radiation Patterns of HMLWA antenna vs. FMLWA antenna at 6GHz mounted atop a finite substrate-ground plane layer.

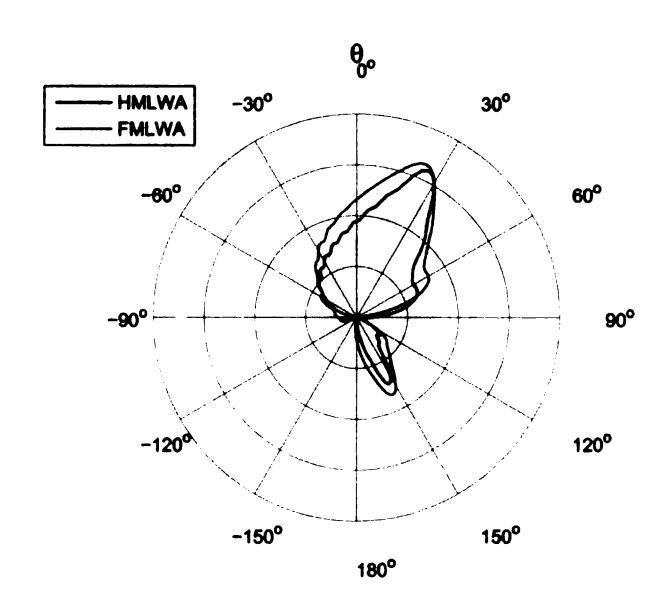


Figure B.11. Radiation Patterns of HMLWA antenna vs. FMLWA antenna at 6.25GHz mounted atop a finite substrate-ground plane layer.

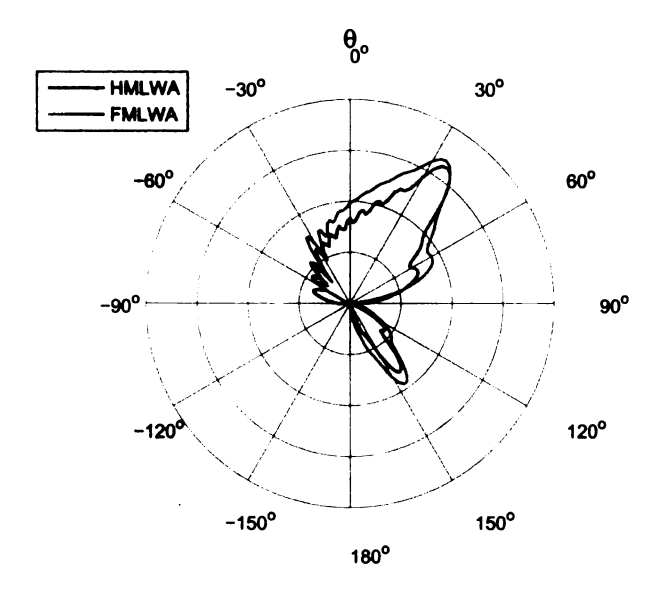


Figure B.12. Radiation Patterns of HMLWA antenna vs. FMLWA antenna at 6.5GHz mounted atop a finite substrate-ground plane layer.

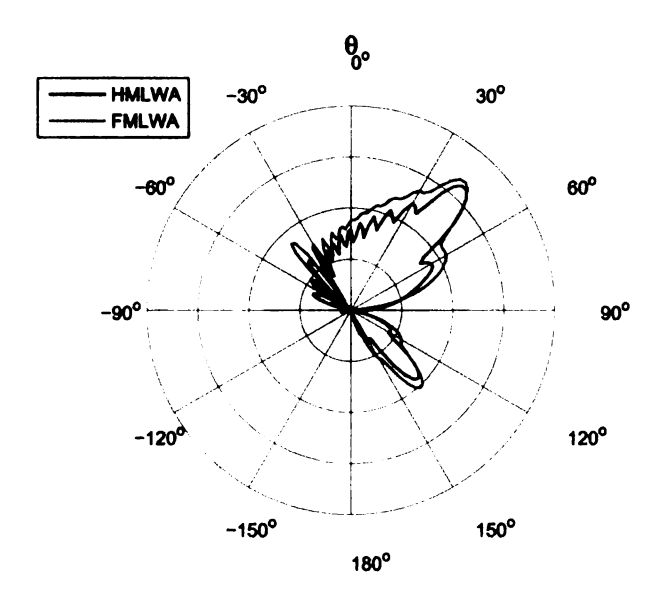


Figure B.13. Radiation Patterns of HMLWA antenna vs. FMLWA antenna at 6.75GHz mounted atop a finite substrate-ground plane layer.

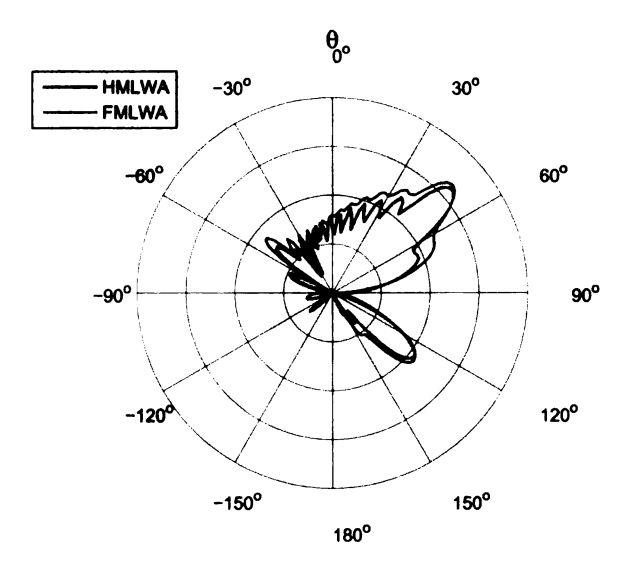


Figure B.14. Radiation Patterns of HMLWA antenna vs. FMLWA antenna at 7GHz mounted atop a finite substrate-ground plane layer.

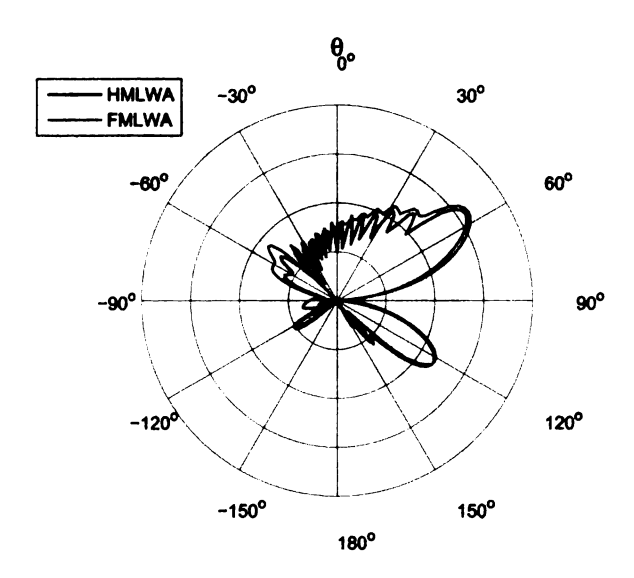


Figure B.15. Radiation Patterns of HMLWA antenna vs. FMLWA antenna at 7.25GHz mounted atop a finite substrate-ground plane layer.

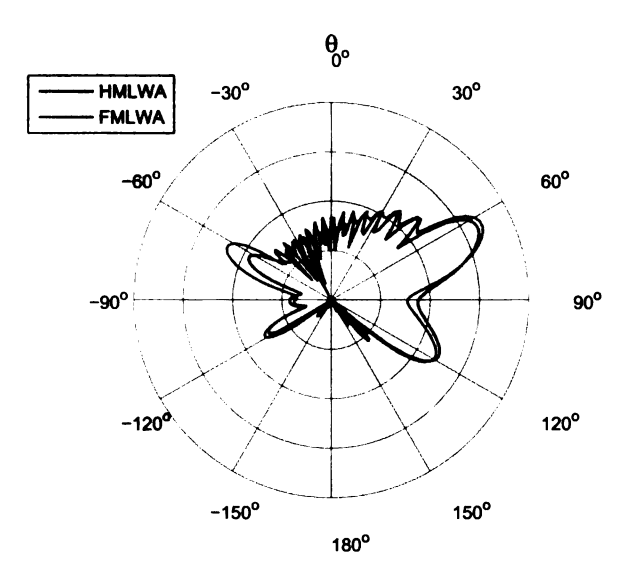


Figure B.16. Radiation Patterns of HMLWA antenna vs. FMLWA antenna at 7.5GHz mounted atop a finite substrate-ground plane layer.

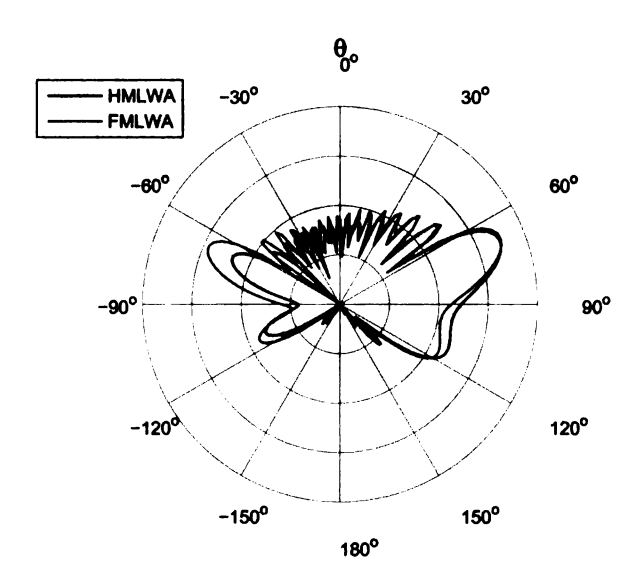


Figure B.17. Radiation Patterns of HMLWA antenna vs. FMLWA antenna at 7.75GHz mounted atop a finite substrate-ground plane layer.

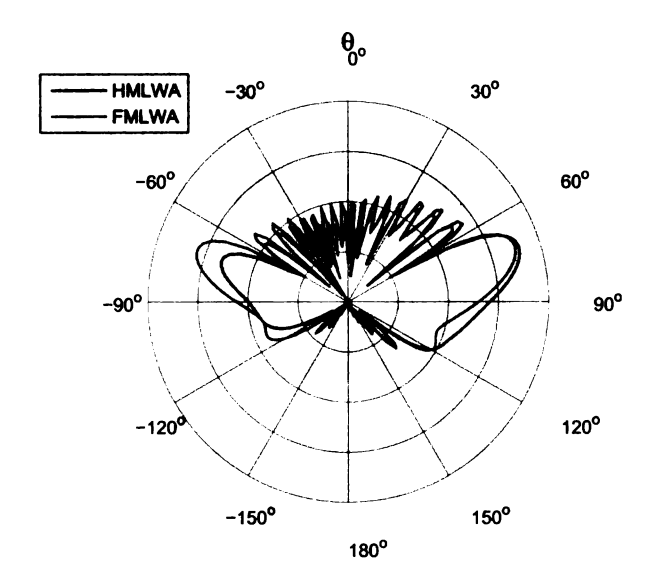


Figure B.18. Radiation Patterns of HMLWA antenna vs. FMLWA antenna at 8GHz mounted atop a finite substrate-ground plane layer.

APPENDIX C

UNLOADED HMLWA ANTENNA CHARACTERISTICS

In this appendix, characteristics of the unloaded HMLWA antenna including the freeedge impedance, transverse and axial wave numbers and other characteristics are presented.

Figure C.1 and Figure C.2 depict the resistance and reactance at the free-edge of the antenna. It implements the free-edge impedance described by equation (3.69) of Section 3.5. Figure C.3 through Figure C.6 show the real, imaginary, magnitude, and phase of χ , the phase of the free-edge impedance (equation (3.78) of Section 3.5). Finally, Figure C.7 through Figure C.10 show the real and imaginary parts of the transverse and axial wavenumbers, k_T and k_z , respectively.

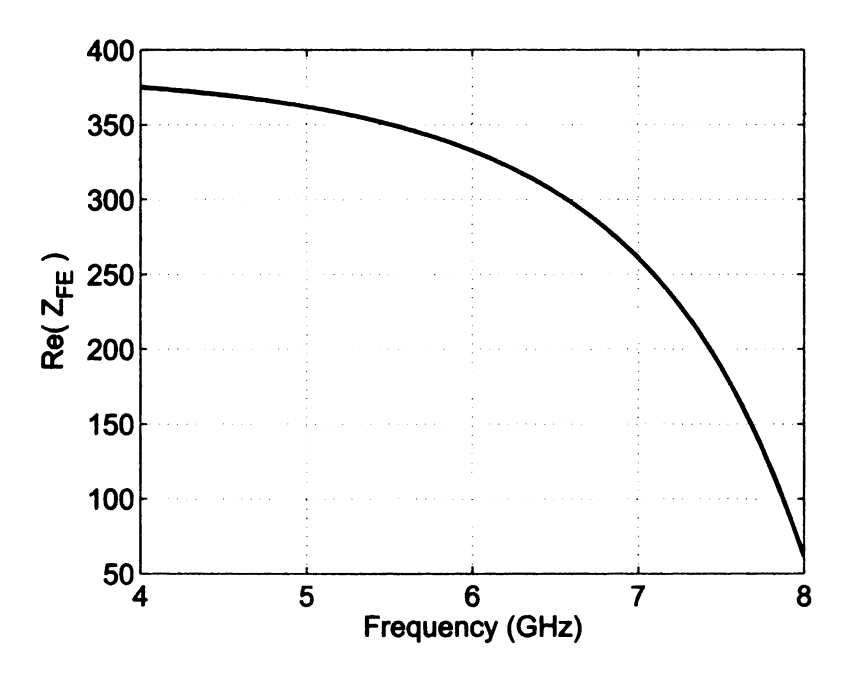


Figure C.1. Free-edge resistance of the unloaded HMLWA antenna.

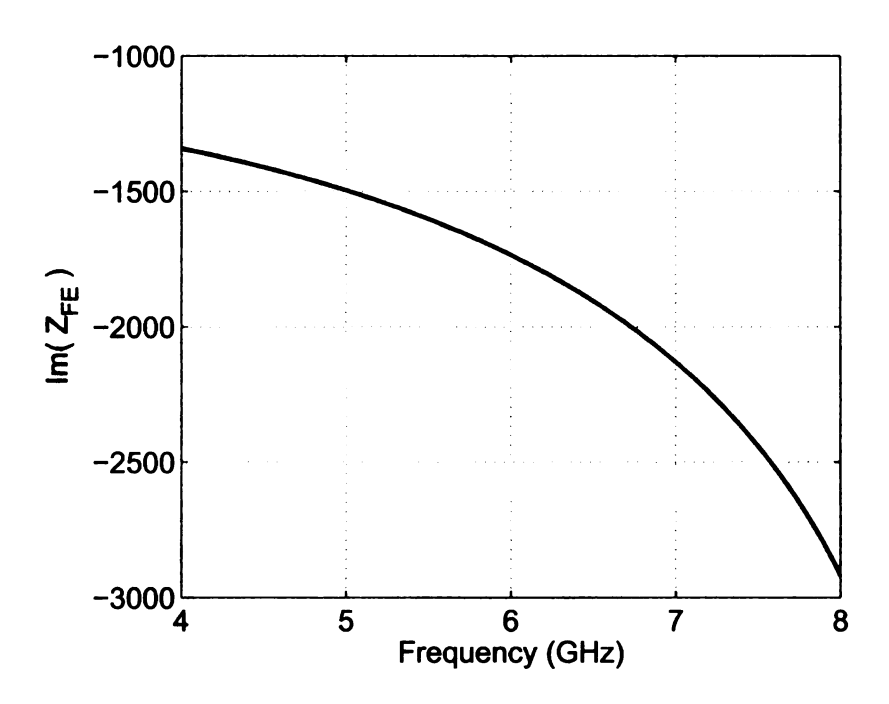


Figure C.2. Free-edge reactance of the unloaded HMLWA antenna.

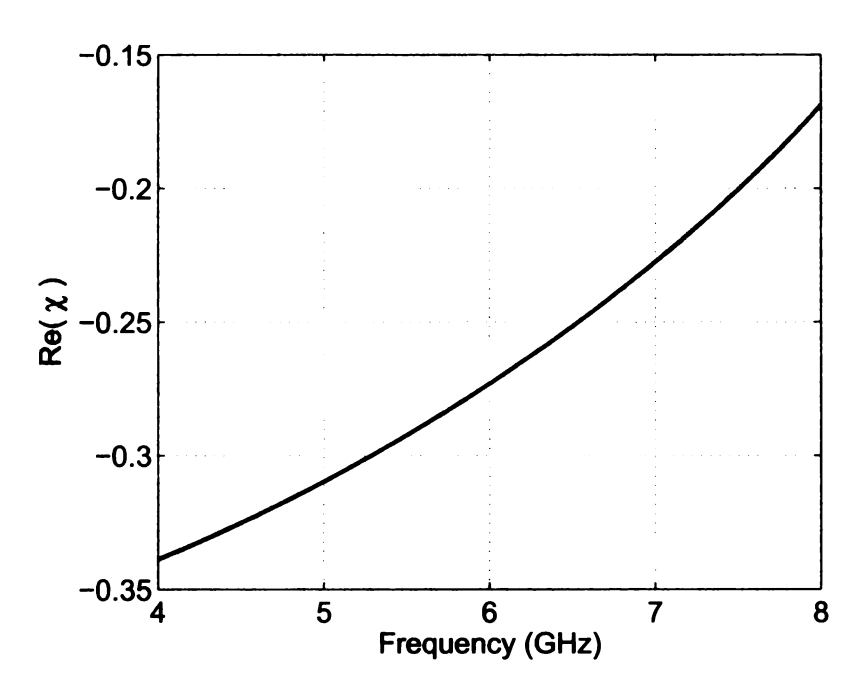


Figure C.3. $Re(\chi)$ of the unloaded HMLWA antenna.

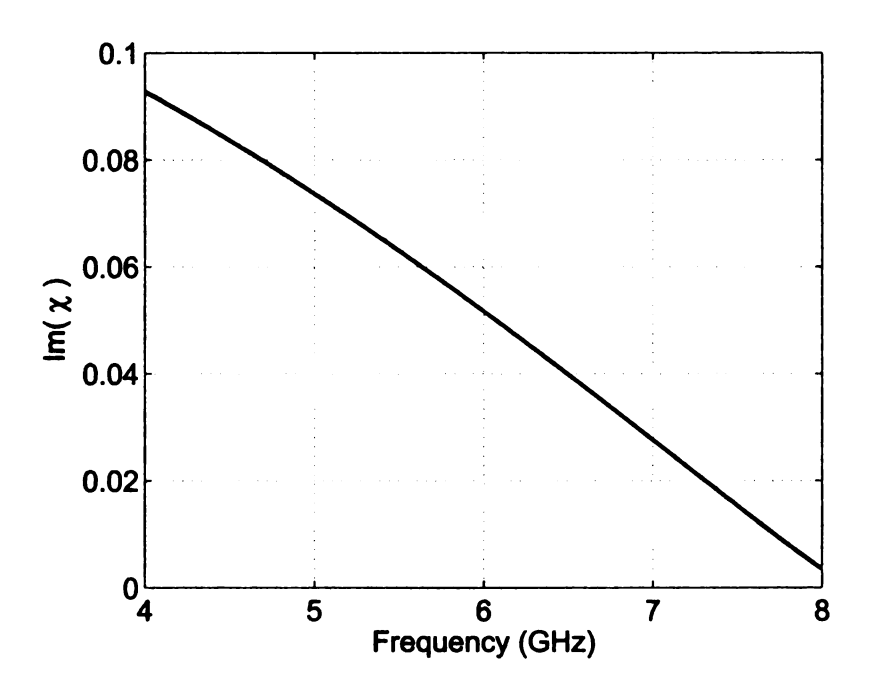


Figure C.4. $Im(\chi)$ of the unloaded HMLWA antenna.

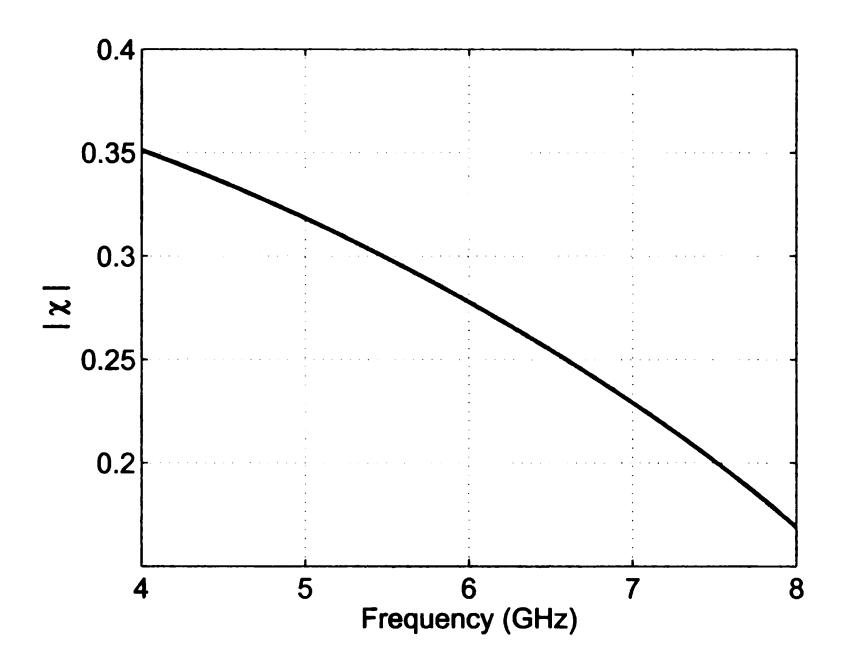


Figure C.5. $|\chi|$ of the unloaded HMLWA antenna.

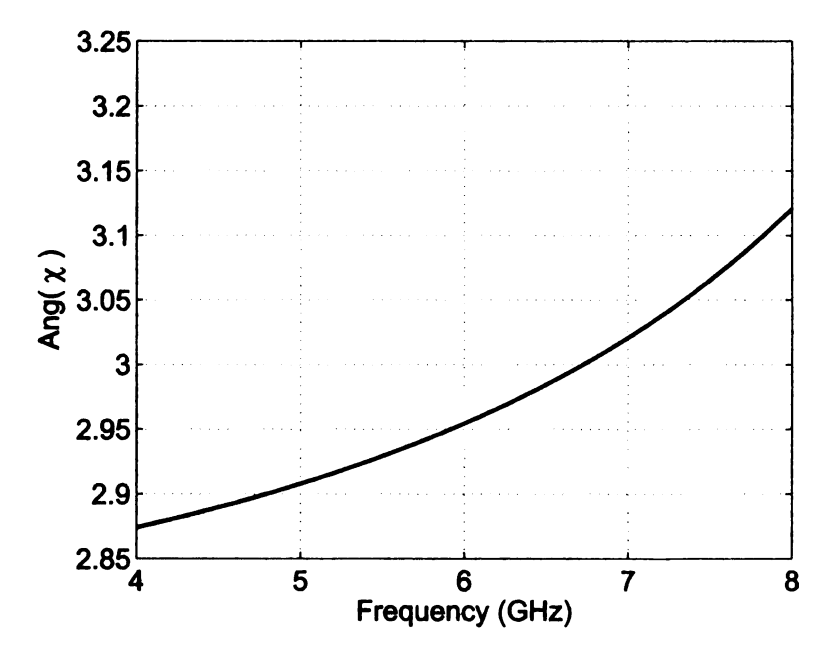


Figure C.6. $Ang(\chi)$ of the unloaded HMLWA antenna.

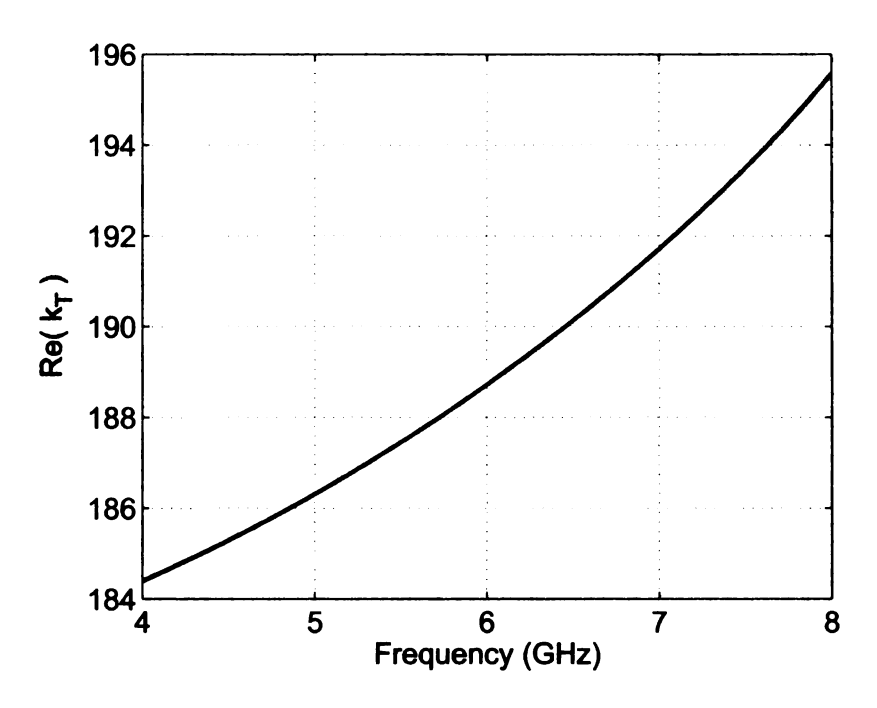


Figure C.7. $Re(k_T)$ of the unloaded HMLWA antenna.

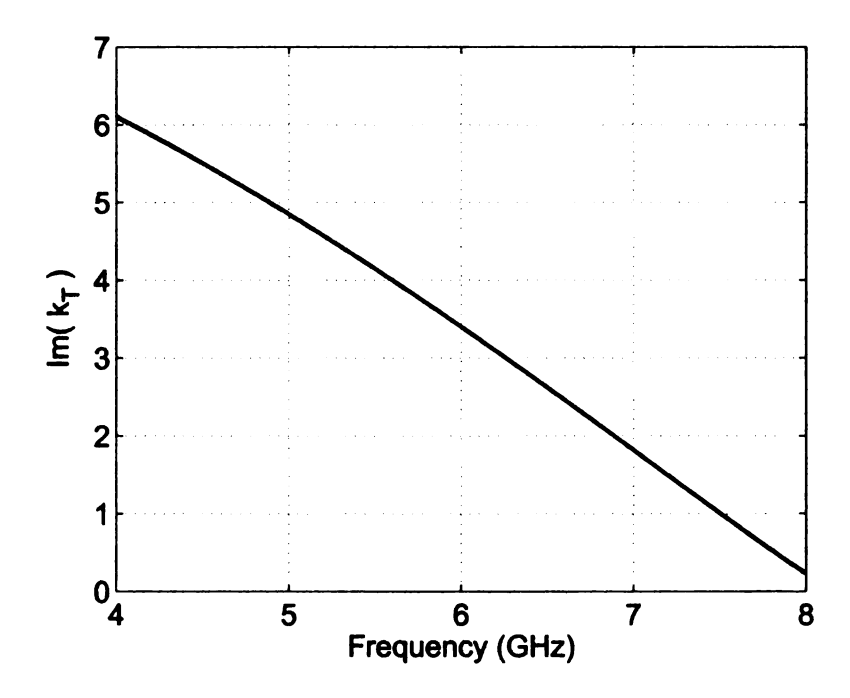


Figure C.8. $Im(k_T)$ of the unloaded HMLWA antenna.

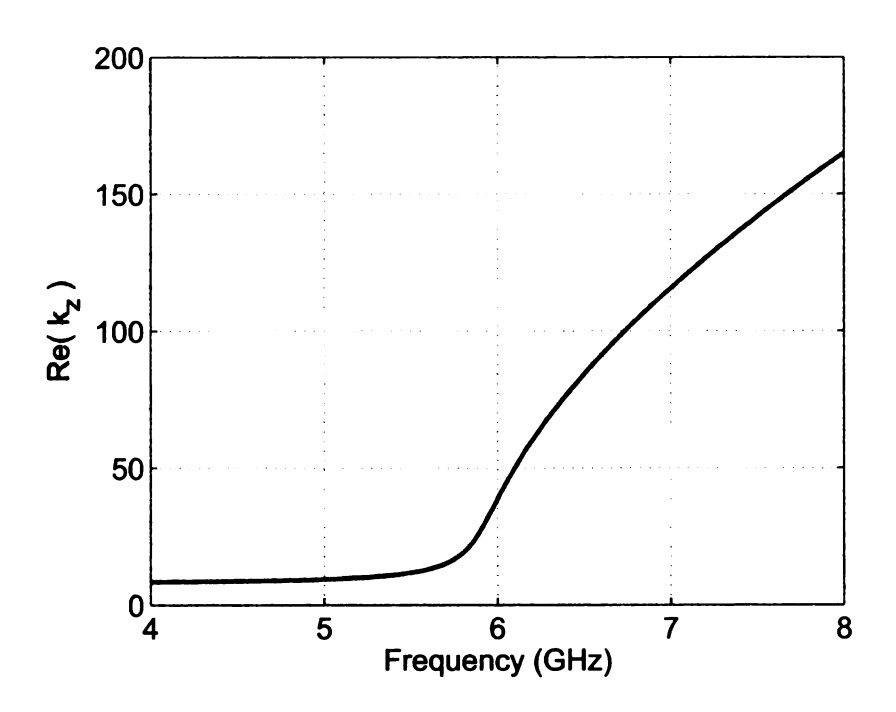


Figure C.9. $Re(k_z)$ of the unloaded HMLWA antenna.

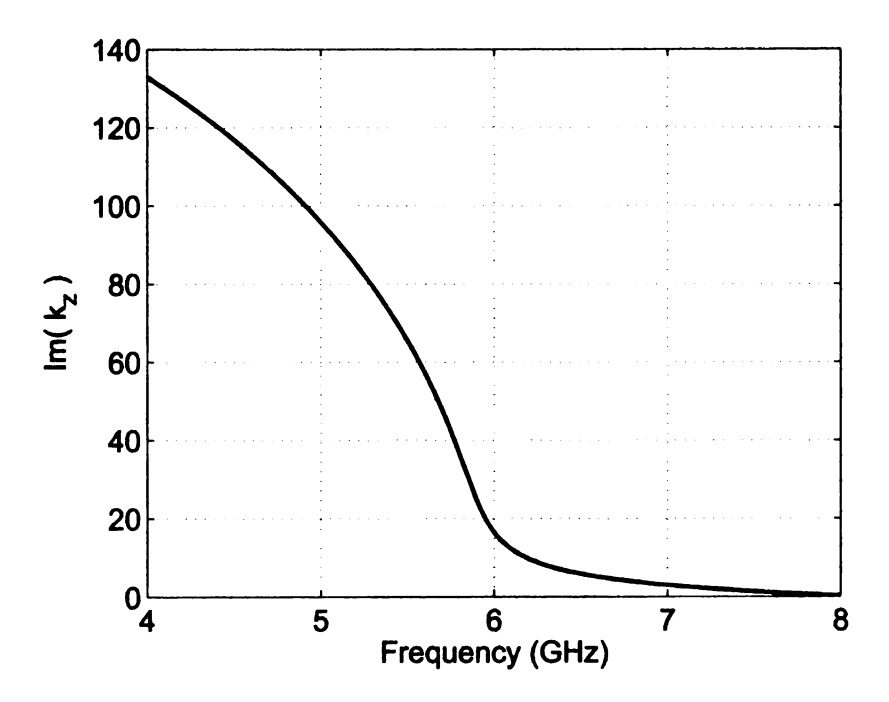


Figure C.10. $Im(k_z)$ of the unloaded HMLWA antenna.

APPENDIX D

0.10 PF PARALLEL-LOADED HMLWA ANTENNA CHARACTERISTICS

In this appendix, characteristics of the 0.10 pF loaded HMLWA antenna including the free-edge impedance, transverse and axial wave numbers and other characteristics are presented.

Figure D.1 and Figure D.2 depict the resistance and reactance at the free-edge of the antenna. It implements the free-edge impedance described by equation (3.69) of Section 3.5. Figure D.3 and Figure D.4 show the resistance and reactance of the parallel-combination of the 0.10 pF lumped capacitor and the free-edge impedance at the radiating edge of the HMLWA antenna, respectively. Figure D.5 through Figure D.8 show the real, imaginary, magnitude, and phase of χ , the phase of the free-edge impedance (equation (3.78) of Section 3.5). Finally, Figure D.9 through Figure D.12 show the real and imaginary parts of the transverse and axial wavenumbers, k_T and k_z , respectively.

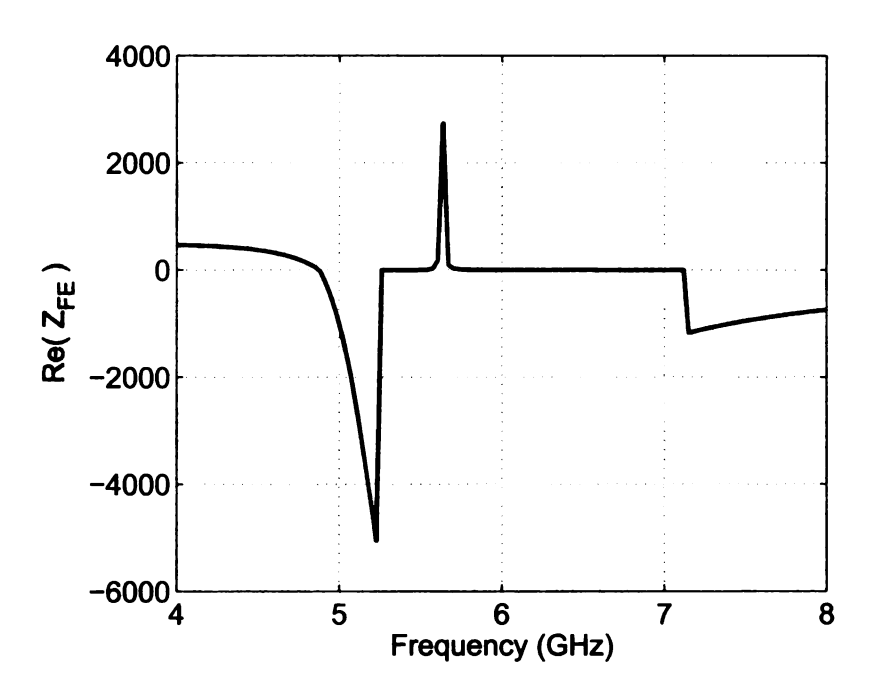


Figure D.1. Free-edge resistance of the 0.10 pF loaded HMLWA antenna.

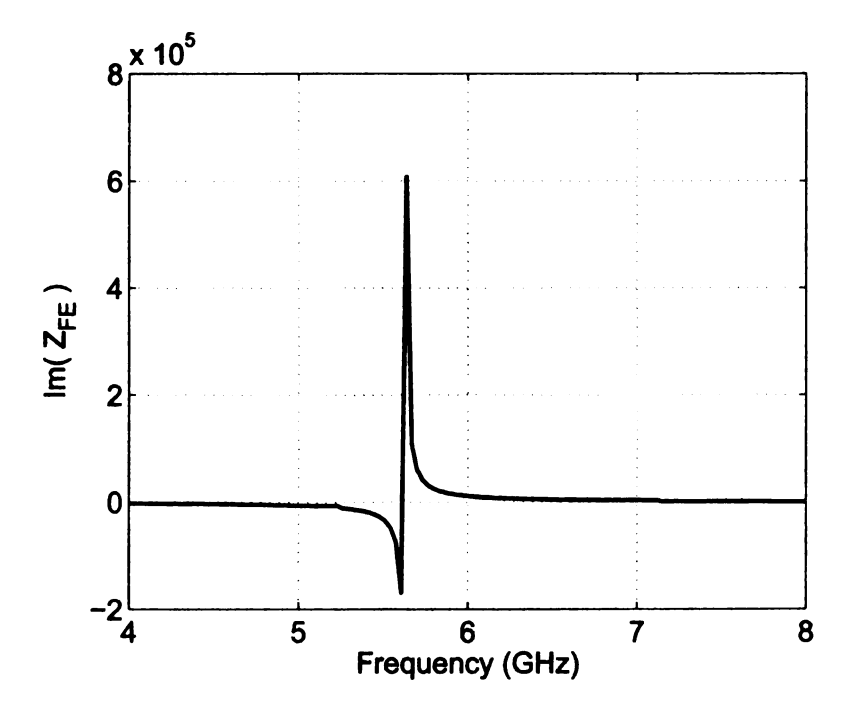


Figure D.2. Free-edge reactance of the 0.10 pF loaded HMLWA antenna.

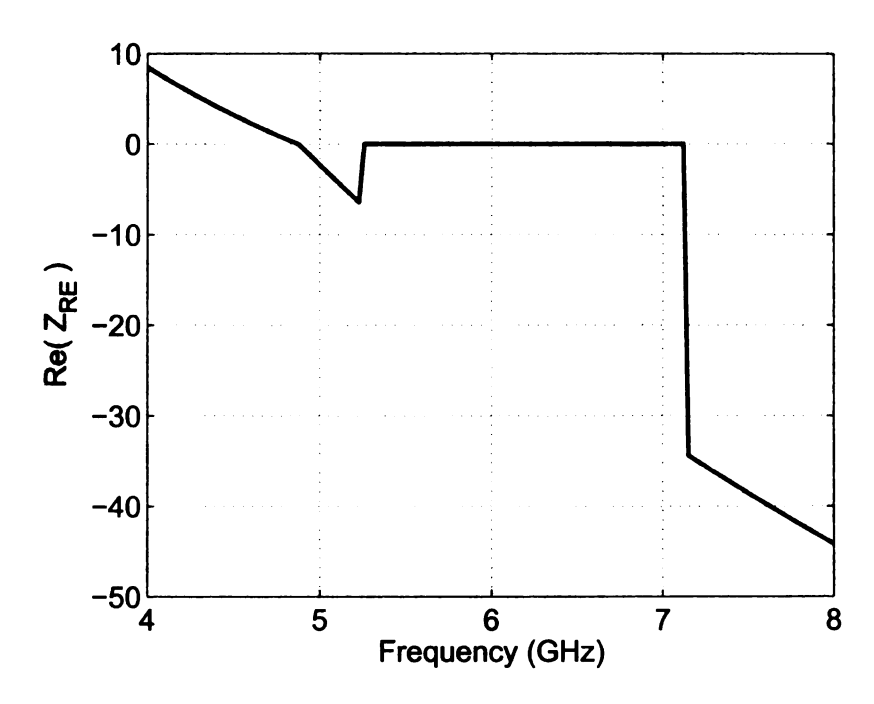


Figure D.3. Radiating-edge resistance of the 0.10 pF loaded HMLWA antenna.

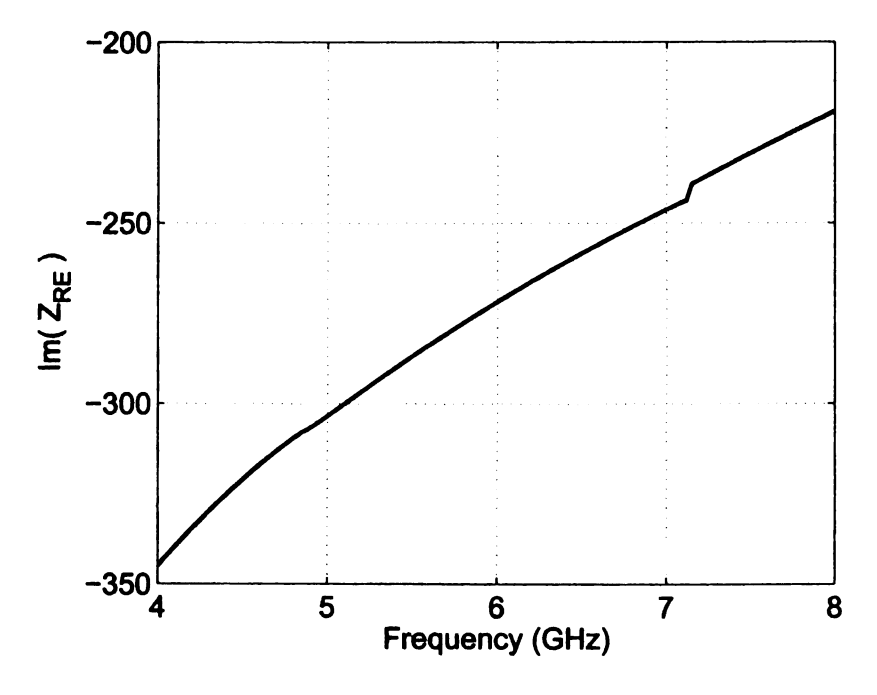


Figure D.4. Radiating-edge reactance of the 0.10 pF loaded HMLWA antenna.

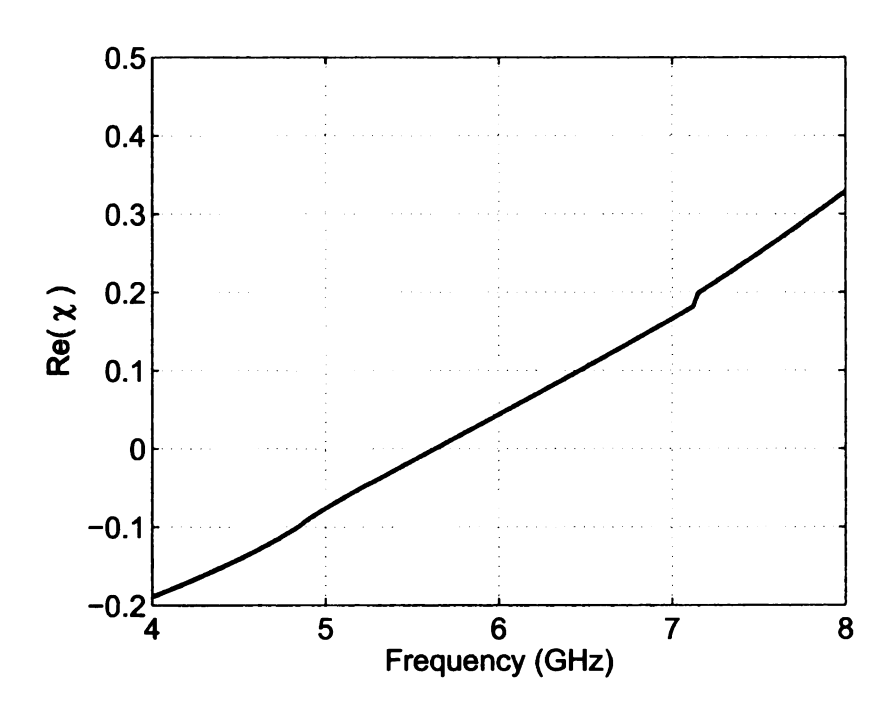


Figure D.5. $Re(\chi)$ of the 0.10 pF loaded HMLWA antenna.

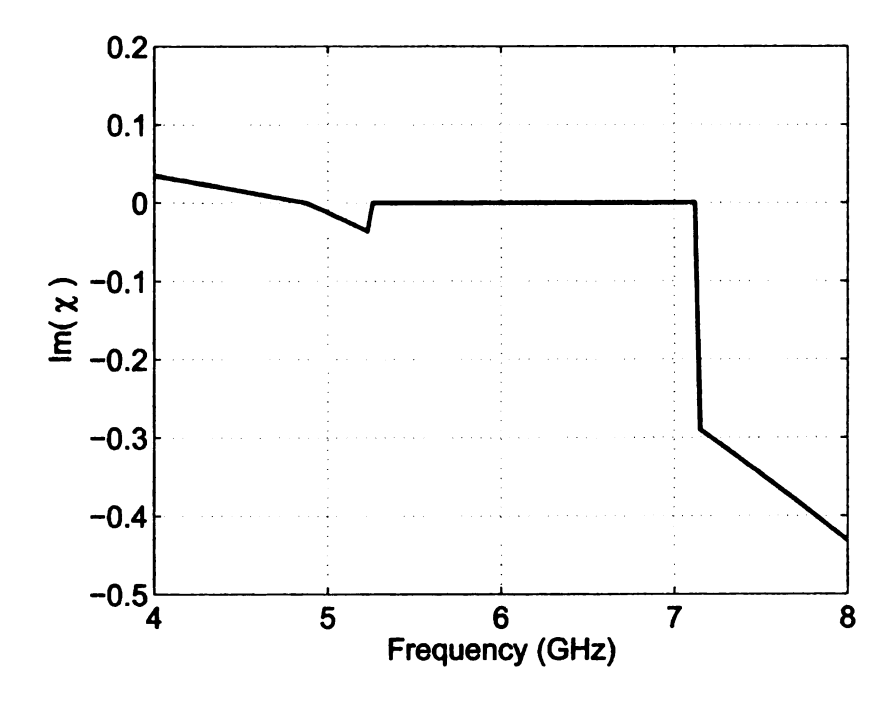


Figure D.6. $Im(\chi)$ of the 0.10pF loaded HMLWA antenna.

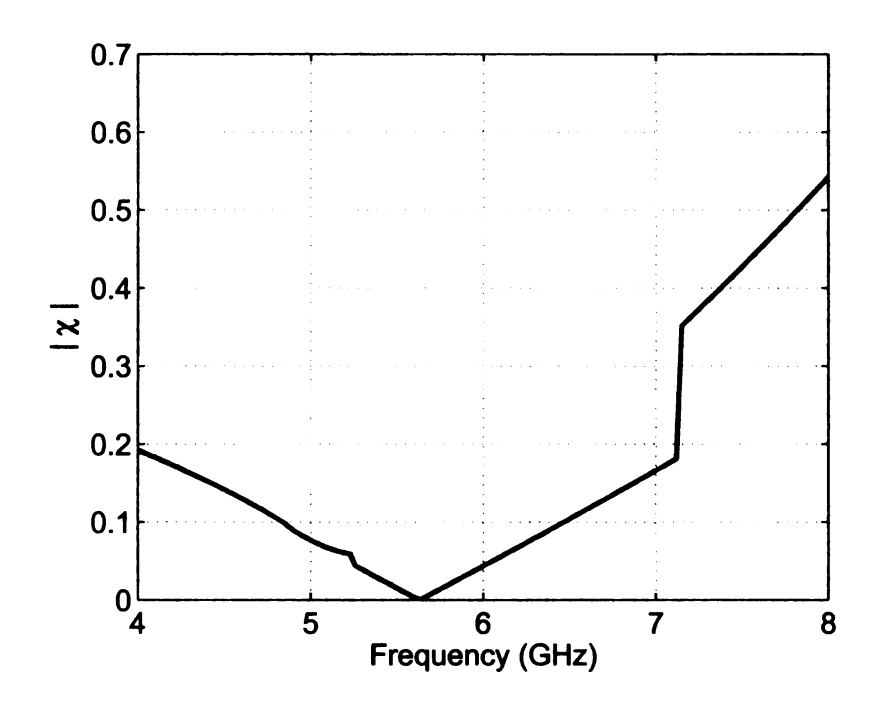


Figure D.7. $|\chi|$ of the 0.10 pF loaded HMLWA antenna.

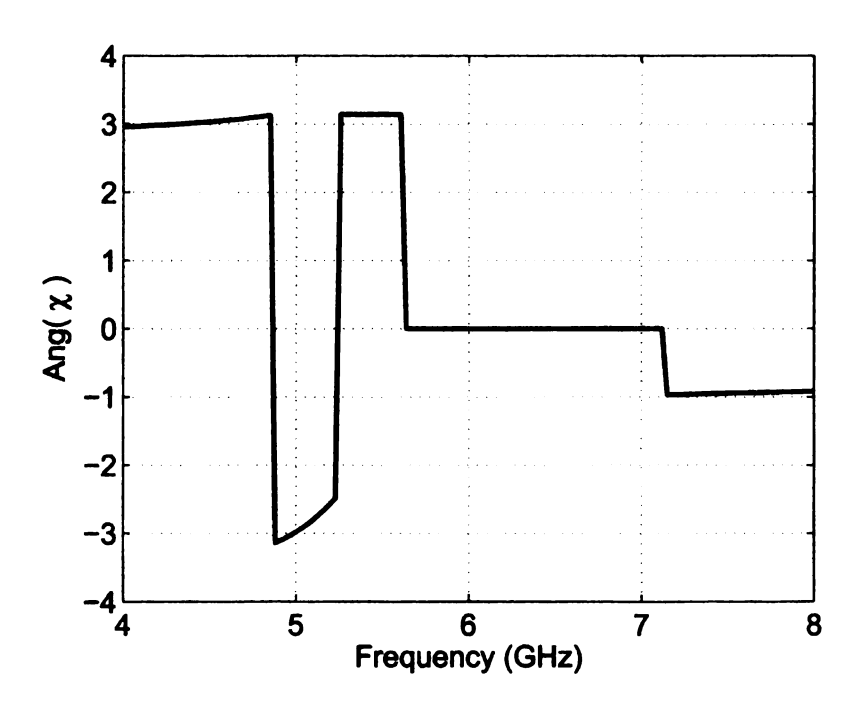


Figure D.8. $Ang(\chi)$ of the 0.10 pF loaded HMLWA antenna.

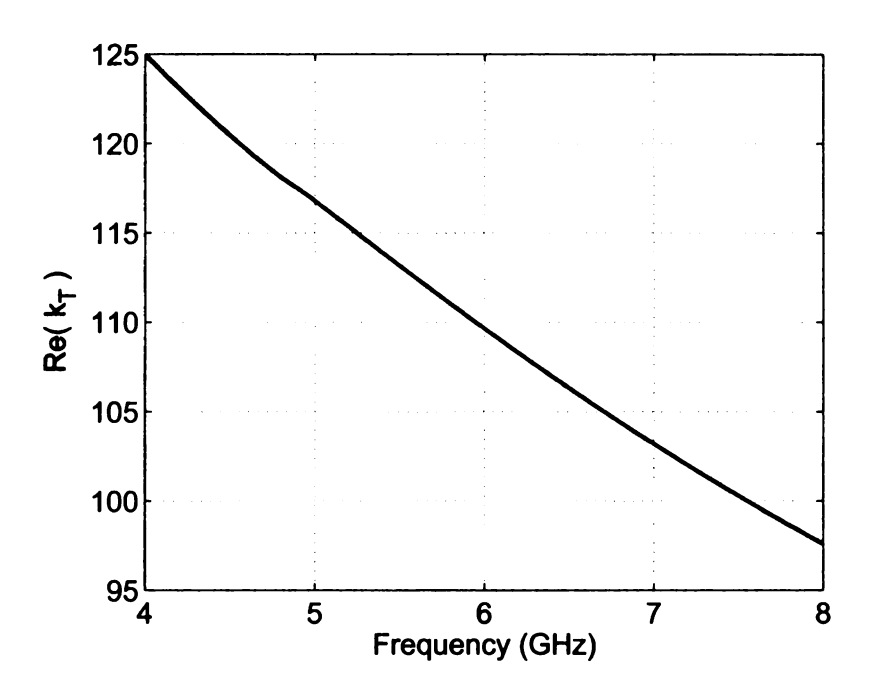


Figure D.9. $Re(k_T)$ of the 0.10 pF loaded HMLWA antenna.

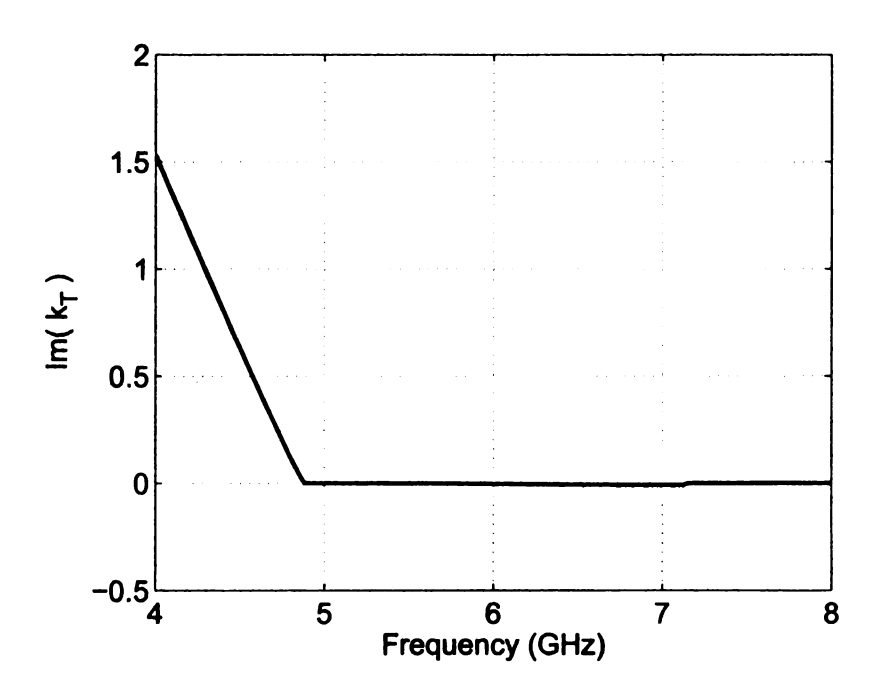


Figure D.10. $Im(k_T)$ of the 0.10 pF loaded HMLWA antenna.

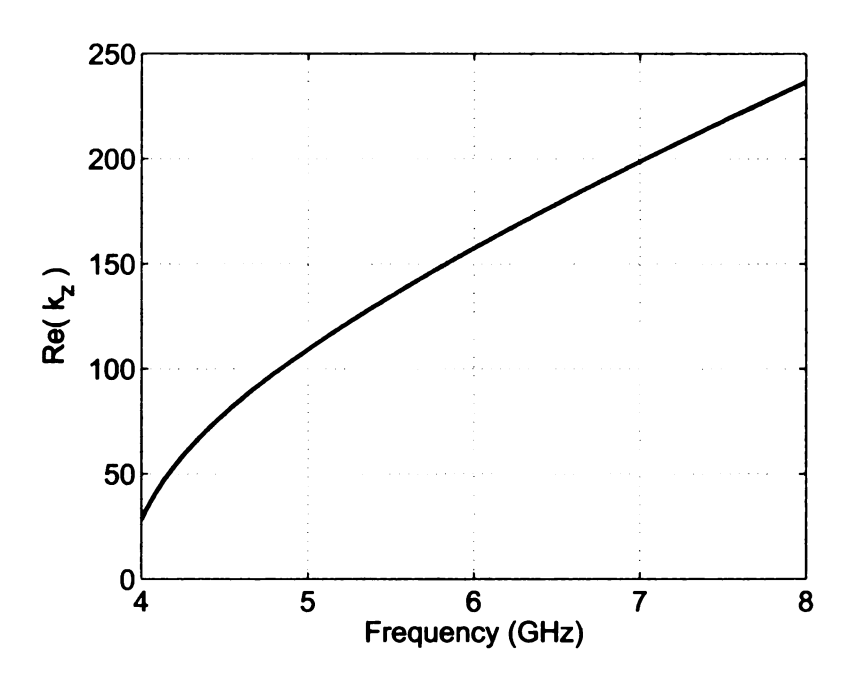


Figure D.11. $Re(k_z)$ of the 0.10 pF loaded HMLWA antenna.

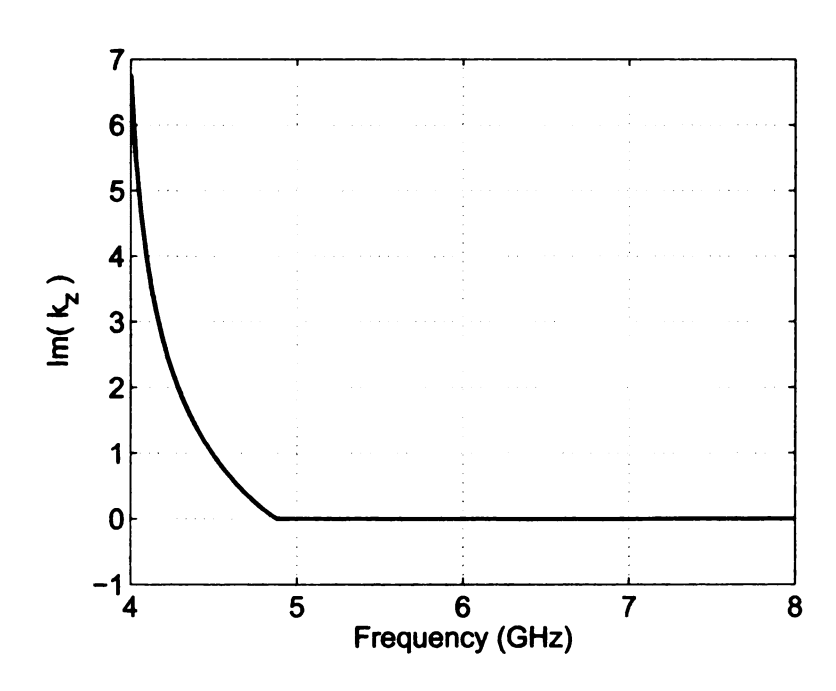


Figure D.12. $Im(k_z)$ of the 0.10 pF loaded HMLWA antenna.

APPENDIX E

MEASURED RADIATION PATTERNS OF THE CAPACITIVELY LOADED HMLWA ANTENNA

The patterns shown in Figure E.1 through Figure E.17 were measured in the NSI spherical near-field measurement system. The author would like to express his sincere gratitude to team RASCAL of AFRL for providing the resources required to obtain the patterns.

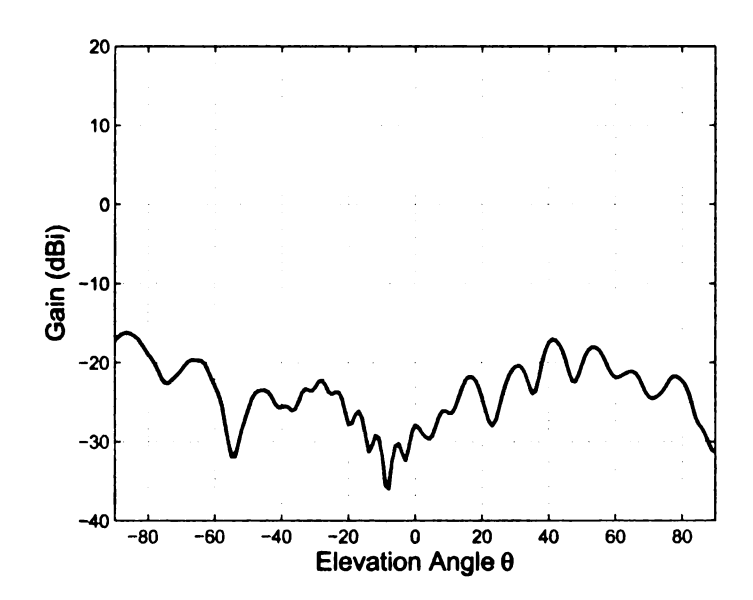


Figure E.1. Measured Radiation Pattern of HMLWA antenna at 4.00 GHz

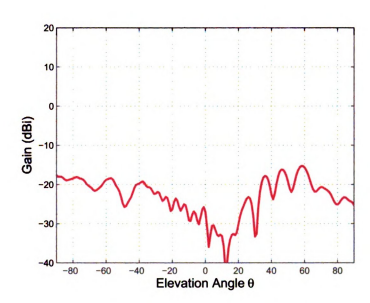


Figure E.2. Measured Radiation Pattern of HMLWA antenna at 4.25 GHz

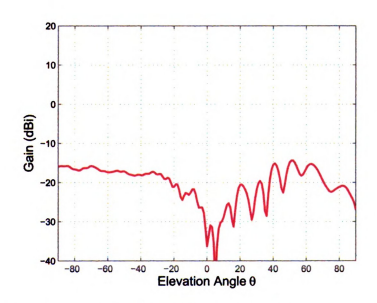


Figure E.3. Measured Radiation Pattern of HMLWA antenna at 4.50 GHz

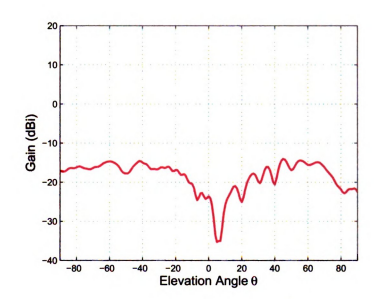


Figure E.4. Measured Radiation Pattern of HMLWA antenna at 4.75 GHz

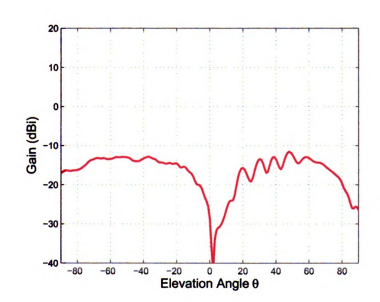


Figure E.5. Measured Radiation Pattern of HMLWA antenna at 5.00 GHz

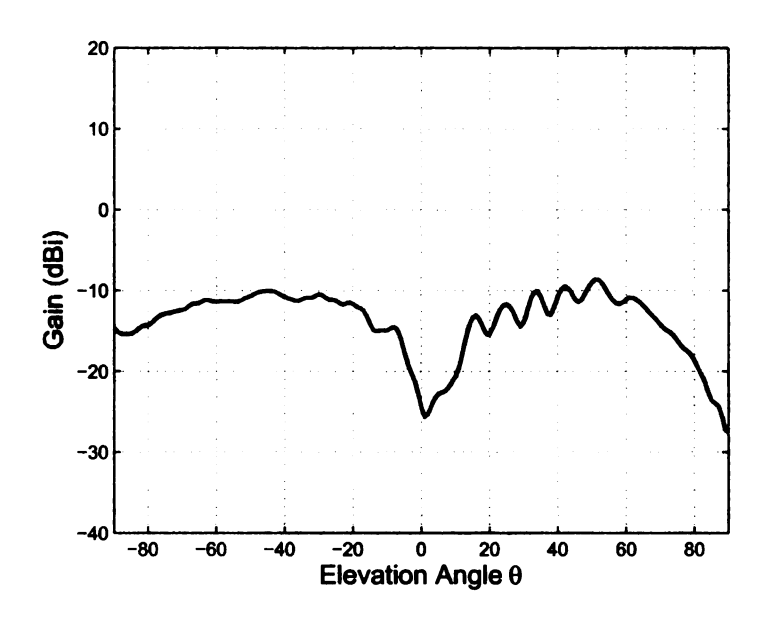


Figure E.6. Measured Radiation Pattern of HMLWA antenna at 5.25 GHz

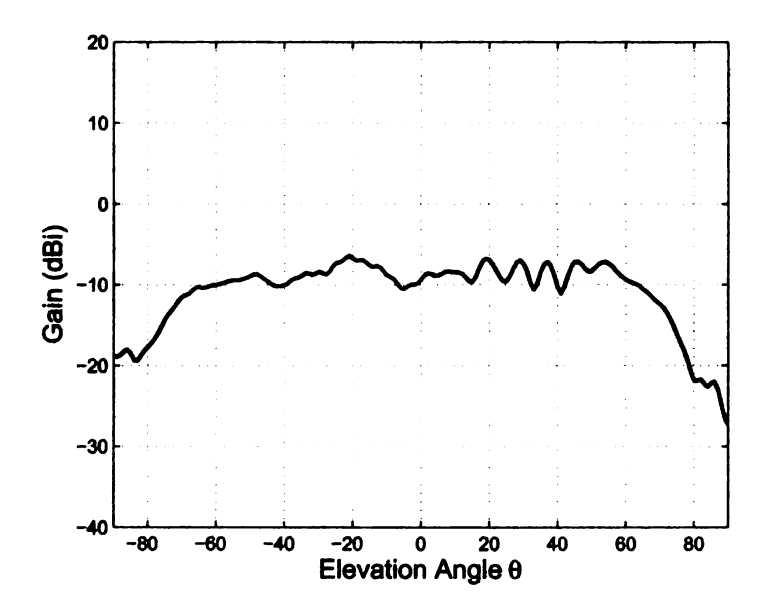


Figure E.7. Measured Radiation Pattern of HMLWA antenna at $5.50~\mathrm{GHz}$

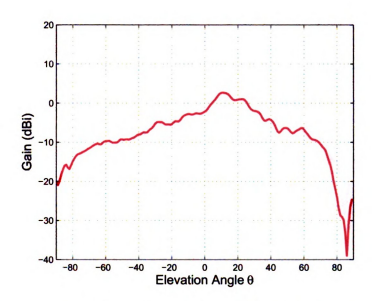


Figure E.8. Measured Radiation Pattern of HMLWA antenna at $5.75~\mathrm{GHz}$

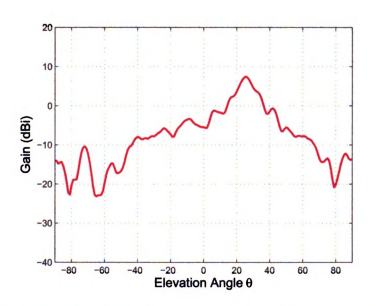


Figure E.9. Measured Radiation Pattern of HMLWA antenna at $6.00~\mathrm{GHz}$

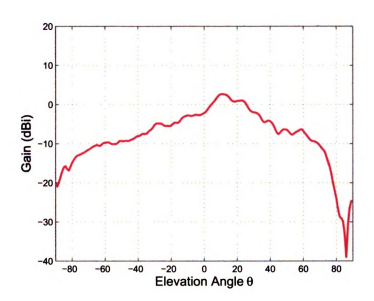


Figure E.8. Measured Radiation Pattern of HMLWA antenna at 5.75 GHz

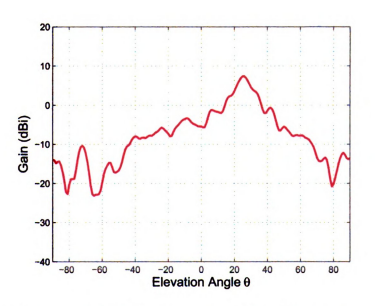


Figure E.9. Measured Radiation Pattern of HMLWA antenna at $6.00~\mathrm{GHz}$

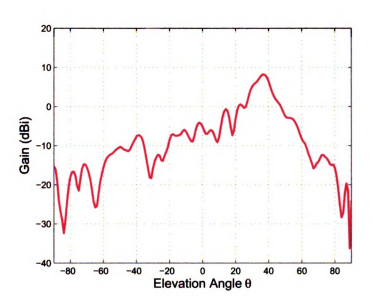


Figure E.10. Measured Radiation Pattern of HMLWA antenna at 6.25 GHz

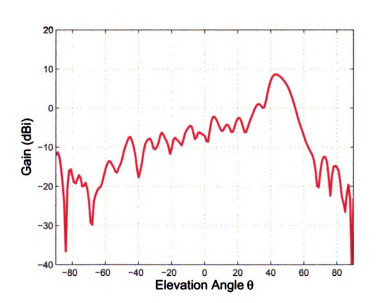


Figure E.11. Measured Radiation Pattern of HMLWA antenna at 6.50 GHz

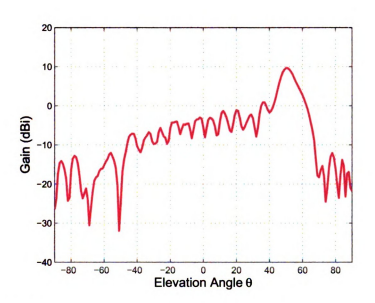


Figure E.12. Measured Radiation Pattern of HMLWA antenna at 6.75 GHz

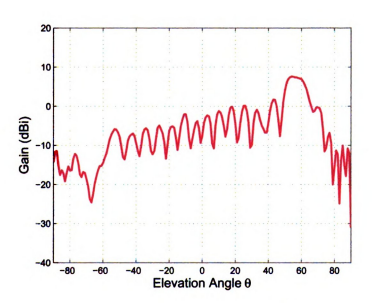


Figure E.13. Measured Radiation Pattern of HMLWA antenna at 7.00 GHz

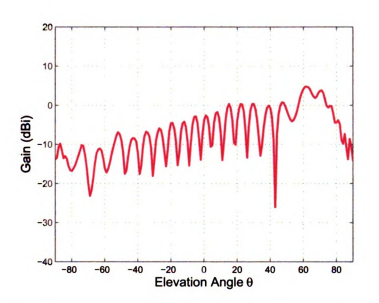


Figure E.14. Measured Radiation Pattern of HMLWA antenna at 7.25 GHz

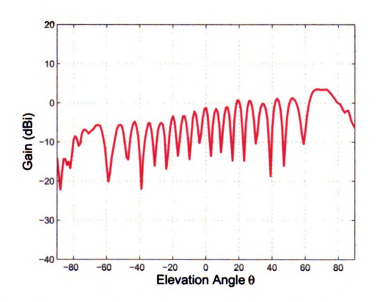


Figure E.15. Measured Radiation Pattern of HMLWA antenna at 7.50 GHz

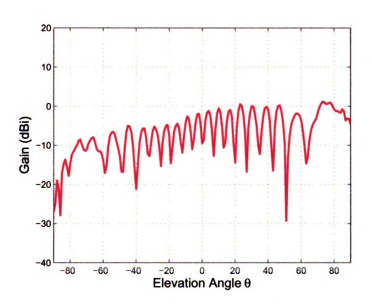


Figure E.16. Measured Radiation Pattern of HMLWA antenna at 7.75 GHz

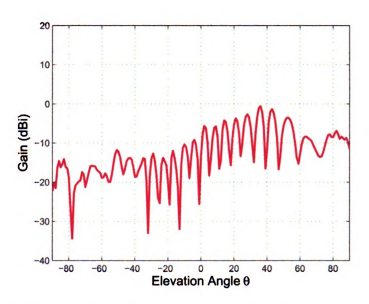


Figure E.17. Measured Radiation Pattern of HMLWA antenna at 8.00 GHz

BIBLIOGRAPHY

BIBLIOGRAPHY

- [1] J.L. Volakis, Antenna Engineering Handbook, McGraw-Hill, New York, 2007.
- [2] K.M. Noujeim, "Wave Propagation Characteristics of a Reactively Loaded Microstrip," IEEE MTT-S Digest, vol. 2, pp. 821-824, June 2003.
- [3] G. Augustin, S.V. Shynu, P. Mohanan, C.K. Aanandan and K. Vasudevan, "Wide Band Electronically Scannable Leaky Wave Antenna for Low Cost Beam Steering Applications," Microw. Conf. Proc., 2005. APMC 2005. Asia-Pacific Conference Proceedings, vol. 4, Dec. 2005.
- [4] G. Augustin, S.V. Shynu, P. Mohanan, C.K. Aanandan and K. Vasudevan, "Reactive loaded microstrip leaky wave antenna for low cost beam steering applications," Microw. and Optical Technology Let., vol. 48, no.11, pp. 2299-2301, Nov. 2006.
- [5] C. Luxey and J.-M. Laheurte, "Effect of reactive loading in microstrip leaky wave antennas," Electronics Letters, vol. 36, no.15, pp. 1259-1260, July 2000.
- [6] C. Wang, C.F. Jou, J. Wu and S. Peng, "Active Asymmetrically Feeding Dual-Beam Leaky-Wave Antenna," Microwave and Millimeter Wave Technology Proceedings, pp. 293-296, 1998.
- [7] C. Wang, C.F. Jou, J. Wu and S. Peng, "An Active Microstrip Antenna for Satellite Communication," Vehicular Technology Conference Proceedings, vol. 2, pp. 1386-1389, 2000.
- [8] D.C. Chang and E.F. Kuester, "Total and partial reflection from the end of a parallel-plate waveguide with an extended dielectric slab," Radio Science, vol. 16, pp. 1-13, Feb. 1981.
- [9] H. Ermert, "Guided modes and radiation characteristics of covered microstrip lines," Archiv fuer Elektronik und Uebertragungstechnik, pp. 65-70, February 1976.

- [10] H. Ermert, "Guiding and radiation characteristics of planar waveguides," European Microwave Conference, pp. 59-62, September 1979.
- [11] W. Menzel, "A New Traveling Wave Antenna in Microstrip," European Microwave Conference, pp. 302-306, October 1978.
- [12] A.A. Oliner and K. S. Lee, "Microstrip Leaky Wave Strip Antennas," IEEE AP-S International Symposium Digest, pp. 443-446, 1986.
- [13] Y.T. Lo and S.W.Lee, Antenna Handbook: Theory, Applications, and Design, Springer, 1988.
- [14] G.A. Thiele and D.S. Janning, United States Patent 7,109,928, "Conformal microstrip leaky wave antenna," September 19, 2006.
- [15] G.M. Zelinski, "Finite difference time domain (FDTD) analysis of a leaky traveling wave microstrip antenna," M.S. Thesis, Air Force Institute of Technology, Wright-Patterson Air Force Base, OH, 2005.
- [16] A.A. Oliner and K.S. Lee, "The Nature of the Leakage from Higher Modes on Microstrip Line," IEEE MTT-S Digest, pp. 57-60, 1986.
- [17] A.A. Oliner, "Leakage from Higher Modes on Microstrip Line with Application to Antennas," Radio Science, vol. 22, no. 6, pp. 907-912, 1987.
- [18] J.S. Bagby, C. Lee, D.P. Nyquist and Y. Yuan, "Identification of Propagation Regimes on Integrated Microstrip Transmission Lines," IEEE Transactions on Microwave Theory and Techniques, vol. 41, no. 11, pp. 1887-1894, November, 1993.
- [19] L.O. McMillan, N.V. Shuley and P.W. Davis, "Leaky Fields on Microstrip," Journal of Electromagnetic Waves and Applications, vol. 12, no. 2, pp. 225-227, 1998.

- [20] F. Mesa, D.R. Jackson and M.J. Freire, "Evolution of Leaky Modes on Printed-Circuit Lines," IEEE TRANSACTIONS on Microwave Theory and Techniques, vol. 50, no. 1, pp. 94-103, January, 2002.
- [21] C.A. Jaramillo-Henao, L.C. Kempel and S. Schneider, "Simulation of Microstrip Leaky-Wave Antennas on Inhomogeneous Substrates Using Transverse Resonance and Finite Element Methods," Electromagnetics, vol. 28, pp. 27-41, January 2008.
- [22] C.A. Balanis, Advanced Engineering Electromagnetics, John Wiley & Sons, New York, 1989.
- [23] F.T. Ulaby, Fundamentals of Applied Electromagnetics, Pearson Prentice Hall, New Jersey, 2004.
- [24] J.R. James and P.S. Hall, *Handbook of Microstrip Antennas*, Peter Peregrinus Ltd., London, United Kingdom, 1989, Chapter 3 (K.F.Lee and J.S.Dahele).
- [25] R. Garg, P. Bhartia, I. Bahl and A. Ittipiboon, *Microstrip Antenna Design Hand-book*, Artech House, Boston, Massachusetts, 1997.
- [26] R.S. Elliott, Antenna Theory and Design, John Wiley & Sons, New Jersey, 2003.
- [27] D.M. Pozar, Microwave Engineering, John Wiley & Sons, New York, 2005.
- [28] C.A. Balanis, Antenna Theory Analysis and Design, John Wiley & Sons, New York, 1997.
- [29] R.F. Harrington, Time-Harmonic Electromagnetic Fields, John Wiley & Sons, New York, 2001.
- [30] F. Gross, Smart Antennas for Wireless Communications With MATLAB, McGraw-Hill, New York, 2005.
- [31] E.J. Rothwell and M.J. Cloud, Electromagnetics, CRC Press, Boca Raton, 2001.

- [32] I.J. Bahl, P. Bhartia, *Microstrip Antennas*, Artech House, Dedham, Massachusetts, 1980.
- [33] K.S. Lee, "Microstrip leaky wave antenna," Ph.D. Dissertation, Polytechnic University, Brooklyn, NY, 1986.

